Characterization of $Li_4Ti_5O_{12}$ and $LiMn_2O_4$ spinel materials treated with aqueous acidic solutions

Cover: Design by Loïc Simonin and Daniel Simon

Printed by Wöhrmann Print Service

ISBN: 978-90-8570-173-6

Printed in The Netherlands

Characterization of $Li_4Ti_5O_{12}$ and $LiMn_2O_4$ spinel materials treated with aqueous acidic solutions

Proefschrift

ter verkrijging van de graad van doctor
aan de Technische Universiteit Delft,
op gezag van de Rector Magnificus prof.dr.ir. J.T. Fokkema,
voorzitter van het College voor Promoties,
in het openbaar te verdedigen

op dinsdag 24 april 2007 om 12:30 uur

door

Daniel Russell SIMON

Materials Engineer, University of Cincinnati

geboren te Ashtabula, Verenigde Staten

Dit proefschrift is goedgekeurd door de promotor
Prof.dr. J. Schoonman

Samenstelling promotiecommissie:

Rector Magnificus	Voorzitter
Prof.dr. J.Schoonman	Technische Universiteit Delft, promotor
Prof.dr. S.J. Picken	Technische Universiteit Delft
Prof.dr. J. Maier	Max Plank Institute, Duitsland
Prof.dr. J. Thomas	Uppsala Universitet, Zweden
Prof.dr. P.H.L. Notten	Technische Universiteit Eindhoven
Prof.dr.dr.h.c. M. Grätzel	EPFL Lausanne, Zwitserland
Dr. E.M. Kelder	Technische Universiteit Delft

Dr. E.M. Kelder heeft als begeleider in belangrijke mate aan de totstandkoming van het proefschrift bijgedragen.

Contents

1. Introduction **1**

1.1 General overview 2

1.2 Basic electrochemical cell 3

1.3 Thermodynamics of an electrochemical cell 4

1.4 Li-ion battery system 5

1.4.1 Materials used in the Li-ion battery system 7

1.4.1.1 Positive electrode materials overview 7

1.4.1.2 Negative electrode materials overview 9

1.4.1.3 Electrolyte overview 10

1.4.2 Electrode/electrolyte interface and electrode degradation 10

1.4.3 Battery design 12

1.5 Thesis overview 13

1.5.1 Spinel structure 14

1.5.2 Lithium titanium oxide spinel 15

1.5.2.1 Structural overview 15

1.5.2.2 Fabrication of $Li_4Ti_5O_{12}$ 15

1.5.2.3 Electrochemical characteristics 16

1.5.3 Lithium manganese oxide spinel 17

1.5.3.1 Jahn-Teller distortion of $LiMn_2O_4$ 17

1.5.3.2 The potential of $LiMn_2O_4$ 19

1.5.3.3 Measuring the potential of $LiMn_2O_4$ in aqueous solution 21

1.5.4 Experimental techniques and electrochemical testing 21

1.5.4.1 Electrode foil preparation 21

1.5.4.2 Coin cells 22

1.5.4.3 Electrochemical testing 23

1.6 Outline of thesis 23

1.7 References 26

2. **The formation of $Li_4Ti_5O_{12}$ using in-situ XRD during precursor decomposition** **33**
2.1 Introduction 34
2.2 Experimental 36
2.2.1 Precursors 36
2.2.2 Thermal Gravimetric Analysis and Differential Thermal Analysis 37
2.2.3 In-situ X-ray diffraction 37
2.3 Results 39
2.3.1 Thermal Gravimetric Analysis and Differential Thermal Analysis 39
2.3.2 In-situ X-ray diffractograms 41
2.3.3 Separation of peaks from diffractograms 46
2.4 Discussion 50
2.5 Conclusions 52
2.6 References 53

3. Proton exchange in $Li_4Ti_5O_{12}$ and its electrochemical properties **57**
3.1 Introduction 58
3.2 Experimental 59
3.2.1 Material preparation 59
3.2.2 Chemical titration of $Li_4Ti_5O_{12}$ 59
3.2.3 Structural characterization 59
3.2.4 Chemical, spectroscopy, and thermal analysis 60
3.2.5 Electrochemical characterization 60
3.3 Results and discussion 61
3.3.1 Chemical titration 61
3.3.1.1 Titration curves and XRD of the solids 61
3.3.1.2 Atomic Adsorption Spectroscopy (AAS) 63
3.3.1.3 FTIR transmission 64
3.3.1.4 Neutron diffraction 65
3.3.1.5 TGA and XRD 68
3.3.1.6 Reaction mechanism 70

3.3.2 Electrochemical characterization 71
3.3.2.1 Proton-exchanged material 71
3.3.2.2 Commercial $Li_4Ti_5O_{12}$ 73
3.4 Conclusions 76
3.5 References 77

4. Magnetic characterization of $Li_{(1-\delta)}Mn_{(2-\delta)}O_4$ and Li extacted spinels 81
4.1 Introduction 82
4.2 Experimental 83
4.2.1 Substitute spinels 83
4.2.2 Chemical extraction of $Li_{(1-\delta)}Mn_{(2-\delta)}O_4$ 83
4.2.3 Determination of the Mn oxidation state 84
4.2.4 X-ray diffraction 84
4.2.5 Magnetic measurements 84
4.3 Results and discussion 84
4.3.1 Structural and chemical characterizations 84
4.3.2 Magnetic characterization 90
4.3.3 Characterization of the near stoichiometric $LiMn_2O_4$ spinel 94
4.3.4 The Mn^{3+} electronic spin configuration 96
4.3.5 The relation between ion interactions and magnetic interactions 98
4.4 Conclusions 100
4.5 References 101

5. Open-circuit potential measurement of $LiMn_2O_4$ in aqueous solutions 105
5.1 Introduction 106
5.2 Theoretical aspects 108
5.2.1 The electric potential as a function of Li-ion extraction from $LiMn_2O_4$ using an electrochemical cell 108

5.2.2 The electric potential based on Hunter's equation 109
5.2.3 The relation between the open-circuit potential of $LiMn_2O_4$ in solution to the electric potential of the electrochemical cell 111
5.3 Experimental 112
5.3.1 Electrochemical characterization 112
5.3.2 Open-circuit potential of $LiMn_2O_4$ in an acidic solution 113
5.3.3 Monitoring the open-circuit potential and pH of a solution containing $LiMn_2O_4$ particles as a function of Li-ion extraction 113
5.4 Results and discussion 114
5.4.1 Open-circuit potential curve of the electrochemical cell 114
5.4.2 Chemical titration of $LiMn_2O_4$ 115
5.4.2.1 Open-circuit potential measurements of $LiMn_2O_4$ in aqueous solution 115
5.4.2.2 Open-circuit potential of Pt/Ag-AgCl electrode couple in solution with $LiMn_2O_4$ particles 118
5.4.2.3 Open-circuit potential as a function of pH 120
5.4.2.4 pH as a function of Li-ion extraction from $LiMn_2O_4$ 121
5.5 Conclusions 122
5.6 References 123

6. Summary and Outlook 125
Introduction 126
Summary 126
Outlook 129
Introductie 130
Samenvatting 130
Vooruitzicht 133
References/Referenties 134

Acknowledgements 137
About the author 139
Publications 141

1

Introduction

Abstract

A general description of the Li-ion battery system is given along with certain materials that are used as electrodes. In addition, the fabrication and stability of these electrode materials are also described. Finally, the scope of this thesis and the experimental details are discussed as well.

1.1 General overview

Energy storage has been and will continue to be one of the most important areas in technology as energy consumption continually increases. One of the reasons for this increase in energy consumption is the increased use of portable electronic devices. Although portable electronics has existed since the early 20th century, the use of portable electronic devices to the everyday consumer has increases dramatically since the 1980's (1). The demand for such products stems from the fact that these devices are rather compact that make it easy to carry. One of the biggest reasons for the compactness of these devices is directly due to the battery development that lead to a reasonable amount of dependable energy in such a compact volume.

There are two main categories in which battery systems are classified. The first category is the primary battery. These batteries are discharged only once and thus, used only once for an application. The second category is the secondary battery. These batteries are rechargeable and can be discharged and charged for multiple times or cycles (2).

For electronic portables, a common example of a primary battery is the alkaline cell. This battery is currently in production and retains a rather large consumer market. This system uses a Zn/MnO_2 electrode couple in an alkaline electrolyte. This battery has an operational potential of 1.5V and are manufactured usually in various cylindrical cans sizes. Some advantages of this system are the long shelf life (more than 4 years) and a reasonable operational life. The drawbacks for this system are low energy and power density (3).

One of the earliest secondary battery systems is the lead-acid system invented by Plante in 1859 (1). This system was easy to maintain because of its simple lead/lead oxide electrodes and water-based electrolyte. The operational potential was ~2V and is rechargeable. However, the theoretical energy density is only 165 Wh/kg and in practice only 25% of this energy density is realized. Most of the energy loss is mainly attributed to the weight of the electrodes themselves since Pb is used for both electrodes (2).

There are several advanced rechargeable battery systems that have been investigated. Some of the major systems include Ni/Cd, Ni/Metal Hydride, Li metal, and Li-ion sys-

tems. All of these systems are rechargeable and all of these systems possess a higher energy density than the lead-acid system (1,2). Further discussion in this chapter will be focused on the Li-ion battery system.

1.2 Basic electrochemical cell

The basic concept of an electrochemical cell is that this system converts chemical energy into electrical energy. In general, there are five components that constitute an electrochemical cell. These components are two electrodes, electrolyte, and two current collectors. The main function of the electrodes is to be reduced or oxidized over a potential range measured in volts (V). The electrolyte serves as an ionic conductor between the electrodes and must be electronically insulating. The current collectors are an electrically conducting material, usually a metal, that are directly in contact with each electrode. The current collectors are attached to each other by an external circuit. (2,4).

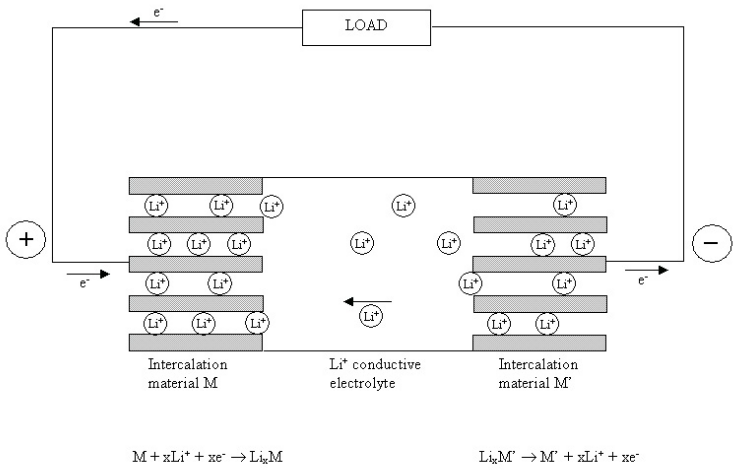

Figure 1-1 Schematic of an electrochemical cell

An electrochemical cell functions because of the potential difference between the two electrodes. It is energetically favourable for the two electrodes to come towards an equilibrium potential that is lower than the initial open-circuit cell potential where they are stable. Equilibrium between the electrodes is achieved by the oxidation of one electrode

and the reduction of the other electrode. The electrode that is reduced is called the cathode, while the electrode that is oxidized is called the anode. These reactions are accomplished by two distinct paths for ions and electrons. The electrons travel through the external circuit from the anode to the cathode. At the same time, the ions travel in the same direction as the electrons between the two electrodes through the electrolyte. This completes the redox reaction of the two electrodes.

The work that is performed from this reaction occurs at the external circuit. The amount of energy that the cell contains may also be controlled at the external electric circuit. The rate that the electrons flow or the current in the circuit may be regulated and can also be stopped by placing a physical break into the circuit. Once the potential difference between the electrodes reduces to zero Volts, no electrons will flow and the system stops to perform work. The process described above is called cell discharge.

In a rechargeable system, the electronic current flow is reversed through an external power source. At the same time, the ions will flow back to reduce the original electrode via the electrolyte and the potential difference between the electrodes will increase. Ideally, the amount of energy that was put into the system while under charge would equal the amount of energy that could be taken out of the system under discharge. This can never be the case due to entropy loss such as heat, and chemical side reactions in the cell.

1.3 Thermodynamics of an electrochemical cell

When discussing thermodynamics of an electrochemical cell, it is a custom practice to consider the partial change of Gibbs' free energy ∂G of an electrode with the progression of reduction or oxidation of the electrode, ∂n (2). This ratio is expressed as the chemical potential, μ, and is presented in Equation 1.1

$$\mu = \frac{\partial G}{\partial n} \tag{1.1}$$

In an electrochemical cell, the change of Gibbs' free energy, ΔG, is equal to the difference between the chemical potentials, μ_c and μ_a, of the component that was transferred through the electrolyte in its ionized form (e.g. Li) in the cathode and anode, respectively. This is presented in Equation (1.2) as

$$\Delta G = \mu_c - \mu_a \tag{1.2}$$

The electric potential, E, is directly related to the change of Gibbs' free energy by the following relation,

$$\Delta G = -nFE \tag{1.3}$$

where n is the number of electrons involved in the electrochemical reaction and F is Faraday's constant. By combining Equations (1.2) and (1.3), the electric potential of the cell is correlated with the difference of the chemical potentials defined above. Thus,

$$E = -\frac{(\mu_c - \mu_a)}{nF} \tag{1.4}$$

Chapter 5 of this thesis will discuss in more detail the thermodynamics of the Li-ion battery system.

1.4 Li-ion battery system

One of the most interesting rechargeable battery systems, that is being researched today, is the Li-ion battery system. This system is very attractive due to it's high energy density when compared to other rechargeable battery systems as presented in Figure 1-2 (4).

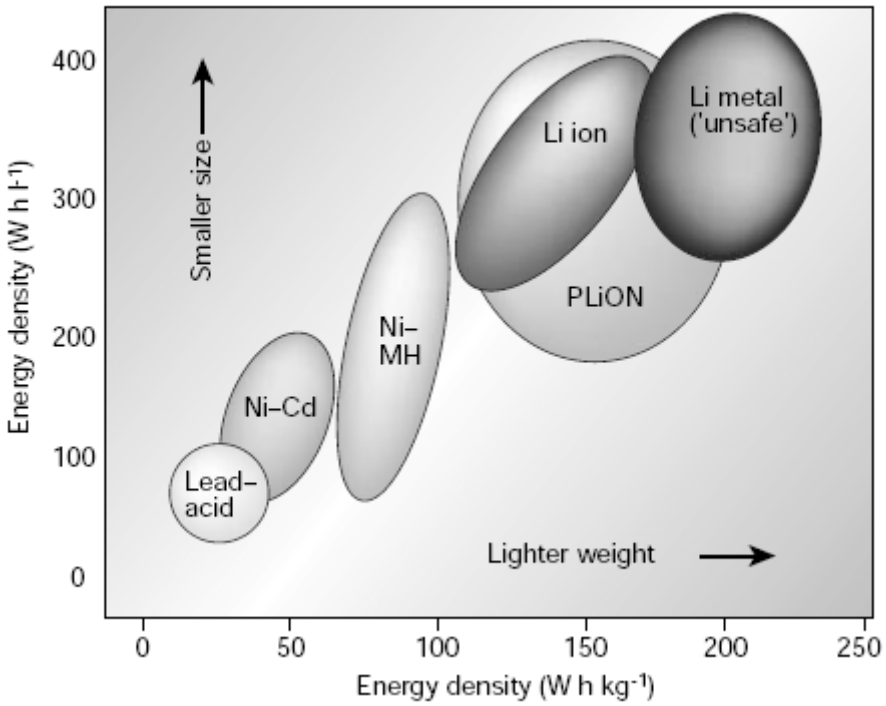

Figure 1-2 A graphic description of the volume of energy density to the weight of energy density for various battery systems from ref. (4)

The Li-ion battery system shuttles lithium between the two electrodes where one electrode is the Li source while the other electrode is a Li sink. Lithium is an ideal material for battery applications because it is one of the lightest elements in the Periodic Table and it possesses a high reducing potential (-3.04 V versus the standard hydrogen electrode). This combination makes the theoretical specific capacity extremely high (3862 Ah/kg), which is desirable for an energy storage device (1,5).

Early attempts to harness this energy used lithium metal as an anode and an intercalating or Li-ion insertion material as a cathode. This system failed due to dendrite formation on the lithium electrode as the cell underwent repeated discharge to charge cycles. The dendrites would build over a period of cycles until a physical short circuit between the electrodes would end the cell's life (2). In addition, safety was an issue, since lith-

ium metal can oxidize violently to form lithium nitride, Li_3N, and lithium oxide, Li_2O, in normal air (4).

One of the first approaches to circumvent the Li metal problem was to use a Li-ion intercalating material for both electrodes. This concept was demonstrated as early as the mid 1970's to the early 1980's that led to the Li-ion battery technology (6,7). This technology solved the Li metal problem by using only Li atoms to reduce one of the two intercalating electrode materials. Dendrite formation was no longer a problem, because the intercalating material was able to accept Li^+ ions into its structure. However, because Li metal was not used in the Li-ion intercalating strategy, the specific capacity was significantly reduced to a fraction of the theoretical specific capacity for Li metal. In 1991 the Sony Corporation was the first private company to market this technology using a $LiCoO_2$/carbon electrode couple (2,4).

1.4.1 Materials used in the Li-ion battery system

1.4.1.1 Positive electrode materials overview

Since the Li-ion battery concept was focused on intercalating electrodes, it was possible to construct a cell where the initial lithium source resides at the positive electrode. This battery design worked because there were many known Li-metal oxides that were stable in air and possessed a relatively high potential (8,9). Two of the earliest Li-metal oxides that were studied were $LiNiO_2$ and $LiCoO_2$. These materials adopted a layered structure that allowed Li atoms to exit and enter the sites in between the alternating planes in the metal oxides. Although $LiNiO_2$ would theoretically possess a greater specific capacity, the $LiCoO_2$ was more stable, when Li atoms were removed from the structure (10-12). For this reason, most of the commercial batteries use $LiCoO_2$, or a hybrid of the two aforementioned material as the positive electrode (13).

An alternative cathode material is $LiMn_2O_4$ that adopts a cubic spinel structure (14,15). Although the $LiMn_2O_4$ spinel material possesses a similar potential (approximately 4V), this material has a few advantages over the layered structure. Firstly, it was cheaper to produce since the materials were more abundant than Ni or Co. Secondly, it was more environmentally friendly, or less toxic than Ni or Co (16). Thirdly, it possessed a three-

dimensional structure so that Li atoms could enter and exit the structure in a three-dimensional manner (17). This is in contrast to the layered structure of $LiNiO_2$ and $LiCoO_2$ where the Li atoms are mobile in only a two-dimensional conductive pathway.

However, $LiMn_2O_4$ has a few disadvantages. The practical specific capacity for this material is 120mAh/g. This capacity is approximately 10% less than that of the layered structure. Another drawback is that the stoichiometric spinel could change from cubic to an orthogonal structure at just below room temperature due to a Jahn-Teller distortion caused by the Mn^{3+} cations (18-21). Furthermore, the cycle life is limited and storage under elevated temperature conditions decreased the performance of this material (22,23). Recent reports have mentioned coating $LiMn_2O_4$ with $LiCoO_2$ that may have solved some of these problems (24-27). Further discussions of $LiMn_2O_4$ will be presented in a later part of this chapter.

Recently, by doping Ni in place of Mn in the $LiMn_2O_4$ spinel, a new class of 5 V cathodes has been reported (28). The obvious advantage for this class of cathodes is the increase in power density. One of the main obstacles concerning this material is the structural stability of these materials and the potential stability of the electrolytes that are currently used. It is known that the possibility of manganese dissolution occurs at either elevated temperatures, or at higher potentials. This problem directly affects the life of this battery system (29,30).

The latest successful material that is used for the Li-ion battery system is $LiFePO_4$. The $LiFePO_4$ adopts an olivine structure. This material possesses a very stable potential at 3.4 V for approximately 90% of its specific capacity. In addition, this material is extremely stable at elevated temperatures (up to 85^{o}C) over a long cycle life (31,32). The greatest disadvantage is the low electrical conductivity. This problem leads to a high-cell resistance and thus a poor cell performance. Recent advances to improve the conductivity such as carbon coating the particles of this material have made this material a promising candidate as a next generation of positive electrode materials (33).

1.4.1.2 Negative electrode materials overview

One of the first materials that have been examined after Li metal as a negative electrode is carbon. This material can accept one Li atom per six carbons in its structure. Because of its high Li uptake and relatively light density, the theoretical specific capacity is considered high at 372 mAh/g. Through advances in material preparation, the practical capacity is very close to the theoretical value. Although the open-circuit potential of this material is 3.5 V versus Li metal, the potential drops dramatically (below 0.1 V) once Li atoms are intercalated into its structure. Thus, practically the full potential of Li metal can be realized (34,35).

Despite obvious advantages such as low cost, high specific capacity, and an intercalation potential that is close to lithium metal, there are a few problems with carbon. Firstly, this material is known to react with the electrolyte as Li is intercalated into the carbon. This reaction forms a so called solid-electrolyte interface (SEI) layer (34). The formation of this layer creates an irreversible capacity loss of approximately 10 to 15% (36,37). Secondly, since the potential of the intercalated carbon is very close to the potential of Li metal, Li metal plating on the carbon under higher charging current densities is a concern. Li plating is a safety risk that is similar to the risk of using Li metal anodes (37).

An alternative material for carbon is metal oxides such as TiO_2, or spinel metal oxide such as $Li_4Ti_5O_{12}$. For the $Li_4Ti_5O_{12}$ spinel material, many groups have found that it possesses attractive qualities as an anode material. Some of these qualities include a practical capacity of 170 mAh/g, an extremely stable potential of 1.55 V versus Li metal for over 90% of its capacity, and an extremely low volume change of the material that is less than 0.1% during the course of cycling (38,39). Because the potential is significantly greater than that of carbon, the risk of Li metal plating is significantly reduced.

The latest class of negative electrodes that has been reported comprises the nano-metal oxides. Tarascon et al. have recently reported a significant increase in specific capacity for some nano-metal oxides. This significant increase of capacity is attributed to the reversibility of Li_2O. It has been previously thought that Li_2O was irreversible but this group has argued that properties in the nano region do not reflect the same properties as in the bulk (40).

1.4.1.3 Electrolyte overview

Two major types of electrolyte that are commercially being used are the solid-state Li-polymer and a nonaqueous Li-electrolyte. In general, the Li-polymer electrolyte contains a Li salt that is dissolved by a polymer solvent. Once the Li salt is dissolved, Li^+ ions can hop along the backbone of the polymer chain (4). The advantage is that the electrolyte is solid state. Thus, manufacturing the battery is easier and because electrolyte spillage is not an issue, the battery is more safe when comparing to batteries that uses liquid electrolytes. The disadvantage is that the ionic conductivity is rather low at room temperature. However, recently Scrosati et al. have reported a significant improvement of the ionic conductivity of polymer electrolytes by the addition of nano-sized metal oxides in the polymer, such as TiO_2 (41).

The second type of electrolyte generally uses an organic solvent that dissolves a Li salt. There have been many salts and organic solvents that have been used in the past. Of these, one of the most commonly reported liquid electrolyte is the lithium fluorophosphate ($LiPF_6$) that is dissolved in a mixture of ethylene carbonate (EC), dimethyl carbonate (DMC) or propylene carbonate (PC). This electrolyte is a particularly good ionic conductor at room temperature (up to 10^{-3} S/cm^2), and is stable up to 5V versus Li metal (4). Some of the disadvantages are the flammability of the electrolyte and the limited temperature range that the electrolyte can be operated, i.e., in the range of 10-50^{O}C (42). Recently, a new class of liquid electrolytes that uses a rather large anion and called ionic liquids are being researched. These electrolytes are stable at higher temperatures and have a similar ionic conductivity than that of the early liquid electrolytes (43).

1.4.2 Electrode electrolyte interface and electrolyte degradation

According to the Bockris and Reddey, most of the action in electrochemistry takes place at the interfaces of the electrodes and electrolyte. However studying this area of electrochemistry is rather tedious and complex. When considering interfaces in electrochemistry, the concept of the Helmholtz layer has been widely accepted for more than 100 years. In the 1960's the concept of the overcharge potential explains some of the dynamics of the electrode electrolyte interfaces (44).

In the Li-ion battery field, the interface between the electrolyte and anode has been studied the most while little attention has been given towards the cathode-electrolyte interface. It has been accepted generally that a solid electrolyte interface (SEI) layer is formed on the anode at the early stages of lithium intercalation, or alloying of the anode where the local potential is below 1V (42). During this process, the electrolyte reacts with the electrode to form this layer. This layer is generally viewed as a passivation layer that acts as a protective coating that prevents further degradation of the electrode or electrolyte. To date, evidence of the SEI layer has been given indirectly through various electrochemical techniques. In some instances, the SEI layer may increases the cell resistance over time and, therefore, reduces the service life of the cell (34). There have also been reports that this may be the case at the cathode electrode as well but the validity of these reports is currently debateable (42). Figure 1-3 presents a schematic of the interfacial layers. (45)

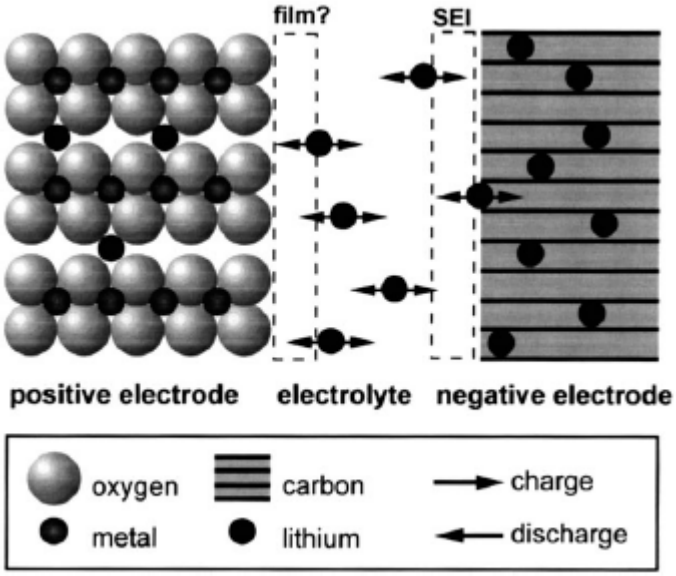

Figure 1-3 Schematic of the electrochemical cell with the SEI layer from ref. (45)

Other forms of degradation of the electrolyte have been reported also. Among these is the reaction of residual water with the lithium salt in nonaqueous electrolytes. In the case of electrolytes that use $LiPF_6$ salt, the possibility of producing hydrofluoric acid

has been reported (4,30). If acids were introduced into the electrolyte that use a $LiMn_2O_4$ electrode, the Mn would tend to dissolve into the electrolyte and this reduces the cycle life of the $LiMn_2O_4$ electrode at especially higher temperatures (46,47).

1.4.3 Battery design

Although there are many cell configurations, the most common consumer battery designs are the coin cell, wound cell, prismatic cell, and the flat cell (2,3,48). The coin cell design is a straight forward design where the electrodes are parallel to each other. These electrodes are separated usually by a polyethylene sheet that contains a liquid electrolyte. These materials are placed in a thin cylindrical metal can which is sealed by a metal lid. To prevent an electrical short circuiting, a polymer gasket seals the lid to the can. Thus, the can is usually one electrode pole while the lid is the other electrode pole of the cell. The name of this design comes from the fact that its casing resembles a coin. The second most common design is the wound cell design. This design uses long strips of electrodes and separator that are wound inside and are placed in a long cylindrical can. A similar system that is used to seal the coin cell design also seals this cell design. The prismatic cell is similar to the cylindrical cell in that it is a wound cell that is flat. The flat cell design contains alternating plates of electrodes and separators. Each electrode plate possesses a tab that is welded to all of the other tabs of its respective electrodes. Figure 1-4 (a-d) presents four common cell designs from reference (4).

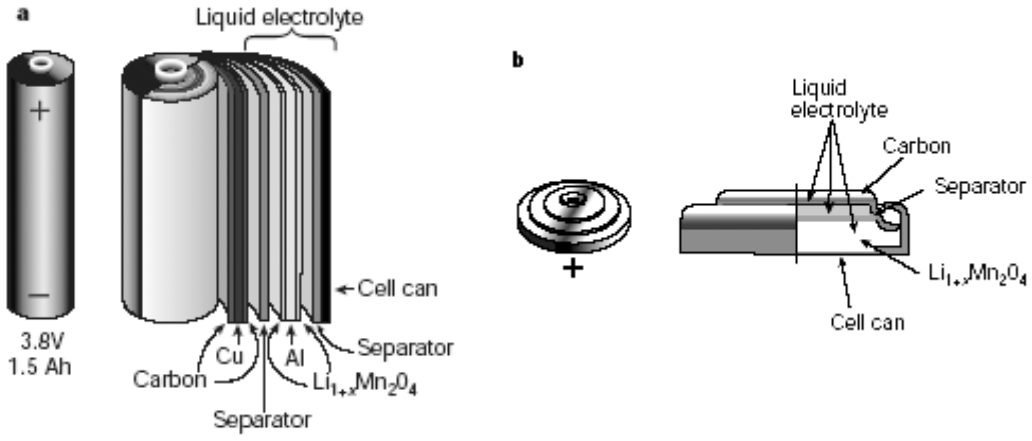

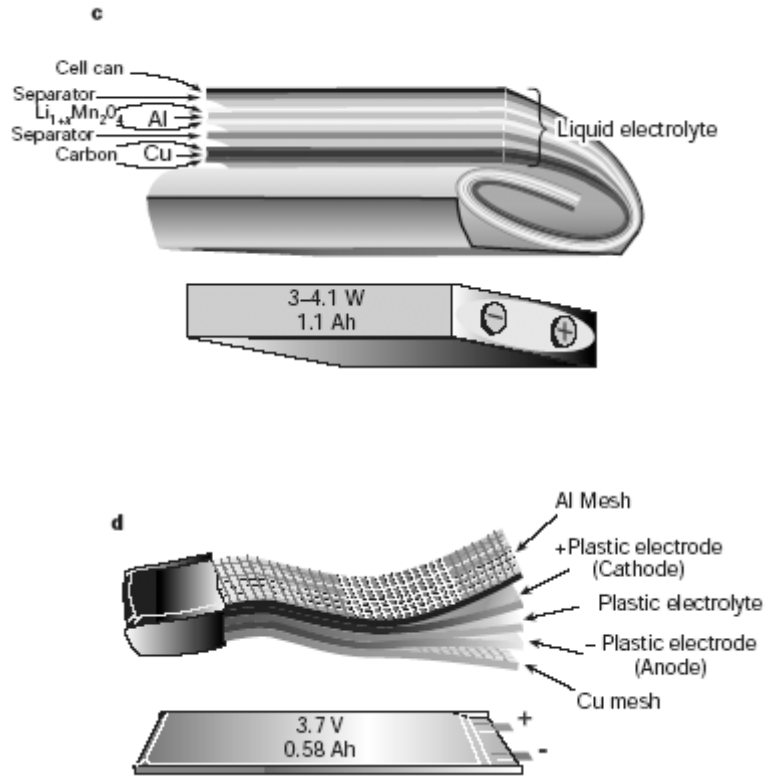

Figure 1-4 Four common cell designs: a. cylindrical, b. coin, c. prismatic, and d. flat from ref. (4)

1.5 Thesis overview

This thesis examines two specific materials that are used as an electrode in the Li-ion battery system. These are $Li_4Ti_5O_{12}$ and $LiMn_2O_4$ spinel materials. In the case of $Li_4Ti_5O_{12}$, the formation and the stability of this material are studied when treated with an acidic solution. In the case of $LiMn_2O_4$, magnetic properties of the delithiated spinel by an acid are compared with the substituted $LiMn_2O_4$. Finally, the corrosion potential of $LiMn_2O_4$ is correlated to the potential of an electrochemical cell as a function of Li-ion extraction.

A brief description of the spinel structure and a more detailed description of both materials are discussed in the following sections of this chapter. Included in these discussions is a brief introduction of the topics presented in this thesis.

1.5.1 Spinel structure

The spinel structure is a cubic structure which lies in the Fd3m space group that consists of octahedral and tetrahedral sites. There are in total 56 atoms per unit cell that include 24 cations and 32 anions that forms the spinel framework. The empirical formula of the spinel structure is AB_2X_4 where the A cations reside on the 8a tetrahedral sites, while the B cations reside on the 16d octahedral sites. The X anions are placed on the 32e sites in a cubic close-packed (ccp) array. The 16d octahedra share edges with the 8a tetrahedral and the 8a tetrahedra also share faces with the 16c octahedra (49). Figure 1-5 presents an illustration of the spinel structure from reference (50).

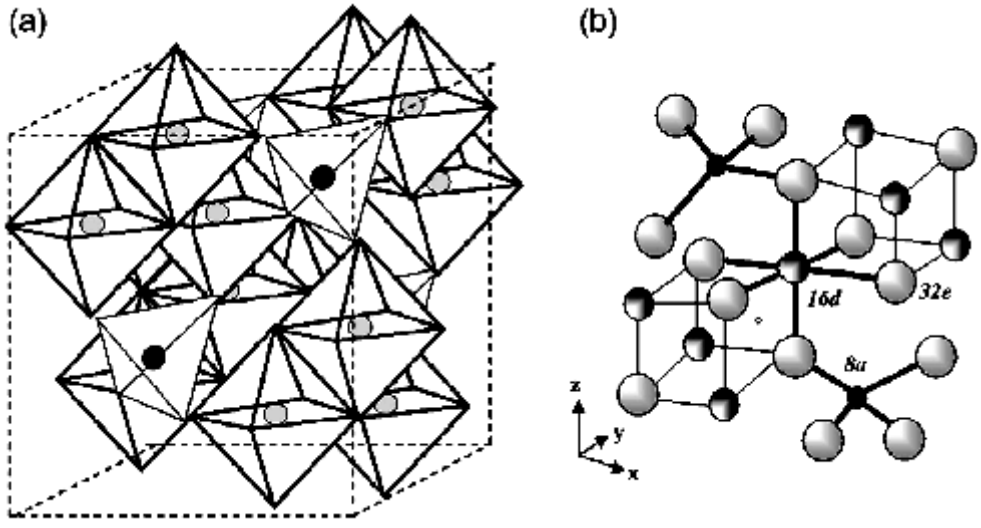

Figure 1-5 Schematic of the spinel structure: (a) presents octahedral and tetrahedral sites of the spinel, X anions resides on the edges of these sites at the 32e sites, darken circles represent A cations in the tetrahedrons at the 8a sites, lightly coloured circles represent B cations in the octahedrons at the 16d sites, (b) presents the location of the sites in the spinel from ref.(50)

1.5.2 Lithium titanium oxide spinel

1.5.2.1 Structural overview

The lithium titanium oxide spinel ($Li_4Ti_5O_{12}$) used as an anode in Li-ion batteries is a single phase in the Li-Ti-O ternary system. It falls at one of the end points that is related to the $LiTi_2O_4$ spinel phase. In the $Li_4Ti_5O_{12}$ spinel, 1/6 of the Ti ions are substituted by Li^+ ions. Thus, in spinel notation, the empirical formula is $Li[Li_{1/3}Ti_{5/3}]O_4$ where the cations in the square brackets represent the cations on the octahedral sites (51).

1.5.2.2 Fabrication of $Li_4Ti_5O_{12}$

Many groups have reported the production of this material. In essence, two routes have been explored. The first route is the solid-state reaction between TiO_2 and a Li salt. The solid-state reaction uses a thoroughly mixed precursor that was heated to approximately 800^OC in air for as long as 24 hours. The resulting material is a white powder that possesses the spinel structure. This route is the most direct one for the production of this material and the average particle size of the product is in the range of 5 to 10 microns (52-54).

The second route is a sol-gel method reported by Bach et al.(55,56). This method uses Ti-isopropoxide mixed with lithium acetate. The hydrolysis of the Ti-isopropoxide produces a white milky substance. This mixture is dried and heated to 500^OC in air to form the spinel powder. The particle size of this powder can be as small as 9 nm and it has been shown that the electrochemical performance of this material is better than that of the material with micron-sized particles (57).

Chapter 2 of this thesis examines the formation of $Li_4Ti_5O_{12}$ using in-situ XRD as the precursors are heated. In this chapter both solid-state and sol-gel synthesis routes are studied. The phases that are formed and their relationships to the phase diagram are also discussed.

1.5.2.3 Electrochemical characteristics

$Li_4Ti_5O_{12}$ is typically used as an anode electrode and possesses a theoretical capacity of 175mAh/g. By using the empirical formula $Li_4Ti_5O_{12}$, this spinel can accept up to 3 mols of Li atoms to form $Li_7Ti_5O_{12}$ upon discharge. This reduction is reversible upon charging and the material is oxidized back to $Li_4Ti_5O_{12}$. Equation (1.5) illustrates the reduction and oxidation reactions.

$$Li_4Ti_5O_{12} + 3Li^+ + 3e^- \rightleftarrows Li_7Ti_5O_{12} \tag{1.5}$$

The electrochemical performance of this material is rather unique, if compared to other intercalating materials. One unique feature is the flat potential (approximately 1.55V versus Li metal) for over 90% of its capacity during intercalation and deintercalation of Li^+ ions. Also the polarization is less important when compared to other metal oxide electrodes at similar current densities. It is believed that the substantial flat potential region is due to two phases, i.e., $Li_4Ti_5O_{12}$ and $Li_7Ti_5O_{12}$, which are always present upon discharge and charge (58,59).

Another unique feature is that the change in volume is particularly small when this material intercalates and deintercalates Li^+ ions as the cell charges and discharges, respectively. Initial reports by Ohzuku et al. have reported that this material experiences zero strain as the spinel accepts or releases Li^+ ions into and out of its structure, respectively (38). Later reports by Scharner and co-workers have reported through the use of high-angle X-ray diffraction (XRD) a volume change less than 0.20% as the spinel intercalates Li^+ ions (60). It is thought that this stability results in a high practical capacity (over 95% of the theoretical) and very small capacity fading over the cell's life time.

Although the cycling stability of $Li_4Ti_5O_{12}$ has been well documented, the stability in acidic solutions has not been reported. As mentioned previously, Li electrolytes may contain acid due to its reaction with residual water. Thus, $Li_4Ti_5O_{12}$ may be exposed to an acidic solution when used as an electrode material. Chapter 3 of this thesis examines the stability of $Li_4Ti_5O_{12}$, when in contact with an acidic solution. This chapter discusses the reaction that takes place between $Li_4Ti_5O_{12}$ in an acidic solution, the structure of the resulting material through neutron diffraction, and its impact on its electrochemical performance.

1.5.3 Lithium manganese oxide spinel

For the stoichiometric lithium manganese oxide spinel, $LiMn_2O_4$, the Li^+ ions reside in the 8a tetrahedral sites, while the Mn cations are in the 16d octahedral sites. This particular material is a unique material in that it may accept or release Li^+ ions into or from its structure. Upon the removal of all Li^+ ions from its structure, the resulting material changes to the λ–MnO_2 spinel phase. The stoichoimetric spinel may also accept Li^+ ions to form $Li_2Mn_2O_4$ that adopts a hexagonal structure. Equations (1.6) and (1.7) show the reduction and oxidation of stoichiometric $LiMn_2O_4$, repectively

$$LiMn_2O_{4(cubic)} + Li^+ + e^- \rightleftarrows Li_2Mn_2O_{4(hexagonal)} \tag{1.6}$$

$$LiMn_2O_{4(cubic)} \rightleftarrows 2\lambda - MnO_{2(cubic)} + Li^+ + e^- \tag{1.7}$$

Although both reactions are reversible, the transformation between the cubic and hexagonal structure, as shown in Equation (1.6) results in poor electrochemical reversibility (61-63). Thus, for battery applications it is interesting to cycle this material at a potential above the stoichiometric $LiMn_2O_4$ phase where Li-ion extraction takes place.

1.5.3.1 Jahn-Teller distortion of $LiMn_2O_4$

It is known that the Mn^{3+} cations distort the octahedral site, if the electrons in the 3d-band of this cation are placed in a high-spin electronic configuration. The main reason for this phenomenon is that the high-spin Mn^{3+} cation possesses four 3d-band electrons. This electronic band splits into two main degenerate energy levels as a result of crystal-field splitting. There are three 3d electron orbitals that form the t_{2g} energy level which are d_{xy}, d_{xz}, and d_{yz}. The e_g energy level is greater in energy than the t_{2g} energy level and consists of two 3d electron orbitals $d_{x^2-y^2}$ and d_{z^2}. The electron orbitals in the t_{2g} energy level do not bond with any oxygen ions. The e_g energy level possesses two electron orbitals that directly face an orbital of the oxide ion. These orbitals are called antibonding orbitals because the energy levels of these orbitals are degenerate. If Hund's rule is obeyed, each electron must be placed in its own unique orbital. Thus, the three t_{2g} orbitals and one of the e_g orbitals in a high-spin configuration are half-filled. Because of the degeneracy of the e_g orbitals, energy can be gained, if the oxide ions along the z-axis

move away from the d_{z2} orbital. Thus, leading to a more stable d_z^2 orbital compared to the d_x^2-d_y^2 orbital. This movement causes a distortion of the octahedral site to form an elongated octahedron that is known as the Jahn-Teller distortion. On a macro-scale, the structure is transformed from a cubic to a hexagonal structure (64). The energy levels for the Mn cation in an octahedral site are pictured in Figure 1-6a from reference (65). The energy splitting of the e_g orbitals from cubic to tetragongal structures is presented in Figure 1-6b from reference (18).

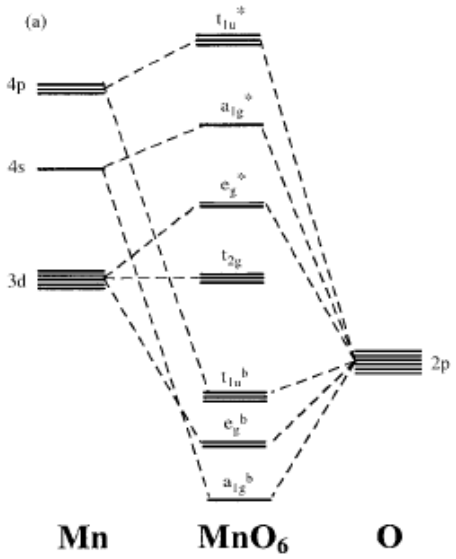

Figure 1-6a Crystal-field energy splitting of Mn in an octahedral site from ref. (65)

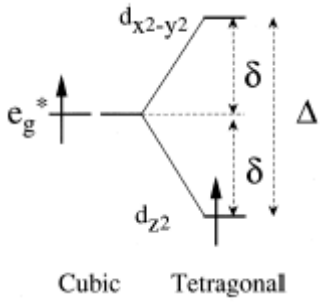

Figure 1-6b The energy splitting with elongated z-axis of the e_g orbitals from cubic to tetragonal structures from ref. (18)

In the case of the stoichiometric spinel, $LiMn_2O_4$, exactly half of the Mn cations are in the 3+ oxidation state, while the other half is in the 4+ oxidation state. Curiously enough, the stoichiometric spinel is cubic above room temperature, but orthogonal when slightly cooled below room temperature. It is thought that this phenomenon is due to charge ordering of the spinel that gives rise to a cooperative Jahn-Teller distortion of the cubic material (66-70). However, if some of the Mn cations are substituted for Li^+ ions, less than half of the total Mn cations in this spinel is in the 3+ oxidation state, while the rest of the cations is in the 4+ oxidation state. Since Mn^{4+} cations cannot cause a Jahn-Teller distortion, the substituted spinel, $Li_{(1+\delta)}Mn_{(2-\delta)}O_4$ for $0.33 \leq \delta \leq 0$, where Li^+ ions replace Mn cations, is resistant to a structural change as the temperature decreases below room temperature (71).

One experimental technique that determines the spin configuration of the Mn^{3+} cations is measuring the magnetic susceptibility of these materials. There have been conflicting results reported by groups that have performed magnetic susceptibility measurements on the stoichiometric $LiMn_2O_4$ spinel. One of the earliest groups reported that 80% of the Mn^{3+} cations are in a high-spin configuration, while 20% is in a low-spin configuration (72,73). Later, other groups have reported that 100% of the Mn^{3+} cations are in a high-spin configuration. Furthermore, a discrepancy in the Weiss temperature has been reported as the average Mn oxidation state of the spinel increases from 3.5 in the stoichiometric $LiMn_2O_4$ spinel to 4 as a result of either Li-ion extraction or by the substitution of Li for Mn in the case of substituted spinels (74,75).

Chapter 4 in this thesis examines the magnetic susceptibility of Li-extracted spinel by acidic treatment and Li-substituted spinels as the average Mn oxidation state increases. In addition, an explanation of the spin states of these spinels is presented. Lastly, an error and the correction of the error found in a previous report is presented that supports the current findings.

1.5.3.2 The potential of $LiMn_2O_4$

As mentioned earlier, Li^+ ions can be extracted or inserted from or into the stoichiometric $LiMn_2O_4$ spinel, respectively. The full potential window for this spinel is presented in Figure 1-7 (76).

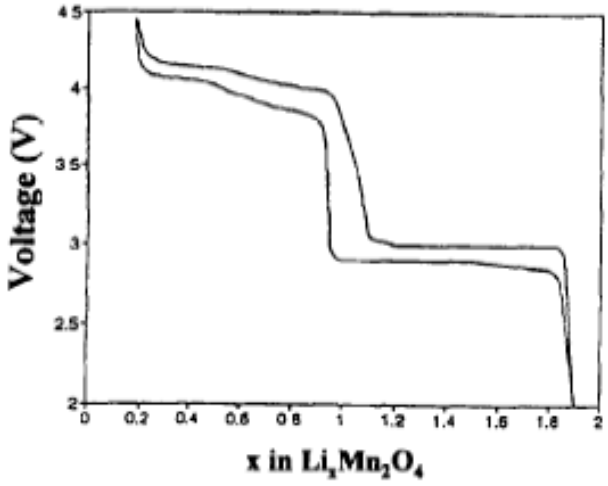

Figure 1-7 The potential of LixMn2O4 as a function of x Li+ ions from ref. (76)

From previous reports, the open-circuit potential of $LiMn_2O_4$ spinel versus Li metal is 3.5 V. If Li atoms are inserted into the structure, the potential drops to approximately 3 V where a plateau is observed. This plateau indicates the coexistence of two phases, which are $LiMn_2O_4$ and $Li_2Mn_2O_4$. This voltage plateau continues until a single phase of $Li_2Mn_2O_4$ is reached.

If Li atoms are extracted from $LiMn_2O_4$, the potential increases from 3.5 V to approximately 3.9 V where the first plateau is observed up to a composition of $Li_{0.5}Mn_2O_4$. A second plateau is observed at approximately 4.1V, where λ-MnO_2 forms and most Li^+ ions are extracted from the material. For Li-ion battery applications, the Li extraction region is most interesting. Thus, this material is typically used as a 4 V cathode material for Li^+ ion delivery (76).

1.5.3.3 Measuring the potential of $LiMn_2O_4$ in aqueous solution

Hunter was one of the first researchers to report the extraction of Li^+ ions from $LiMn_2O_4$ using acidic solutions (77,78). This author named this spinel λ–MnO_2 where no cations in this spinel are in the tetrahedral positions. Kelder and co-workers have found a similarity between the potential curve of the electrochemical extraction of Li^+ ions from $LiMn_2O_4$ and the potential of the glass electrode (pH) when chemically extracting Li^+ ions from the same material (79).

Chapter 5 presents the potential curves of an aqueous solution containing $LiMn_2O_4$ particles using a Pt/Ag-AgCl reference electrode as the pH of the solution decreases. A linear relationship was found between the potential of the Pt/Ag-AgCl electrode and the pH. In addition, an explanation of the potential curve as a function of Li-ion extraction from an electrochemical cell and the pH curve is also presented.

1.5.4 Experimental techniques for electrochemical testing

1.5.4.1 Electrode foil preparation

When testing electrode materials, thin sheets are fabricated for ease of handling and to insure optimal electrochemical performance. Usually the starting electrode material is in the form of a powder of up to 30 micron particle size. In order to fabricate the sheets of electrodes, the electrode material is casted onto a thin sheet of a metal substrate that will serve as a current collector. A poly-vinyl diflouride (PVDF) polymer is used as a binder between the particles and the substrate.

Since the materials in this thesis are semiconductors, carbon is used as an electronic conductive agent. In general, there are two types of carbon that is used. The first type is the flaky type while the other is the spherical type. In an ideal situation, the flaky carbons are thin plates that form an electrical network within the electrode. The spherical carbon acts as a dispersion agent in order to obtain a homogeneous electrode. Since carbon will not intercalate Li ions below 0.1 V, the carbon will not interfere with the intercalation/deintercalation of material above that potential. There is an optimal loading between the amount of active material and carbon in the electrode in order for it to become active. This loading depends usually on the particle size or surface area of the active

material. As a general rule, the smaller the particle size of the active material the larger the surface area and hence, more carbon must be available for the percolation of Li-ion for intercalation.

The mixture of active, non-active, and binder materials is well mixed either by mortar and pestle, or by gently ball milling. A slurry is formed when liquid n-methyl pyrrolidone (NMP) is added to this mixture. This liquid acts as a solvent towards the PVDF binder and will evaporate out of the mixture once heated. The amount of NMP used for the slurry depends on the amount of carbon and the particle size of the active material used in the mixture. In general, the more viscous the slurry is results in a more thinner electrode film.

To caste an electrode film, the doctor-blade technique is used. A predetermined thickness of the blade to the metal substrate is used. The slurry is poured from a beaker onto the substrate that forms a small pool of slurry that is in front of the blade. The blade is then pushed towards and past the slurry pool forming a thin film of slurry on the substrate. The casted film is placed in a convection oven at $120^{O}C$ to remove the NMP. To insure contact between the carbon, substrate, and active material, calendaring or compressing the foil is required. In this thesis, the final film is approximately 35% porous which seems to provide a good balance between the electrical contact of the active material to the current collector and to allow sufficient contact of the electrolyte to the active material.

Care for the selection of the metal substrate is important in order to insure that this substrate is used only for current collection. For example, Li^{+} ions are known to alloy with Al metal below 0.5 V versus Li metal, but Cu metal does not. Thus, the Cu substrate is used to test materials below that potential. Conversely, for potentials above 3 V versus Li metal results in the oxidation of Cu metal but not Al metal. The substrates that are used for the materials in this thesis are in general Al metal.

1.5.4.2 Coin Cells

For electrochemical performance analysis of a novel electrode material, coin cells were fabricated. The test material in the form of an electrode film, Li metal, and a polyethyl-

ene separator sheet were punched out as disks. These disks were placed in a coin cell can in the following sequence; electrode film, separator, and Li metal. Each coin cell contained only one set of this sequence. Liquid Li-conducting electrolyte was added before the can was sealed. A plastic gasket ring was inserted into the can along with a flat metal disk that sits on top of the electrode stack. A spring was placed on top of the flat disk in order to maintain pressure on the cell stack. Finally, the coin cell lid was crimped into the can using the plastic gasket as a seal and an electric insulator between the lid and the can. The sealed coin cell is complete with the lid as one pole and the can as the other pole of the electrochemical cell.

1.5.4.3 Electrochemical testing

Because of the potential stability of Li metal, this material can be used as a reference electrode. Additionally, Li metal provided a large Li source for the cell and can be used as a counter electrode as well. For typical electrochemical testing in this thesis, Li metal was used for both counter and reference electrodes. Thus, all measured potentials for a novel material in this thesis was measured against the potential of Li metal.

Electrochemical testing was performed using a MACCOR battery tester . This device was programmable and was able to collect and store performance data. This device contains multi-channels where several cells may be tested at a time. In addition, the accuracy of the current that is applied to the cell is specific to a unique channel. Some additional tests were carried out by using an Electrochem, galvanic/potentiostat device. This device can provide current-potential plots as well as performing impedance tests.

1.6 Outline of thesis

In this thesis, an investigation of two spinels, $Li_4Ti_5O_{12}$ and $LiMn_2O_4$, are performed in terms of formation and their reactivity towards acidic solutions.

In the case of $Li_4Ti_5O_{12}$, the formation of this material via solid-state or sol-gel routes are examined by using in-situ XRD which is presented in Chapter 2. By using this technique, the formation of $Li_4Ti_5O_{12}$ can be investigated in real time. From this investiga-

tion, it was found that the sol-gel synthesis process forms the spinel at a much lower temperature than the solid-state process. Furthermore, the spinel must form by reacting TiO_2 with an intermediate compoundand, Li_2TiO_3.

In Chapter 3, the reaction of $Li_4Ti_5O_{12}$ when in contact with an acidic solution is investigated. By using potentiometric titration of a solution that contains $Li_4Ti_5O_{12}$ particles with an acid, a buffer region in the potentiometric curve was observed. This means that acid was being neutralized by the $Li_4Ti_5O_{12}$ particles. Through the use of atomic absorption spectroscopy (AAS), Li^+ ions were found in the solution after titration. From this result, it was reasoned that an ion exchange between the protons of the acid and Li^+ ions from $Li_4Ti_5O_{12}$ occurred. Further evidence of ion exchange was given by using infra-red (IR) spectroscopy on the exchanged material. In this spectrum, peaks appeared at wave numbers where protons are known to reside in spinels.

The position of the exchanged protons was examined by using neutron diffraction. The position of these protons can be roughly described as alternating sheets of octahedrally positioned Li^+ and Ti^{4+} ions with tetrahedral 8a protons and Li^+ ions, and protons positioned on the 48f sites. A graphical illustration of the ion-exchanged spinel is presented in Chapter 3.

Through the use of thermogravimetric analysis (TGA), it was found that the weight loss of the ion-exchanged material was substantial after heating to $440^{O}C$. From X-ray diffraction (XRD), the spinel and anatase TiO_2 phases are present after heating the material beyond $440^{O}C$. It seemed that the protons completely exit the spinel structure as water when heated beyond $440^{O}C$. Two proposed reactions are presented in Chapter 3 that include the ion exchange and the change of the exchanged material that occurs when heated above $440^{O}C$.

Finally, electrochemical measurements of pristine $Li_4Ti_5O_{12}$ and the proton-exchanged spinel were performed using Li metal as a counter and reference electrode. The results show that as more protons are in the spinel structure, the potential deviates from a flat potential to a sloping potential as Li^+ ions intercalate and deintercalate from the spinel. Consequently, the capacity decreases as more protons are exchanged into the spinel. The potential curves are presented in Chapter 3.

In Chapter 4, magnetic susceptibility measurements were performed on $LiMn_2O_4$ as a function of Li-ion extraction and on Li-substituted manganese spinels using the Faraday method. The results show that magnetic moments for all samples lie on the theoretical line where 100% of the Mn^{3+} cations in these spinels are in a high-spin electronic configuration. This is in contrast to previous reports where it was concluded that 80% of Mn^{3+} cations are in a high-spin configuration and 20% of these cations are in a low-spin configuration.

In addition, the Weiss temperature of these materials show a similar trend from strongly negative to less negative as the average oxidation state of the Mn cations increases from 3.5 to 3.7. When the average Mn oxidation state increases beyond 3.7, there are two distinct trends of the Weiss temperature. One trend shows very little change in the Weiss temperature as the average Mn oxidation state increases from 3.7 to 3.9 when Li^+ ions are continuously removed from $LiMn_2O_4$. The other trend is a continuation of the original trend as the average Mn oxidation state increases by the substitution of Mn cations by Li^+ ions. An explanation for these results is also presented in this chapter.

Chapter 5 investigates the potential of a solution that contains $LiMn_2O_4$ particles as a function of pH and Li-ion extraction. It is well known that a disproportionation reaction of the Mn^{3+} cations from $LiMn_2O_4$ occurs when this material is in contact with an acidic solution. As the disproportionation reaction proceeds, Li^+ ions and Mn^{3+} cations are extracted from the $LiMn_2O_4$ spinel material. If one traces the pH of the solution as a function of Li-ion extraction, a similarity in the shape of the curve is observed between the pH curve and the potential curve of an electrochemical cell as Li^+ ions are extracted from the $LiMn_2O_4$ spinel. This chapter finds that the open circuit potential of the solution as a function of Li-ion extraction has the same shape and, more importantly, similar in potential when both potentials from the electrochemical curve and from the solution are normalized to the hydrogen electrode. An explanation for these results is presented in this chapter.

1.7 References

1. Dell, R. *Chemistry In Britain* **2000,** *36*(3), 34-39.

2. Winter, M.; Brodd, R. *Chem.Rev.* **2004,** *104,* 4245.

3. Dell, R. *Solid State Ionics* **2000,** *134,* 139.

4. Tarascon, J. M.; Armand, M. *Nature* **2001,** *414*(6861), 359-367.

5. Beck, F.; Ruetschi, P. *Electrochim. Acta* **2000,** *45,* 2467.

6. Murphy, D. W.; Carides, J. N.; Di Salvo, F. J. *Mater. Res. Bull.* **1977,** *12,* 825-830.

7. Padula, A.; Patriarca, M.; Scrosati, B. *Solid State Ionics* **1983,** *9-10,* 365-370.

8. Blasse, G. *Journal Of Physics And Chemistry Of Solids* **1966,** *27,* 383-389.

9. Blasse, G. *Crystal Chemistry and some Magnetic Properties of Mixed Metal Oxides with Spinel Structure*, *Ph.D.Thesis, Leiden University, Leiden, The Netherlands* **1964**.

10. Lu, C. H.; Yeh, P. Y. *J. European Ceram. Soc.* **2002,** *22,* 673.

11. Ebner, W.; Fouchard, D., Xie, L. *Solid State Ionics* **1994,** *69*(3-4), 238-256.

12. Arai, H.; Okada, S., Sakurai, Y. *Solid State Ionics* **1997,** *95,* 275.

13. Li, W.; Currie, C. *J Electrochem. Soc.* **1997,** *144*(8), 2773-2779.

14. Thackeray, M. M.; Johnson, C. S.; de Picciotto, L. A.; Bruce, P. G.; Goodenough, J. B. *Mater. Res. Bull.* **1983,** *19,* 179-187.

15. Thackeray, M. M.; David, W. I. F.; Bruce, P. G.; Goodenough, J. B. *Mater. Res. Bull.* **1983,** *18,* 461-472.

16. Yamada, A.; Tanaka, M.; Tanaka, K.; Sekai, K. *J.Power Sources* **1999,** *82,* 73-78.

17. Thackeray, M. M.; de Picciotto, L. A.; de Kock, A.; Johnson, P. J.; Nicholas, V. A.; Adendorf, K. T. *J. Power Sources* **1987,** *21,* 1-8.

18. Yamada, A.; Tanaka, M.; Tanaka, K.; Sekai, K. *J. Power Sources* **1999,** *82,* 73-78.

19. Yamaguchi, H.; Yamada, A.; Uwe, H. *Phy. Rev. B* **1998,** *58*(1), 8-11.

20. Shimakawa, Y.; Numata, T.; Tabuchi, J. *J. Solid State Chem.* **1997,** *131*(1), 138-143.

21. Yamada, A.; Tanaka, M. *Mater. Res. Bull.* **1995,** *30*(6), 715-721.

22. Yamane, H.; Saitoh, M.; Sano, M.; Fujita, M.; Sakata, M.; Takada, M.; Nishibori, E.; Tanaka, N. *J. Electrochem. Soc.* **2002,** *149*(12), A1514-A1520.

23. Ma, S. H.; Noguchi, H.; Yoshio, M. *J. Power Sources* **2001,** *97-8,* 385-388.

24. Liu, Z. L.; Wang, H. B.; Fang, L.; Lee, J. Y.; Gan, L. M. *J. Power Sources* **2002,** *104*(1), 101-107.

25. Park, S. C.; Kim, Y. M.; Han, S. C.; Ahn, S.; Ku, C. H.; Lee, J. Y. *J. Power Sources* **2002,** *107*(1), 42-47.

26. Park, S. C.; Kim, Y. M.; Kang, Y. M.; Kim, K. T.; Lee, P. S.; Lee, J. Y. *J. Power Sources* **2001,** *103*(1), 86-92.

27. Park, S. C.; Han, Y. S.; Kang, Y. S.; Lee, P. S.; Ahn, S.; Lee, H. M.; Lee, J. Y. *J. Electrochem. Soc.* **1901,** *148*(7), A680-A686.

28. Sun, Y. K.; Hong, K. J.; Prakash, J.; Amine, K. *Electrochem. Commun.* **2002,** *4*(4), 344-348.

29. Lee, J. H.; Hong, J. K.; Jang D.H.; Sun, Y. K.; Oh, S. M. *J. Power Sources* **2000,** *89,* 7.

30. Nishimura, K.; Douzono, T.; Kasai, M.; Andou, H.; Muranaka, Y.; Kozono, Y. *J. Power Sources* **1999,** *81- 82,* 420.

31. Andersson, A. S.; Thomas, J. O.; Kalska, B.; Haggstrom, L. *Electrochem. & Solid State Letters* **2000,** *3*(2), 66-68.

32. Prosini, P. P.; Carewska, M.; Scaccia, S.; Wisniewski, P.; Pasquali, M. *Electrochim. Acta* **2003,** *48*(28), 4205-4211.

33. Doeff, M. M.; Hu, Y. Q.; McLarnon, F.; Kostecki, R. *Electrochem. & Solid State Letters* **2003,** *6*(10), A207-A209.

34. Fong, R.; Vonsacken, U.; Dahn, J. R. *J. Electrochem. Soc.* **1990,** *137*(7), 2009-2013.

35. Sawai, K.; Iwakoshi, Y.; Ohzuku, T. *Solid State Ionics* **1994,** *69*(3-4), 273-283.

36. Zaghib, K.; Nadeau, G.; Kinoshita, K. *J. Electrochem. Soc.* **2000,** *147*(6), 2110-2115.

37. Zaghib, K.; Kinoshita, K. *J. Power Sources* **2004,** *125,* 214.

38. Ohzuku, T.; Ueda, A.; Yamamoto, N. *J. Electrochem. Soc.* **1995,** *142*(5), 1431-1435.

39. Scharner, S.; Weppner, W.; Schmid-Beurmann, P. *J. Electrochem. Soc.* **1999,** *146*(3), 857-861.

40. Badway, F.; Plitz, I.; Grugeon, S.; Laruelle, S.; Dolle, M.; Gozdz, A. S.; Tarascon, J. M. *Electrochem. & Solid State Letters* **2002,** *5* (6), A115-A118.

41. Scrosati, B.; Croce, F.; Persi, L. *J. Electrochem. Soc.* **2000,** *147*(5), 1718-1721.

42. Xu, K. *Chem.Rev.* **2004,** *104,* 4303.

43. MacFarlane, D. R.; Forsyth, S. A.; Golding, J.; Deacon, G. B. *Green Chemistry* **2002,** *4*(5), 444-448.

44. Bockris, J. O.; Reddy, A. K. N. *Modern Electrochemistry, an Introduction to an Interdisciplinary Area Vol.1 & 2;* Plenum Press, New York: 1970, AN 1970: 526463

45. Winter, M.; Besenhard, J. O.; Spahr, M. E.; Novak, P. *Advanced Mater.* **1998,** *10*(10), 725-763.

46. Saitoh, M.; Yoshida, S.; Yamane, H.; Sano, M.; Fujita, M.; Kifune, K.; Kubota, Y. *J. Power Sources* **2003,** *122*(2), 162-168.

47. Yamane, H.; Saitoh, M.; Sano, M.; Fujita, M.; Sakata, M.; Takada, M.; Nishibori, E.; Tanaka, N. *J. Electrochem. Soc.* **2002,** *149*(12), A1514-A1520.

48. Tarascon, J. M.; Armand, M. *Nature* **2001,** *414*(6861), 359-367.

49. Sickafus, K. E.; Hughes, R. *J. Amer. Ceram. Soc.* **1999,** *82*(12), 3279-3292.

50. Julien, C. M. *Solid State Ionics* **2006,** *177,* 11.

51. Harrison, M. R.; Edwards, P. P.; Goodenough, J. B. *Philosophical Magazine B* **1985,** *52*(3), 679-699.

52. Peramunage, D.; Abraham, K. M. *J. Electrochem. Soc.* **1998,** *145*(8), 2609-2622.

53. Wang, G. X.; Bradhurst, D. H.; Dou, S. X.; Liu, H. K. *J. Power Sources* **1999,** *83*(1-2), 156-161.

54. Zaghib, K.; Simoneau, M.; Armand, M.; Gauthier, M. *J. Power Sources* **1999,** *82*, 300-305.

55. Bach, S.; Pereira-Ramos, J. P.; Baffier, N. *J. Power Sources* **1999,** *82,* 273-276.

56. Bach, S.; Pereira-Ramos, J. P.; Baffier, N. *J. Materials Chemistry* **1998,** *8*(1), 251-253.

57. Kavan, L.; Prochazka, J.; Spitler, T. M.; Kalbac, M.; Zukalova, M. T.; Drezen, T.; Grätzel, M. *J. Electrochem. Soc.* **2003,** *150*(7), A1000-A1007.

58. Colbow, K. M.; Dahn, J. R.; Haering, R. R. *J. Power Sources* **1989,** *26*(3-4), 397-402.

59. Ohzuku, T.; Ueda, A.; Yamamoto, N.; Iwakoshi, Y. *J. Power Sources* **1995,** *54*(1), 99-102.

60. Scharner, S.; Weppner, W.; Schmid-Beurmann, P. *J. Electrochem. Soc.* **1999,** *146*(3), 857-861.

61. Thackeray, M. M. *Progress in Solid State Chemistry* **1997,** *25*(1-2), 1-71.

62. Thackeray, M. M. *J. Amer. Ceramic Soc.* **1999,** *82*(12), 3347-3354.

63. Thackeray, M. M. *J. Electrochem. Soc.* **1995,** *142*(8), 2558.

64. Goodenough, J. B. *Magnetism and the Chemical Bond;* John Wiley and Sons, New York: 1963; Vol. 1. AN 1963: 412206

65. Berg, H.; Goransson, K.; Nolang, B.; Thomas, J. O. *J. Mater. Chem.* **1999,** *9*(11), 2813-2820.

66. Rodriguez-Carvajal, J.; Rousse, G.; Masquelier, C.; Hervieu, M. *Phys. Rev. Letters* **1998,** *81*(21), 4660-4663.

67. Paolone, A.; Roy, P.; Rousse, G.; Masquelier, C.; Rodriguez-Carvajal, J. *Solid State Commun.* **1999,** *111*(8), 453-458.

68. Rousse, G.; Masquelier, C.; Rodriguez-Carvajal, J.; Elkaim, E.; Lauriat, J. P.; Martinez, J. L. *Chemistry of Materials* **1999,** *11*(12), 3629-3635.

69. Rousse, G.; Masquelier, C.; Rodriguez-Carvajal, J.; Hervieu, M. *Electrochem. & Solid State Letters* **1999,** *2*(1), 6-8.

70. Marzec, J.; Swierczek, K.; Przewoznik, J.; Molenda, J.; Simon, D. R.; Kelder, E. M.; Schoonman, J. *Solid State Ionics* **2002,** *146*(3-4), 225-237.

71. Yamada, A.; Tanaka, M. *Mater. Res. Bull.* **1995,** *30*(6), 715-721.

72. Endres, P.; Fuchs, B.; Kemmler-Sack, S.; Brandt, K.; Faust-Becker, G.; Praas, H. W. *Solid State Ionics* **1996,** *89,* 221.

73. Sandler, J.; Shaffer, M. P.; Prasse, T.; Bauhofer, W.; Schulte, K.; Windle, A. H. *Polymer* **1999,** *40*(21), 5967-5971.

74. Masquelier, C.; Tabuchi, M.; Ado, K.; Kanno, R.; Kobayashi, Y.; Maki, Y.; Nakamura, O.; Goodenough, J. B. *J. Solid State Chem.* **1996,** *123*(2), 255-266.

75. Tabuchi, M.; Masquelier, C.; Kobayashi, H.; Kanno, R.; Kobayashi, Y.; Akai, T.; Maki, Y.; Kageyama, H.; Nakamura, O. *J. Power Sources* **1997,** *68*(2), 623-628.

76. Thackeray, M. M. *J. Amer. Ceram. Soc.* **1999,** *82*(12), 3347-3354.

77. Hunter, J. C. *MnO_2 derived from $LiMn_2O_4$, United States Patent* **1982,** *4,312,930*.

78. Hunter, J. C. *J. Solid State Chem.* **1981,** *39,* 142-147.

79. Kelder, E. M.; Ooms, F. J. B.; Perego, R.; Schoonman, J. *J. Power Sources* **2001,** *97-8,* 433-436.

2

The formation of $Li_4Ti_5O_{12}$ using in-situ XRD during precursor decomposition

Abstract

The formation of the $Li_4Ti_5O_{12}$ spinel material as the precursors decompose has been studied via a solid-state and sol-gel methods using in-situ XRD. This technique was used in order to determine the reaction mechanism involved with this material. It was found that an intermediate phase Li_2TiO_3 is the preferred phase to form first at lower temperatures, which reacts with TiO_2 to form the spinel at higher temperatures. Also, the manner to which the precursors decompose dictates the formation of the intermediate phase and affects the reactions at higher temperatures.

2.1 Introduction

As discussed in Chapter 1, $Li_4Ti_5O_{12}$ has been a known anode material for Li-ion batteries (1-5). This material is ideal for the use in Li-ion batteries due to its high capacity retention and low volume change under repeated charge and discharge cycles (2-3). Many groups have used solid-state techniques to form these compounds (4,5). Recently, Peramunage et al. (10) used 32 nm sized TiO_2 with either LiOH or Li_2CO_3 as the precursors for forming the spinel phase when heated up to 800ºC. They have based their precursor material on the following reactions:

$$4LiOH + 5TiO_2 \rightarrow Li_4Ti_5O_{12} + 2H_2O_{(g)} \quad (2.1)$$

$$2Li_2CO_3 + 5TiO_2 \rightarrow Li_4Ti_5O_{12} + 2CO_{2(g)} \quad (2.2)$$

This group has noticed that the reaction to form the spinel with these precursors have yielded two different particle sizes, due to the differences in the way that these precursors decompose. It was observed that the particle size significantly increased when the LiOH precursor was used as opposed to the Li_2CO_3 precursor. It was thought that since the spinel usually forms at 800^{O}C and the decomposition temperature of the Li_2CO_3 (723ºC) was significantly closer to the spinel formation than the decomposition temperature of LiOH (450ºC), the precursors using Li_2CO_3 would directly react to form the spinel. Thus, particle agglomeration of the TiO_2 precursor would be less when using the Li_2CO_3 precursor rather than LiOH. As a result, the overall particle size of the spinel is reduced when using the Li_2CO_3 precursor. It was also observed that the purity of the spinel was better when using this precursor.

Another method to synthesize this spinel is to use a sol-gel technique. Bach et al. have reported a sol-gel technique that produces the $Li_4Ti_5O_{12}$ spinel at a temperature as low as 500ºC (5,11). By using the known sol-gel process of producing TiO_2 through the hydrolysis of Ti-isopropoxide, the spinel structure can be produced using this synthesis technique in conjunction with a hydrated lithium salt. In this report lithium acetate is

dissolved in an alcoholic solvent that forms an intimate mixture of the titanium and lithium oxide gel.

Although some studies have been performed on the determination of the final phases of this material, little information has been found on the formation of this spinel phase using the solid-state technique, while the decomposition of the precursors takes place. Previous studies have used differential thermal analysis (DTA) to determine when the spinel phase occurred. Unfortunately, these attempts have led to unclear interpretations of the analysis, because of the low heat that the material gives off. The low heat signal is comparable to the background signal of the equipment itself (8).

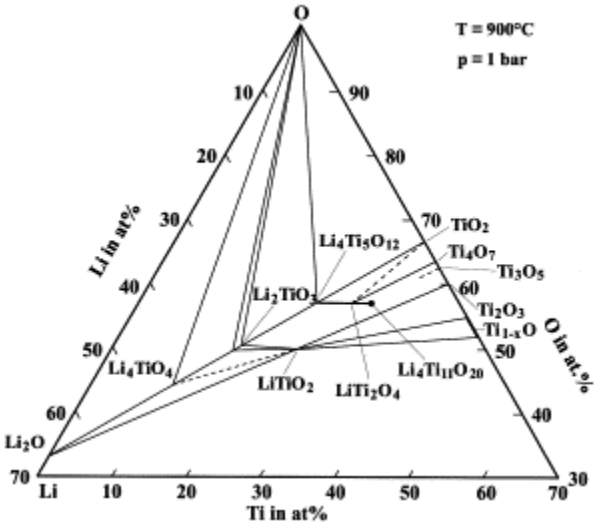

Figure 2-1 Ternary phase diagram of Li-Ti-O from ref. (12)

Kleykamp (12) and others (14,15) have been successful in the construction of a phase diagram along the LiO_2 and TiO_2 phases up to temperatures of 1600ºC. These diagrams are presented in Figures 2-1 and 2-2. It was found that the $Li_4Ti_5O_{12}$ spinel lies in between the TiO_2 and the Li_2TiO_3 phases and is stable up to $1018^{O}C$. It is known that these two phases are typical impurities that are found after the initial annealing of the precursors to form the spinel. Subsequent mixing and annealing steps reduce the amount of these impurities (10). This chapter explores the formation of $Li_4Ti_5O_{12}$, using solid-state and sol-gel techniques that are analyzed in-situ through the use of high-temperature

XRD. For the case of the solid-state synthesis, Li_2CO_3 and LiOH precursors are mixed with anatase and rutile TiO_2 particles and the sol-gel synthesis uses precursors as described by Bach (5, 11). In addition, DTA and Thermal Gravimetric Analysis (TGA) analyses are presented.

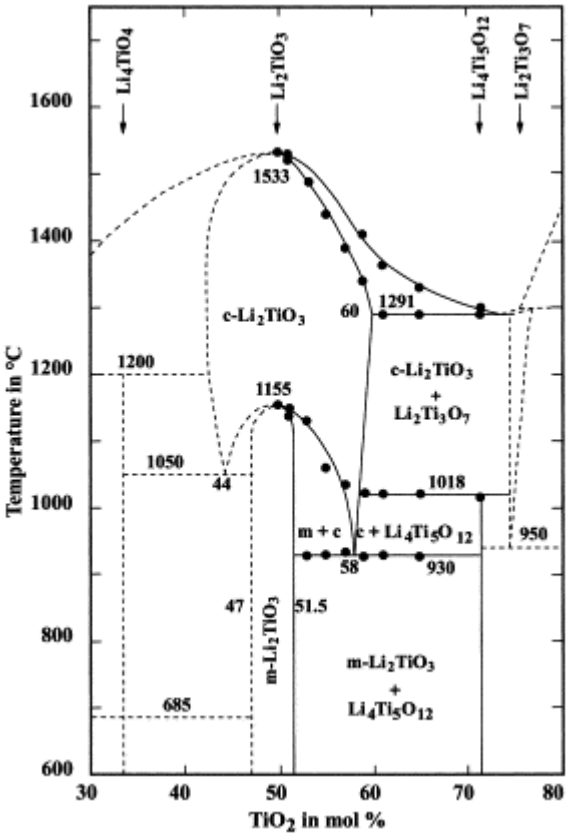

Figure 2-2 Partial binary phase diagram of Li_2O and TiO_2 from ref.(12)

2.2 Experimental

2.2.1 Precursors

Table 1 presents a summary of the precursors for the preparation of the experiments. In the solid-state case, stoichiometric amounts of lithium hydroxide (Aldrich), or lithium carbonate (Aldrich) were either dissolved in distilled water or dry mixed via mortar and

pestle with nano-sized anatase TiO_2 (Degussa P25), or micron-sized rutile TiO_2 (Aldrich). In the case where a solution was used, the mixture was stirred for approximately 8 hours and dried at 110ºC in air. The precipitates were then collected. The sol-gel technique used stoichiometric mixtures of titanium isopropoxide (Aldrich) with lithium acetate (Aldrich) dissolved in high purity ethanol. This mixture was stirred for 2 hours and then dried in air at $110^{O}C$. Afterwards, the precipitates were collected.

Table 2-1 *The lithium and titanium precursors and the preparation methods.*

Sample	Titanium	Lithium	Preparation
A-1	Anatase TiO_2	LiOH	Water solvent
A-2	Anatase TiO_2	Li_2CO_3	Dry mixed
R-1	Rutile TiO_2	LiOH	Water solvent
R-2	Rutile TiO_2	Li_2CO_3	Dry mixed
S-G	Ti-isopropoxide	Li-acetate	Ethanol solvent

2.2.2 Thermal Gravimetric Analysis and Differential Thermal Analysis

Thermal Gravimetric Analysis (TGA) and Differential Thermal Analysis (DTA) were performed using a Setaram type Setesys 16 apparatus with platinum crucibles. The amount of material that was used was between 5 and 6 mg for each experiment. The temperature scan was from $25^{O}C$ up to $1000^{O}C$ at a $3^{O}C$/min rate in air.

2.2.3 In-situ X-ray diffraction

The in-situ X-ray diffraction measurements were performed on a Bruker-AXS D5005 Theta/Theta type diffractometer with a diffracted beam graphite monochromator using CuKα radiation. This type of diffractometer was used, because it allowed a full spectrum to be observed without rotating the sample. The other advantage in using this technique is that the XRD pattern is not distorted when the data are collected.

A schematic view of the X-ray diffraction unit is presented in Figure 2-3. A wide range high-temperature chamber housed the system in which flowing air was used. A Pt-Rh strip was used for direct heating of the sample. The sample was mounted onto the strip by taking the precipitates of the precursors and mixing it with ethanol. The mixture was gently ground into a slurry, that was then applied onto the strip. The average amount on the strip was approximately 10mg and the dimensions of the samples were 10mm wide

by 15mm long. The strip was placed directly onto the heating element and a spring kept the tension on the strip to avoid the displacement of the sample during heating. A thermocouple was placed below the strip to record the temperature.

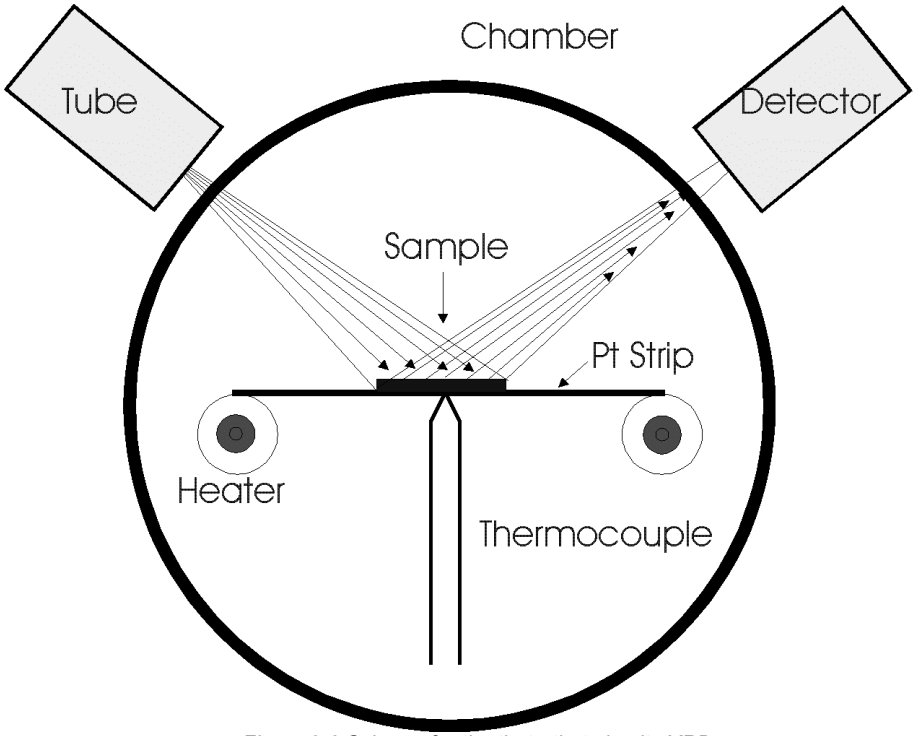

Figure 2-3 Scheme for the theta-theta in-situ XRD

Each measurement was performed at 25ºC intervals and was controlled to within 1ºC from room temperature to 700ºC under a flowing air environment. The time it took for each measurement was approximately 9 minutes. The range of the spectrum was between the 2-Θ angles of 15-45º.

To understand the mechanism of these reactions, part of the XRD pattern was separated using Gaussian profiles via a computer program Peak Fit (Jandal). Although this fitting is not quantitative, it is qualitative in terms of the separation of the peaks for phase identification. The 2-Θ angles that the separation was performed, was in the range of 34-39.5º. This range was chosen because the peaks in this region corresponds to the ex-

pected phases that can be observed without severe overlap. The fitting was used on scans at 50ºC intervals beginning at 450ºC. If the pattern changed, scans between the 25ºC intervals were analysed as well.

2.3 Results

2.3.1 Thermal Gravimetric Analysis and Differential Thermal Analysis

The TGA traces for all the precursors are given in Figure 2-4. Traces A and B are the solid-state precursors using the LiOH with anatase and rutile TiO_2, respectively. These traces release the least weight which is approximately 6%. This loss is expected due to the release of water from the precursors. Traces C and D are the solid-state precursors using Li_2CO_3 with anatase and rutile TiO_2 , respectively. The weight loss for these samples is between 17 and 20%. This significant weight loss is due to the decomposition of the carbonates in the system. For all of the solid-state reactions, the system stops losing weight around 700ºC. After this temperature, a stable trace is observed. It is reasoned that at this point both precursor salts decomposed and that only solid products are present. It is also observed that the greatest decrease in weight takes place in the temperature range of 400-700ºC. The TGA trace for curve E involves the sol-gel precursor. This system has the greatest weight loss at approximately 40% due to the high content of organics in this system. Unlike the solid-state reactions, most of its weight loss occurs before 375ºC. This is followed by a relatively stable signal up to 1000ºC. The majority of its weight loss occurs between the temperatures of 225-375ºC.

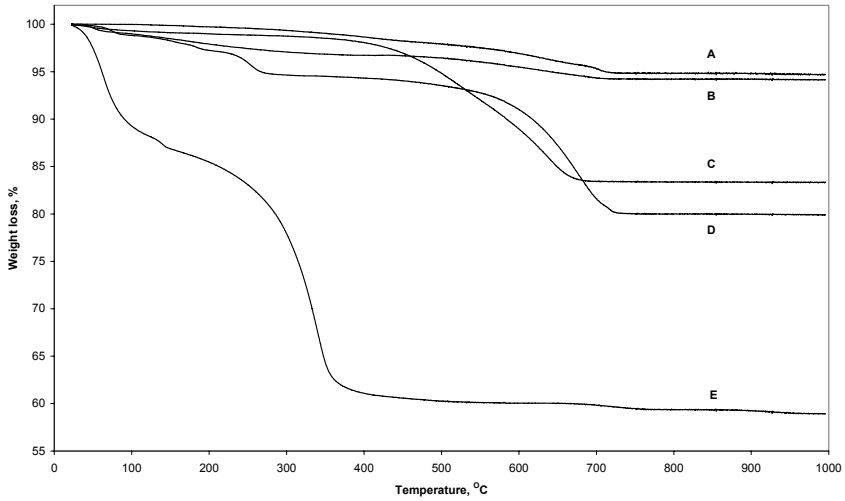

Figure 2-4 TGA traces for LiOH salt with: A-rutile TiO_2 , B-anatase TiO_2 , and Li_2CO_3 salt with: C-anatase TiO_2 , D-rutile TiO_2 , E-sol-gel

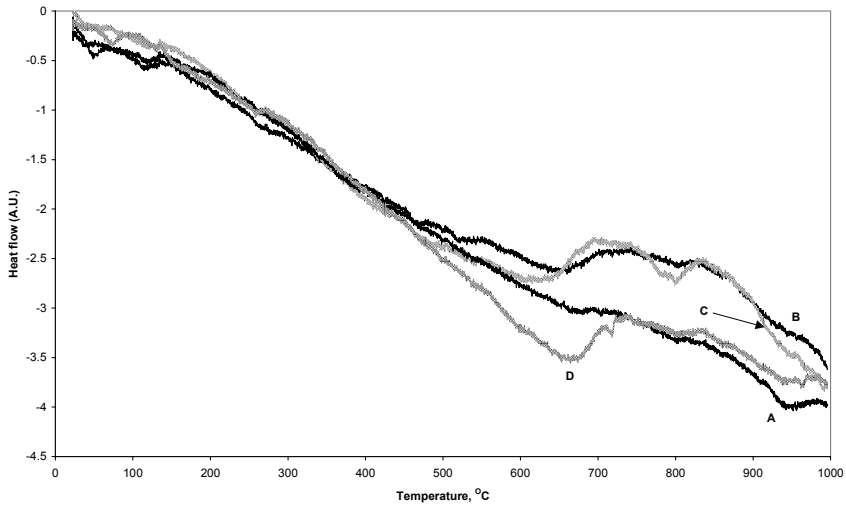

Figure 2-5 DTA traces for LiOH salt with: A-rutile TiO_2 , B-anatase TiO_2 , and Li_2CO_3 salt with: C-anatase TiO_2 , D-rutile TiO_2

Figure 2-5 presents the DTA traces for the solid-state precursors. The traces for all of the solid-state precursors are stable until 700ºC, where one or perhaps two exothermic peaks occur beyond that temperature. This may indicate that only the decomposition of salt precursors is active until 700^{O}C. For the sol-gel precursors presented in Figure 2-6 at approximately 350ºC, a strong exothermic peak is observed. This coincides with the weight loss of the TGA trace and is interpreted as the loss of organics from both lithium and titanium precursors.

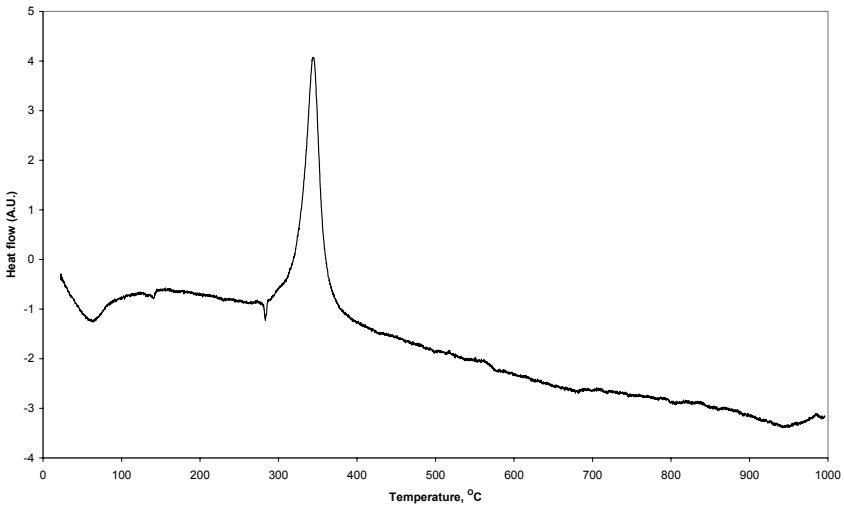

Figure 2-6 DTA trace of the sol-gel precursors

2.3.2 In-situ X-Ray diffractograms

Figures 2-7 and 2-8 present a series of patterns between 2-Θ angles of 15-45º relating to the mixture of anatase and rutile TiO_2 with the LiOH from room temperature to 700ºC, respectively. From both figures, only TiO_2 can be observed at room temperature. It is also observed that minor amounts of impure TiO_2 are found from the initial precursor that was designated for the study, i.e., both forms of TiO_2 were found at room temperature in all solid- state precursors.

In Figure 2-7, where anatase TiO_2 is mixed with LiOH, the emergence of a peak is observed approximately at a 2-Θ angle of 18.5º at 425ºC. The identity of this peak could be either the spinel or the cubic Li_2TiO_3 phase or both since the peaks of both peaks overlap each other. This is followed by an increase of the rutile phase and a decrease of the anatase phase. At a temperature of 575ºC, a clear spinel peak appears around a 2-Θ angle of 34.2º. Finally, the last spectrum at a temperature of 700ºC reveals both forms of TiO_2, Li_2TiO_3, and the spinel phase $Li_4Ti_5O_{12}$.

Figure 2-8 presents the same series, but with the rutile TiO_2 and LiOH precursors. Although the initial precursors possess both forms of TiO_2, the majority phase from this precursor is the rutile form. By comparing the diffractograms of Figures 2-7 and 2-8, similar observations are found as in the anatase TiO_2 case, but the changes occur at elevated temperatures. For example, the peak that was found at the 18.5º angle begins at a temperature of 550ºC in the rutile case rather than at 425ºC shown in the anatase case. Furthermore, there is not a distinct spinel peak even at a temperature of 700ºC at the 34.2º angle. The particle size difference between the two forms probably accounts for this discrepancy. The rutile TiO_2 is ~10 microns, while the particle size for the anatase is 25 nano-meters, but from the DTA analysis shown earlier, both materials seem to react in the same manner.

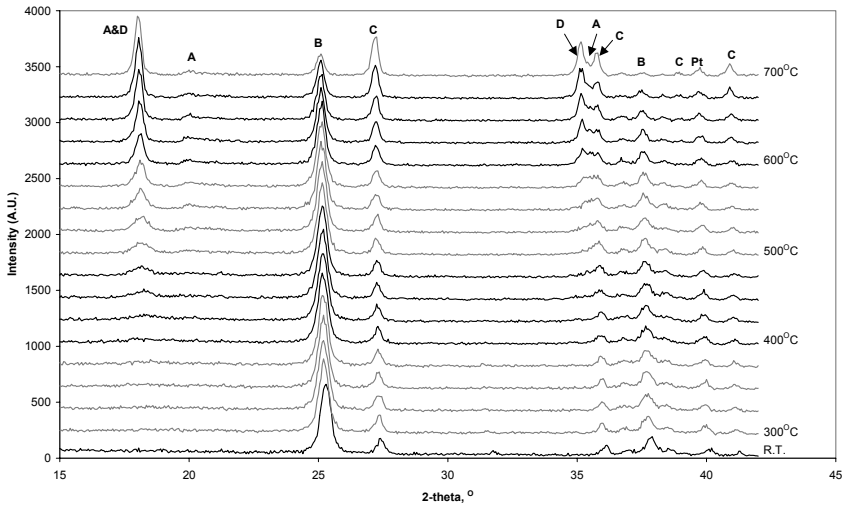

Figure 2-7 XRD patterns of anatase TiO_2 with LiOH salt as a function of temperature: A–Li_2TiO_3, B-anatase TiO_2, C-rutile TiO_2, D-$Li_4Ti_5O_{12}$

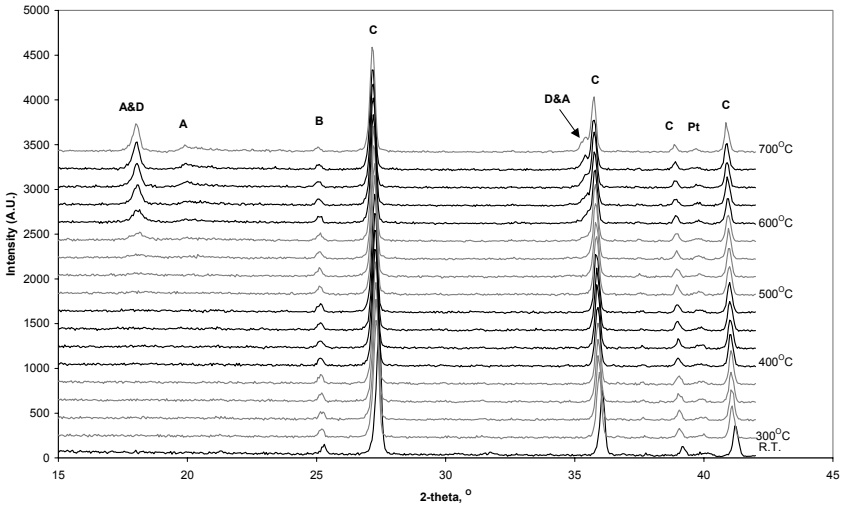

Figure 2-8 XRD patterns of rutile TiO_2 with LiOH salt as a function of temperature: A-Li_2TiO_3, B-anatase TiO_2, C-rutile TiO_2, D -$Li_4Ti_5O_{12}$

Figures 2-9 and 2-10 present a similar series that contain anatase and rutile TiO_2 with Li_2CO_3 precursors, respectively. Although similar observations can be seen in regard to the phase formations that are observed in the LiOH system, the temperature at which the phases occur is notably higher. For example, Figure 2-6 presents the case where the anatase TiO_2 is mixed with Li_2CO_3 precursors, the formation of the first material to appear is a peak at a 2-Θ angle of 18.5º that begins to appear at a temperature of 500ºC. However, the same peak appears at a temperature of 425ºC in the case where the LiOH precursor is used. The difference is due to the decomposition of the Li_2CO_3 precursor at higher temperatures. This can be seen in Figure 2-8, where Li_2CO_3 is present up to a temperature of 600ºC and in Figure 2-9, where the presence of the this precursor is observed up to a temperature of 650ºC.

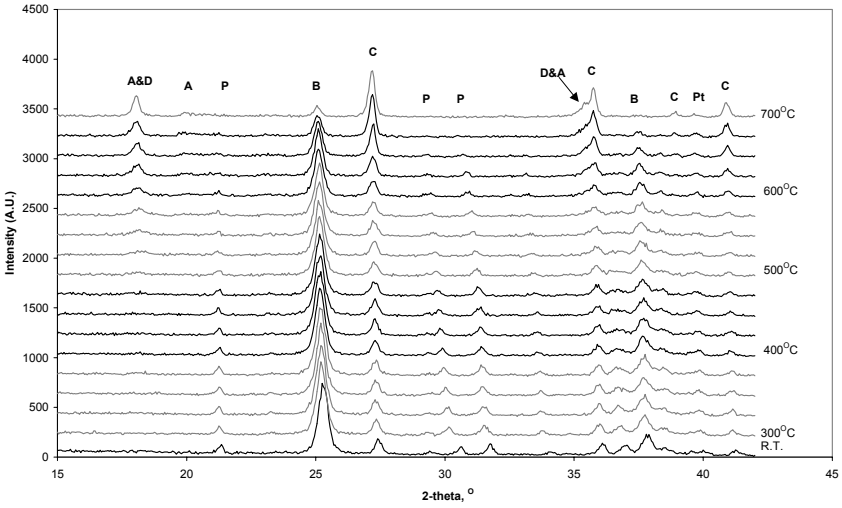

Figure 2-9 XRD pattern of anatase TiO_2 with Li_2CO_3 as a function of temperature: A-Li_2TiO_3, B-anatase TiO_2, C-rutile TiO_2, D-$Li_4Ti_5O_{12}$, P-Li_2CO_3

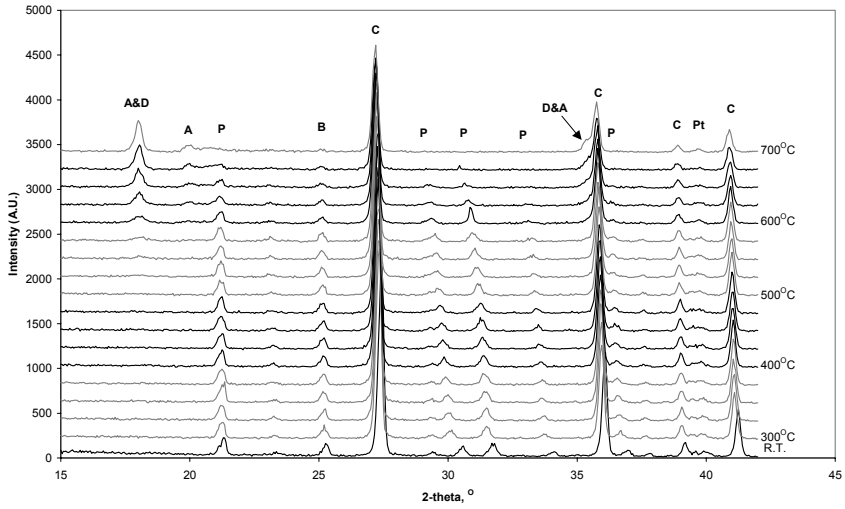

Figure 2-10 XRD pattern of rutile TiO_2 with Li_2CO_3 as a function of temperature: A-Li_2TiO_3, B-anatase TiO_2, C-rutile TiO_2, D-$Li_4Ti_5O_{12}$, P-Li_2CO_3

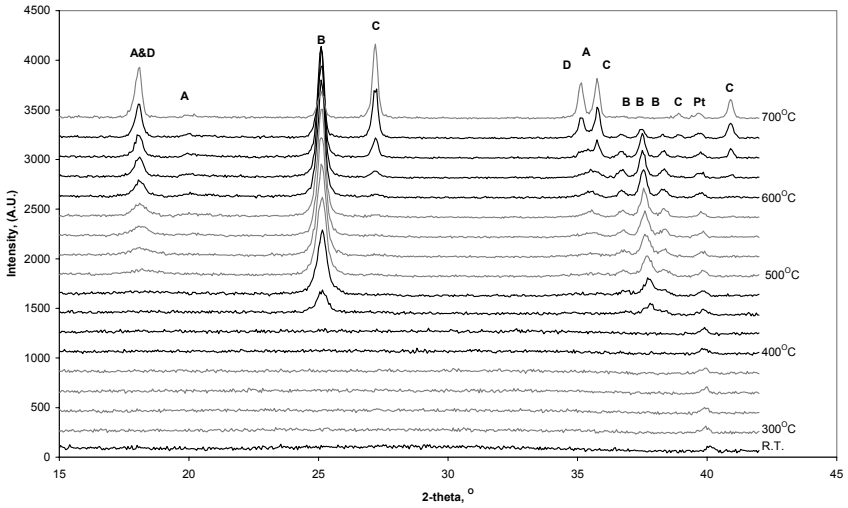

Figure 2-11 XRD pattern of the sol-gel precursor as a function of temperature: A-Li_2TiO_3, B-anatase TiO_2, C-rutile TiO_2, D-$Li_4Ti_5O_{12}$

Figure 2-11 presents the XRD spectrum of the materials formed using the sol-gel technique. This method may represent an ideal mixing of Li, Ti, and O. As expected at room temperature, this mixture is amorphous. The peak at a 2-θ angle of 40º is the Pt-Rh support strip. At a temperature of 475ºC the formation of anatase TiO_2 is observed. The formation of the Li_2TiO_3 phase is observed at a higher temperature of 500ºC. Finally, the rutile TiO_2 forms at a temperature of 600ºC. The spinel peak is first observed at the 2-θ angle of 35º at 625ºC and becomes more distinct at 675ºC.

2.3.3 Separation of peaks from diffractograms

In order to distinguish phases that were observed in the previous section, it is possible to separate the peaks of these spectra in a particular region of interest where the observed phases can be more distinguishable. The separation of peaks of the XRD spectrum is between the 2-θ angles of 34^O-39.4^O. The spectrum using both forms of TiO_2 mixed with LiOH as precursors is presented in Figures 2-12 and 2-13. The separation of peaks for the anatase TiO_2 shown in Figure 2-12 reflects the formation of Li_2TiO_3 at a temperature of 475ºC. At a temperature of 575ºC, a spinel peak is formed and between the temperature range of 600-700ºC the spinel and rutile TiO_2 peaks increase, while the anatase peaks decrease. Figure 2-13 shows the peak separation for the rutile TiO_2 and LiOH precursors. As observed with the anatase TiO_2, the Li_2TiO_3 is first formed at a temperature of 550ºC and is followed by the spinel at a temperature of 700ºC.

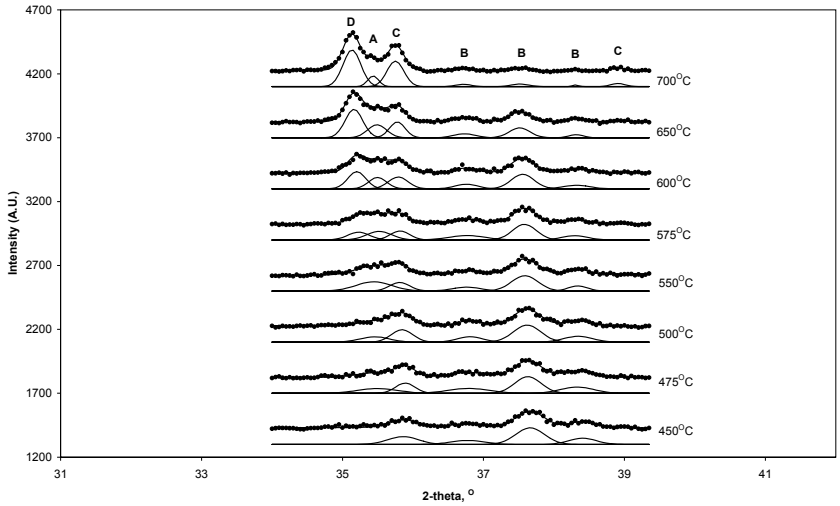

Figure 2-12 The separation of the XRD pattern in the 2-θ range 34-39.4º as a function of temperature for the anatase TiO_2 with the LiOH precursor; A-Li_2TiO_3, B-anatase TiO_2, C-rutile TiO_2, D-$Li_4Ti_5O_{12}$

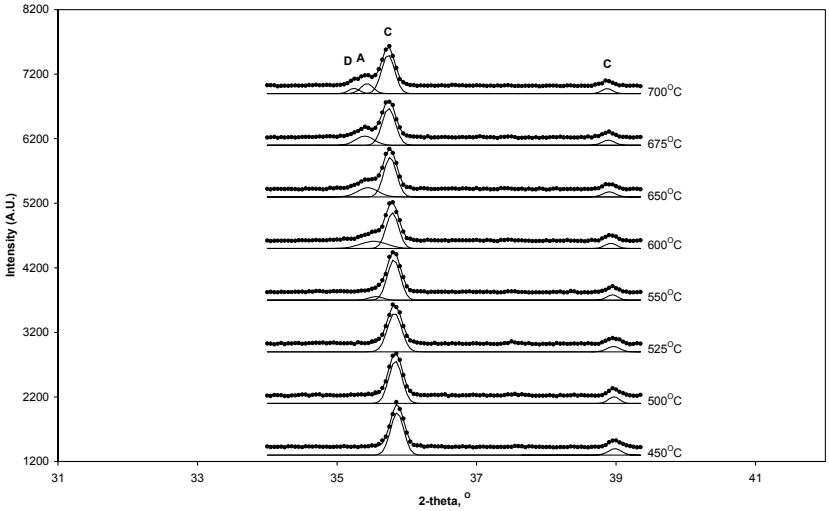

Figure 2-13 The separation of the XRD pattern in the 2-θ range 34-39.4º as a function of temperature for the rutile TiO_2 with the LiOH precursor: A-Li_2TiO_3, B-anatase TiO_2, C-rutile TiO_2, D-$Li_4Ti_5O_{12}$, P-Li_2CO_3

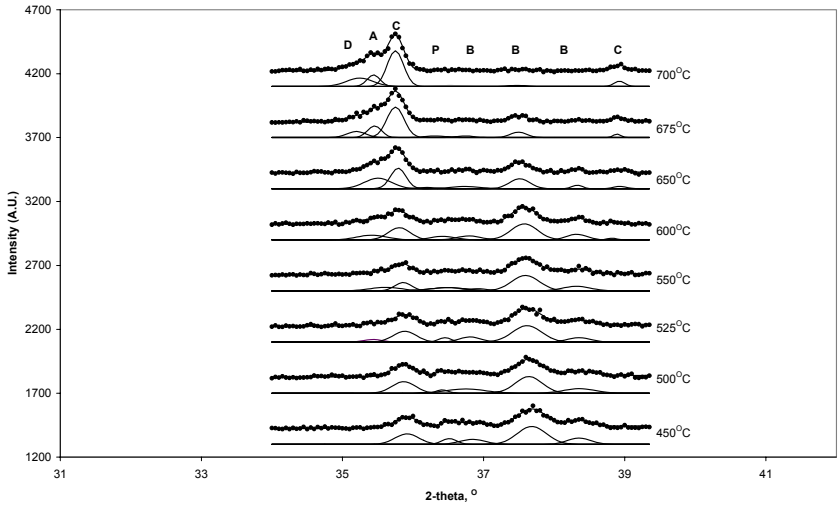

Figure 2-14 The separation of the XRD pattern in the 2-θ range 34-39.4º as a function of temperature for anatase TiO_2 with Li_2CO_3 precursor: A-Li_2TiO_3, B-anatase TiO_2, C-rutile TiO_2, D-$Li_4Ti_5O_{12}$, P-Li_2CO_3

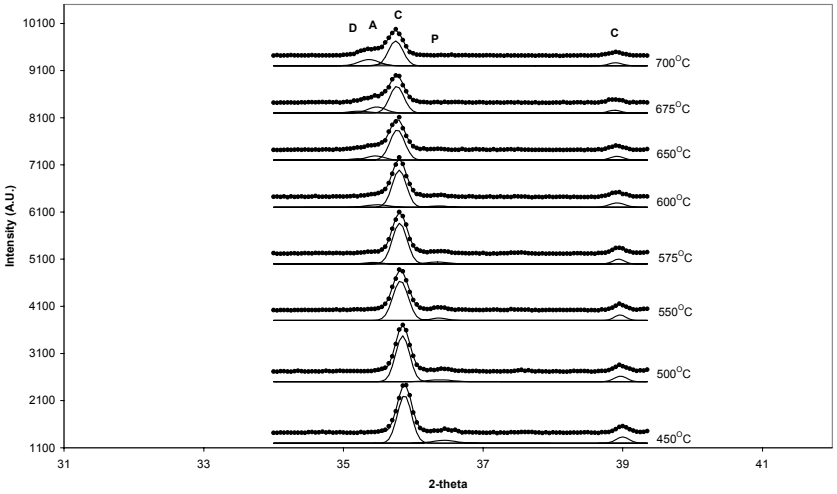

Figure 2-15 The separation of the XRD pattern in the 2-θ range 34-39.4º as a function of temperature for rutile TiO_2 with Li_2CO_3 precursor: A-Li_2TiO_3, B-anatase TiO_2, C-rutile TiO_2, D-$Li_4Ti_5O_{12}$, P-Li_2CO_3

The peak separation for the XRD spectra of the precursors containing the Li_2CO_3 with anatase and rutile TiO_2 is presented in Figures 2-14 and 2-15, respectively. Figure 2-14 reveals initially the presence of anatase and minor amounts of rutile TiO_2 throughout the entire temperature range. The presence of the Li_2CO_3 precursor is observed up to a temperature of 675ºC. At 525ºC, the Li_2TiO_3 phase appears and continues to grow, while the anatase decreases. At a temperature of 675ºC, the spinel peak is formed along with the presence of Li_2TiO_3 and both forms of TiO_2 and Li_2CO_3. Finally, at a temperature of 700°C, the anatase TiO_2 peaks practically disappear. Figure 2-15 presents the separation of peaks of the Li_2CO_3 and rutile precursors. This figure reveals only the rutile phase to be present throughout the entire temperature range in the presence of the Li_2CO_3 precursor up to a temperature of 600°C. The formation of the Li_2TiO_3 phase begins at a temperature of 600°C and finally the spinel begins to form at 675°C.

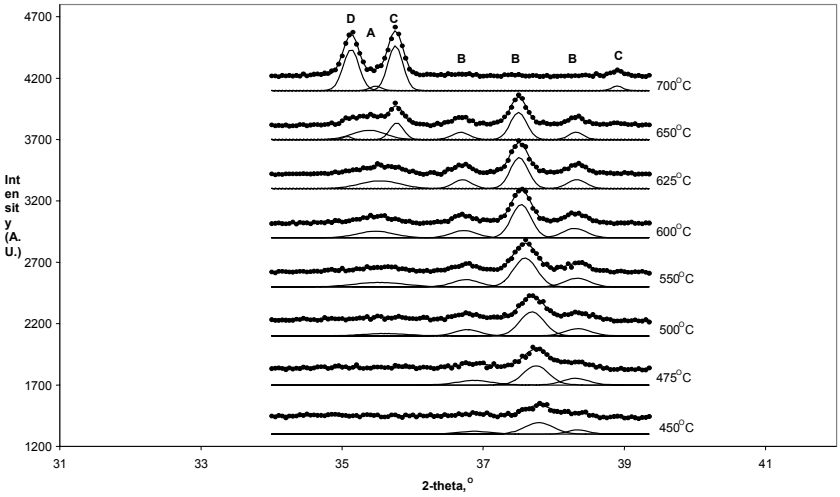

Figure 2-16 The separation of the XRD pattern in the 2-Θ range 34-39.4º as a function of temperature for the materials obtained using the sol-gel method: A-Li_2TiO_3, B-anatase TiO_2, C-rutile TiO_2, D-$Li_4Ti_5O_{12}$

Figure 2-16 presents the separation of the partial scan obtained from material using the sol-gel technique. Initial room temperature scan presents an amorphous pattern that is not shown in this figure. At 450°C though, anatase TiO_2 is first observed. The Li_2TiO_3 phase begins to appear at 500ºC that continues to increase and at 650ºC the rutile and

the spinel peak appear. Finally, at 700ºC the anatase peaks completely disappear, while the rutile, Li_2TiO_3, and spinel peaks remain. The spinel and rutile peaks grow in intensity while the Li_2TiO_3 peak decreases during that period. It is then clear from this analysis that the preferred structure to form first is the anatase TiO_2 followed by the Li_2TiO_3 phase. The next phase is the rutile TiO_2 and finally the $Li_4Ti_5O_{12}$ spinel phase is formed.

2.4 Discussion

From the DTA results in the solid-state method, the bulk energy is released beyond $700^{O}C$ but the TGA results show that the decomposition of the two lithium salts occurs below this temperature. In addition, the manner that the precursors of LiOH and Li_2CO_3 decompose is also different. In the case of LiOH, a gradual slope of the TGA trace is observed, while for the case of Li_2CO_3 a sharp loss of weight is seen. Since in-situ XRD measurements for these precursors show the formation of Li_2TiO_3 during the decomposition of these salts, the manner that these precursor salts decompose has a direct effect on the formation of the impurity Li_2TiO_3 phase. By comparing Figures 2-12 and 2-14 or Figures 2-13 and 2-15, it is clear that Li_2TiO_3 develops further in the case of the LiOH precursor than in the case where the Li_2CO_3 precursor is used. Finally, the formation of these structures form during the precursor decomposition (T<700°C) presents no obvious thermal results from DTA. This implies that either these reactions are too subtle for thermal analysis or that the decomposition of the precursors overshadows any other reaction occurring in the system.

The sol-gel precursors present a slightly different picture in the formation of the spinel as is observed. First, the DTA results show a sharp exothermic peak at a much lower temperature (~400°C) and the TGA results presents a sharp decline of weight loss at the same temperature followed by a gradual decline. The in-situ XRD measurements show the formation of the anatase TiO_2 that co-insides approximately with the same temperature as the exothermic peak but, continues to form the other phases at higher temperatures. Interestingly enough, the Li_2TiO_3 phase begins to form before the transformation of anatase to rutile TiO_2. Once again as in the case of the solid-state method, the formation of these other structures is not obvious in the thermal measurements.

In general, from the analyses of the in-situ XRD measurements, the preferred phases at lower temperatures as the precursors decompose would be anatase TiO_2 and Li_2TiO_3. At elevated temperatures, the rutile TiO_2 and the $Li_4Ti_5O_{12}$ spinel phases form, while the amount of the lower temperature phases decrease. This would imply that the Li_2TiO_3 phase is being consumed, while the spinel is forming and thus is considered an intermediate phase.

Since there is always multiple phases present at any given temperature while trying to form a single spinel phase, the reactions are not in equilibrium and the kinetics for these reactions are rather slow. However, it has been shown, given enough heating time, the spinel can form as low as $500^{O}C$ using the sol-gel method as shown by other groups (5,13). Nevertheless, the basic finding of this study is that $Li_4Ti_5O_{12}$ spinel formation from either solid-state or sol-gel precursors involves an intermediate phase in the region where the precursors decompose from room to the elevated temperatures.

A proposed reaction mechanism for the spinel formation during the precursor decomposition region is presented in Equations 2.3 and 2.4. The reactions of the solid-state precursors give the following reaction schemes:

$$TiO_2 + 2LiOH \rightarrow Li_2TiO_{3(s)} + H_2O_{(g)} \qquad (2.3)$$

$$TiO_2 + Li_2CO_3 \rightarrow Li_2TiO_{3(s)} + CO_{2(g)} \qquad (2.4)$$

The intermediate phase from the above equations then continues to react with the TiO_2 precursor to form the spinel as shown in the next reaction:

$$2Li_2TiO_3 + 3TiO_2 \rightarrow Li_4Ti_5O_{12} \qquad (2.5)$$

In the case where the sol-gel precursor is used, the following reactions occur:

$$Li - Ti - O_{(gel)} \rightarrow TiO_2 + Li_2TiO_3 \qquad (2.6)$$

$$2Li_2TiO_3 + 3TiO_2 \rightarrow Li_4Ti_5O_{12} \qquad (2.7)$$

With regard to the particle size difference to the salt precursor used that Peramunage and Abraham reported, agglomeration of the products by using the LiOH precursor may indeed cause the increase of particle size as the agglomerates are heated to elevated temperatures (10). Additionally, the manner that the precursors decompose also affects the purity of the spinel as discussed earlier.

A balance between purity and processing temperature is observed here. The formation of the low-temperature phase, Li_2TiO_3, could be suppressed by using the higher decomposing Li_2CO_3 precursor, but then the formation of the spinel must be processed either at a higher temperature or a two-step annealing scheme (16). On the other hand, a low-melting precursor will produce more of the intermediate phase and the spinel can be processed at a lower temperature. However, the kinetics are slower and either annealing at higher temperatures or, longer annealing times are needed in order to yield a phase pure spinel. In addition, the sintering effect of the particles increases. In this regard, the sol-gel precursors seem to possess this balance of a fast decomposing precursor that forms the intermediate phase early and then to form the spinel at much lower temperatures.

2.5 Conclusions

The formation of the $Li_4Ti_5O_{12}$ spinel has been successfully studied using in-situ XRD for both solid-state and sol-gel techniques. It was found that the formation of the spinel is a sluggish reaction, as the precursors decompose and that an intermediate phase was involved. As the precursor decomposes, the Li_2TiO_3 intermediate phase forms first at lower temperatures. This phase then further reacts with TiO_2 to form the $Li_4Ti_5O_{12}$ spinel at higher temperatures.

In the case of the solid-state synthesis method, the LiOH precursor forms the intermediate phases at a lower temperature when compared to the Li_2CO_3 precursor due to its lower melting temperature and the manner that the decomposition takes place. Due to the sharp decomposition at higher temperature, the Li_2CO_3 precursor suppresses the in-

termediate phase which also suppresses the spinel to form at lower temperatures. In the case where the sol-gel precursors are used, the phases that are formed sequentially appear to be: anatase TiO_2 followed by Li_2TiO_3, and next rutile TiO_2 followed by the $Li_4Ti_5O_{12}$ spinel.

2.6 References

1. Colbow, K. M.; Dahn, J. R.; Haering, R. R. *J.Power Sources* **1989**, *26*, 397-402.

2. Panero, S.; Satolli, D.; Salomon, M.; Scrosati, B. *Electrochem.Comm.* **2000**, *2*, 810-813.

3. Prosini, P. P.; Mancini, R.; Petrucci, L.; Contini, V.; Villano, P. *Solid State Ionics* **2001**, *144*, 185-192.

4. Wang, G. X.; Bradhurst, D. H.; Dou, S. X.; Liu, H. K. *J.Power Sources* **1999**, *83*, 156-161.

5. Bach, S.; Pereira-Ramos, J. P.; Baffier, N. *J.Mater.Chem.* **1998**, *8*, 251-253.

6. Ferg, E.; Gummow, R. J.; Dekock, A.; Thackeray, M. M. *J.Electrochem.Soc.* **1994**, *141*, L147-L150.

7. Ohzuku, T.; Ueda, A.; Yamamoto, N. *J.Electrochem.Soc.* **1995**, *142*, 1431-1435.

8. Zaghib, K.; Simoneau, M.; Armand, M.; Gauthier, M. *J.Power Sources* **1999**, *82*, 300-305.

9. Huang, H.; Kelder, E.; Simon, D. R.; Schoonman, J. *Meeting Abstract - 198th Meeting of The Electrochemical Society* **2000**, *2000-2*.

10. Peramunage, D.; Abraham, K. M. *J.Electrochem.Soc.* **1998**, *145*, 2609-2622.

11. Bach, S.; Pereira-Ramos, J. P.; Baffier, N. *J.Power Sources* **1999**, *82*, 273-276.

12. Kleykamp, H. *Fusion Engineering Design* **2002**, *61-62*, 361-366.

13. Kavan, L.; Prochazka, J.; Spitler, T. M.; Kalbac, M.; Zukalova, M. T.; Drezen, T.; Grätzel, M. *J.Electrochem.Soc.* **2003**, *150*, A1000-A1007.

14. Izquierdo, G.; West, A.R. Mater. Res. Bull. 15 **1980**, 15, 1655

15. Mikkelsen, J.C. J.Amer. Cer. Soc. **1980**, 63, 331

16. Simon, D. R.; Huang, H.; Kelder, E.; Schoonman, J. *Meeting Abstract - 198th Meeting of The Electrochemical Society* **2000**, *2000-2*.

3

Proton exchange in $Li_4Ti_5O_{12}$ and its electrochemical properties

Abstract

The stability of $Li_4Ti_5O_{12}$ spinel material in acidic solutions has been examined. This study determined that a proton exchange with Li^+ ions from $Li_4Ti_5O_{12}$ spinel material occurs in solution. The spinel structure is retained up to 69 % exchanged ions that is associated with a 0.25% reduction of volume from the initial spinel. The protons reside on the 8a and 48f sites, that form alternating planes with 16d Li and Ti sites in the spinel structure. Electrochemical results of the ion-exchange material show a general decrease of capacity as more protons are present in the structure. These curves also show that the 1.55V plateau becomes less distinguishable as more protons are present in the structure. Additional electrochemical studies have shown that the pure material may react with water from the atmosphere under storage. The performance of the reacted material shows a slight loss of capacity and enhances polarization between cell charge and discharge.

3.1 Introduction

It is well known that the formation of acids occurs in non-aqueous electrolytes that are used for Li-ion battery systems (1-3). Previous studies have reported that most Li-containing electrode materials are not stable, when they are in contact with acidic solutions (4-6). In the case of the $LiMn_2O_4$ spinel material, Li^+ ions are topotatically extracted out of these spinels. A disproportion of the Mn^{3+} cations is the driving force for this reaction. The Mn^{3+} cations in this material reduce to Mn^{2+} and oxidize to Mn^{4+} to form a λ-MnO_2 spinel as described by Hunter (7). Feng et al. (6) described these reactions further and proposed an ion exchange mechanism at a critical value of Li/Mn ratio. Although Li^+ ions may also be chemically inserted back into λ-MnO_2, when it is submersed in an aqueous LiOH solution, the electrochemical performance of these materials were reported to be poor (8).

Other studies were focused on materials that exhibit only ion exchange between protons and Li^+ ions. One example is the $Li_4Mn_5O_{12}$ spinel material (9,10). These reports show that this material can exchange protons for Li^+ ions when in contact in acidic solutions. The conversion of the ion exchange was reported to be 90%. Furthermore, the exchange between Li^+ ions and protons is reversible when the proton-exchanged material is in contact with LiOH aqueous solution.

One group has reported ion exchange between Li^+ ions and protons for materials based on the partial substitution of Mn in the $Li_4Mn_5O_{12}$ spinel with Cr, Co or Ti cations (11). Some results, such as exchange properties for these materials, have been reported. However, other details such as structure and electrochemical performance were not reported.

Another material that is of interest as an anode material for Li ion battery applications is the $Li_4Ti_5O_{12}$ spinel material. In this spinel, Li that generally resides in the 8a tetrahedral sites replaces 1/6 of the Ti 16d sites. Therefore, the spinel notation for this structure is $Li_1[Li_{0.33}Ti_{1.67}]O_4$ where the elements in the brackets represent the octahedral sites of the spinel. This material exhibits practically zero volume change as Li is inserted into the material and a flat potential curve is observed for over 90% of its capacity (12,13). Although the stability of this material in regards to electrochemical cycling is well documented, to date no reports have shown the stability of this material if in contact with

acidic solutions and the subsequent electrochemical performance. The current work is focused on the stability of $Li_4Ti_5O_{12}$ spinel material in aqueous acidic solutions and its electrochemical performance.

3.2 Experimental

3.2.1 Material preparation

Commercially available $Li_4Ti_5O_{12}$ (Hohsen) with an average particle size of approximately 30 microns was used as the basis for these experiments. Subsequent processing included ball milling this material for 2 and 6 hours using a planetary ball mill. An agate crucible and lid along with grinding balls were used. Hexane (Baker) was used as a lubricant, that was filled approximately to 1/3 of the crucible by volume.

3.2.2 Chemical titration of $Li_4Ti_5O_{12}$

Titration of the $Li_4Ti_5O_{12}$ samples was performed using a Metrohm titrator. A combination glass electrode coupled with a Ag-AgCl reference electrode was employed to monitor the pH of the solution. The combination electrode was calibrated to known buffer solutions. Samples of approximately one gram of $Li_4Ti_5O_{12}$ were placed in 50 ml of deionized water (Milli-Q). Small amounts of 1M HCl acid (Baker) were periodically injected into the solution at 10-minute intervals. Each injection contained 30 microliters of acid and the titration finished when the total volume of acid that was added to the solution reached to 10 ml. The pH of the solution was measured after each injection. Afterwards, the solution was separated from the solids. The solids were washed with deionized water and dried at $120^{O}C$ overnight in air.

3.2.3 Structural characterization

Structural characterization was performed using a Bruker X-ray diffractometer (XRD) that used a copper electrode. Typical scans ranged at 2-Θ angles from $0\text{-}90^{O}$ and were identified using the provided software. These scans were performed at room temperature in air.

Sample preparation for the neutron diffraction experiments used 1 gram of 6-hours ball-milled particles, that was submersed in 50 ml of deionized water. Approximately 6

ml of 1M HCl acid (Baker) was added to the solution, that was heated to $50^{O}C$ for 10 days. Constant stirring of the solution during that time period insured a homogeneous mixing of the solution with the $Li_4Ti_5O_{12}$ particles. The same procedure was followed in the collection, washing, and drying of the solids as previously described.

Neutron diffraction was performed using a general materials diffractometer (GEM), the high-general purpose time-of-flight diffractometer at the ISIS pulsed neutron source at the Rutherford Appleton Laboratory in England (14). For the present sample, significant intensity was found in the d-spacing range of 0.2-0.8Å. Cylindrical vanadium sample cans were used for all measurements. The data were corrected for the scattering of vanadium with the Ariel software and Rietveld refinement was performed using the software program GSAS.

3.2.4 Chemical, spectroscopy, and thermal analysis

Chemical analysis of the solution after titration was performed using a Perkin Elmer Optima 4300DV atomic adsorption analysis (AAS) unit. This unit was calibrated against known quantities of Li^{+} and Ti^{4+} ions. Approximately 20 ml of solution for each sample was saved for this measurement.

Fourier-Transform Infrared (FTIR) measurements were performed using a Perkin-Elmer Spectrum One instrument. Less than 10 mg of powder was mixed with KBr salt. This mixture was pressed into a pellet and then dried in air at $120^{O}C$ overnight before the measurements were taken. The measured spectra range was from 400-4000/cm.

Thermogravimetric analysis (TGA) was performed using a Perkin-Elmer TGA 7 unit. Typical samples were approximately 35 mg. These measurements were performed in air from room temperature up to $620^{O}C$.

3.2.5 Electrochemical characterization

Electrochemical tests were preformed using a MACCOR electrochemical test system. Preparation of the electrodes was described in the first chapter. In brief, a paste of electrode material was casted onto an aluminium substrate via a doctor blade process. The

paste consisted of 80% active material, 10% graphite, 3% flakey carbon, and 7% polyvinyl diflouride by weight. The counter and reference electrode were lithium metal and a 1M $LiPF_6$ salt in a 1:1 ethylene carbonate to dimethyl carbonate solvent (Merck) was used as an electrolyte. A porous polyethylene sheet, Solupor (DSM), separated the electrodes in a coin cell CR 2320 type of package (Hohsen). The assembly of the cells took place in an Ar filled glovebox. The cells were charged and discharged at a C/10 rate between the potentials of 2.6-0.6V.

3.3 Results and discussion

3.3.1 Chemical titration

3.3.1.1 Titration curves and XRD of the solids

Figure 3-1 presents the titration curves, i.e., pH of the solution as a function of volume of acid injected into the solution for material that was ball milled for 0, 2, and 6 hours. The titration curves for all three preparations of this material exhibit a similar shape. Initially, all three materials produced a basic solution when first introduced into water. An initial pH of 10.2 is observed, if the non-milled material was first introduced into the deionized water. In the case of the ball-milled material, the initial pH of the solution is slightly greater at a value of 10.8. As acid is injected into the solution, the pH of the solution decreases until a buffer region is reached between a pH of 5-4. Below a pH of 4, the curve continues to decrease to a pH of 2, where the solution is saturated with acid.

A comparison of the titration curves between the spinel materials to the curve of a blank solution that contained only deionized water is also presented in Figure 3-1. The titration curve of the blank solution exhibited no buffer region as the pH quickly decreases to a pH of 2 with a very small volume of injected acid. From this comparison, it is reasonable to assert that protons are being consumed when $Li_4Ti_5O_{12}$ particles are present in the solution.

Figure 3-1 also presents the influence of ball-milling time of this material to the amount of acid consumed in the buffer region. As milling time increased from 0 to 6 hours, the buffer region increased from 0.9 to 1.7 ml of acid. This increase of the buffer region

may indicate that the consumption of protons is greater for the 6-hours ball-milled sample than for that of the non-milled sample. This effect is apparently due to the reduction of particle size when milling time increases. This particle size reduction then increases the surface area of this material that would, in turn, increase the sites that proton consumption can take place between the solution and the solid material.

The structure of the 6-hours ball-milled sample was examined using X-ray diffraction before and after acidic titration. This sample was chosen, because it showed the greatest neutralization of acid as presented in Figure 3-1. The XRD patterns show that the structure practically does not change before or after titration as presented in Figure 3-2. Thus, the spinel structure is retained after titration with no obvious changes to the lattice parameter.

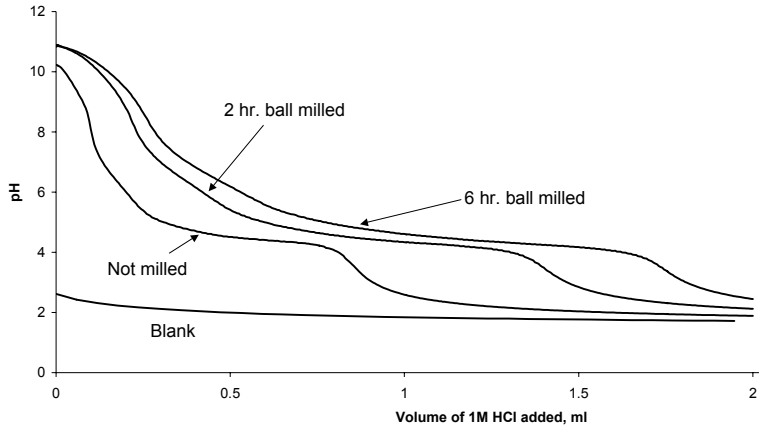

Figure 3-1 Titration of water with 1M HCl that include non-milled and ball-milled $Li_4Ti_5O_{12}$ material. A blank solution is included for comparison

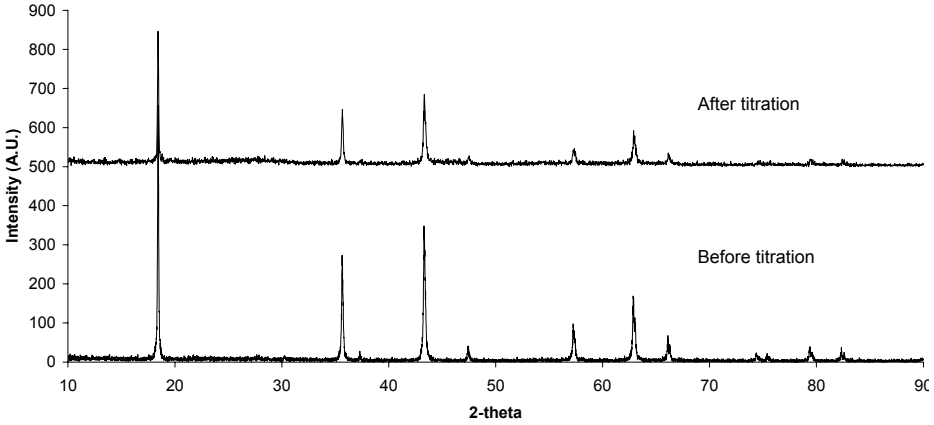

Figure 3-2 XRD patterns of the 6-hours ball-milled sample before and after titration

3.3.1.2 Atomic adsorption spectroscopy (AAS)

To determine whether $Li_4Ti_5O_{12}$ is being dissolved in solution, AAS was employed. The results are presented in Table 3-1. From this Table, it is clear that Li^+ ions are the primary ions found in solution. This is in contrast to Ti where no significant quantities were found. By taking into account that the error for this analysis is approximately 5%, the percentage of reported Ti is considered negligible. Thus, it is assumed that no Ti is in solution. Since all Ti ions in this particular material are in a 4+ oxidation state, it is highly unlikely that the solution can reduce to H_2 or O_2 gas, when Li^+ ions are released from the spinel. Furthermore, since the structure of the material does not change before or after it was in contact with the acidic solution, it is reasoned that protons exchanges with Li^+ ions in this material. It is known that protons exchange with other lithium containing spinels (10,15-18) as well as other lithium titanates (19) and partial lithium manganese titanates (11). However, to the best of the author's knowledge, a detailed study of proton exchange with this material has not yet been reported.

By assuming that the concentration of Li^+ ions in solution is equal to the concentration of protons that is exchanged into the structure and that the oxide ion content of the spinel framework is constant, the amount of exchanged protons can be calculated. This is presented as an empirical chemical composition presented in Table 3-1. This Table also shows the dependence of the amount of proton exchange to the particle size and time in acidic solution. By comparing the percentages of Li^+ ions found in solution between non-milled to the 6-hours ball milled samples (i.e., samples A and C), the amount of ion exchange can be compared to the ball milling time. The amount of ion exchange increases from 18% for the non-milled sample to 36 % for the 6-hours milled sample. This is presumably due to the reduction of particle size and hence an increase in surface area as ball milling time increases. For non-milled samples (i.e., samples A, D, and E), the treatment time or the time that the material was in an acidic solution may also be compared. The amount of ion exchange increases from 18% with a 1day treatment to 49% with a 26-days treatment. This suggests that the exchange rate is rather slow at room temperature. The largest amount of proton exchange is 68% for sample F. The treatment conditions for this sample included the submergence of a 6-hours ball-milled sample in an acidic solution that was heated for 10 days.

Table 3-1 Sample preparation and AAS results. The percentages of Li and Ti are calculated from the initial amount of $Li_4Ti_5O_{12}$ spinel in the solution.

Sample	Material	Acid	Treatment	%Li (wt) (% ion exchanged)	%Ti (wt)	Empirical Chemical Composition
A	Non-milled	1M HCl	1 day RT	18	0.048	$H_{0.23}Li_{1.10}Ti_{1.67}O_4$
B	2hr ball mill	1M HCl	1 day RT	32	0.083	$H_{0.43}Li_{0.90}Ti_{1.67}O_4$
C	6hr ball mill	1M HCl	1 day RT	36	0.042	$H_{0.48}Li_{0.85}Ti_{1.67}O_4$
D	Non-milled	1M HCl	10 days, RT	39	0.023	$H_{0.53}Li_{0.80}Ti_{1.67}O_4$
E	Non-milled	1M HCl	26 days, RT	49	0.063	$H_{0.65}Li_{0.68}Ti_{1.67}O_4$
F	6hr ball mill	1M HCl	10 days, 50°C	68	0.193	$H_{0.90}Li_{0.43}Ti_{1.67}O_4$

3.3.1.3 FTIR transmission

As a confirmation of ion exchange, FTIR transmission was performed for some of these samples. Figure 3-3 presents the FTIR transmission spectra in the range of 400 to 4000/cm for the pure and titrated materials. The empirical chemical composition of these materials is listed in Figure 3-3. From previous studies of proton exchange in lithium manganate spinels, it is known that protons in spinel structures appear in the spectra at approximately 1600/cm, 3400/cm, and 910/cm (11,20). This is indeed the case, because a strong peak appears at 3400/cm indicating O-H stretching for the titrated samples. A weaker peak arises at 1600/cm that also indicates proton insertion being assigned to water bending. The weak peak at circa 910/cm is associated with protons in the spinel (4) Compared to the titrated material, some peaks from the original $Li_4Ti_5O_{12}$ disappear in the range of 1000/cm and 1500/cm. This has been interpreted as surface hydroxyl groups on the original spinel (10). The known spinel vibrations are at the low wavenumbers in the range of 400-700/cm (21). These peaks become less intense as more Li^+ ions is exchanged with protons. It is interesting to note that the spectra of the

original $Li_4Ti_5O_{12}$ material exhibit some bands where proton exchange is known to occur. Since these materials were exposed to air for approximately 6 months before the material was analyzed, it suggests that this material may have reacted with water from the air itself. Further evidence of this is given in the electrochemical testing.

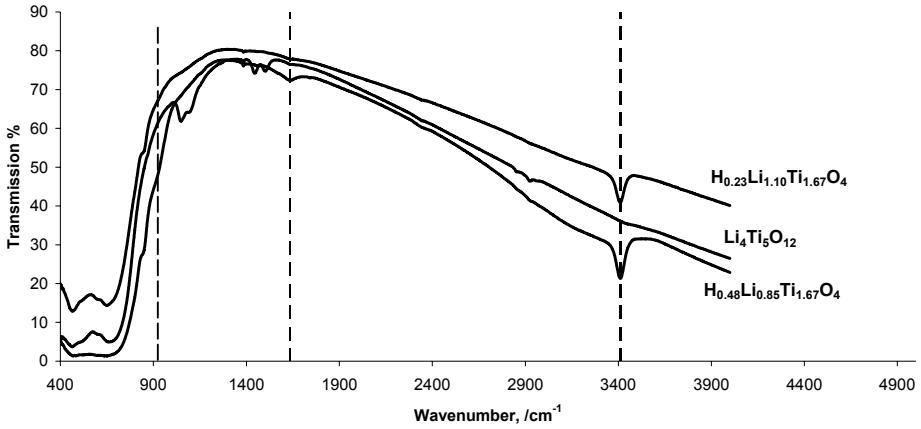

Figure 3-3 FTIR transmission spectra of $Li_4Ti_5O_{12}$ and its proton-exchanged counterparts

3.3.1.4 Neutron diffraction

The diffraction pattern of the exchanged material $H_{0.90}Li_{0.43}Ti_{1.67}O_4$ (sample F) is presented in Figure 3-4. The diffraction pattern can be indexed with the Fd3m space group, which is the same as that of the pure spinel. The fit results of the pure spinel material were compared with the proton-exchanged material in order to give a 3-D positional map of the protons residing in the structure. A cross section of this map is shown in Figure 3-5. This map suggests that the protons reside on the 48f and on the 8a sites as indicated by the dark spots on the map. The proton positions found were included in the Rietveld refinement. In addition, the results given from the AAS measurements were used to constrain the occupancies in the fitting. By including the protons on the specified positions, the fit quality significantly improved. This led to the residual of the fit shown in Figure 3-4.

The fit results of the atomic positions and occupancies are presented in Table 3-2. From these results, the bulk of the exchange occurs at the tetrahedral Li 8a sites. These sites

are directly exchanged with protons in the same position. This is in contrast to the $Li_4Mn_5O_{12}$ counterpart where a relatively small amount of protons (approximately 18%) is found on the 8a sites, while the bulk protons reside on the 96g sites (15).

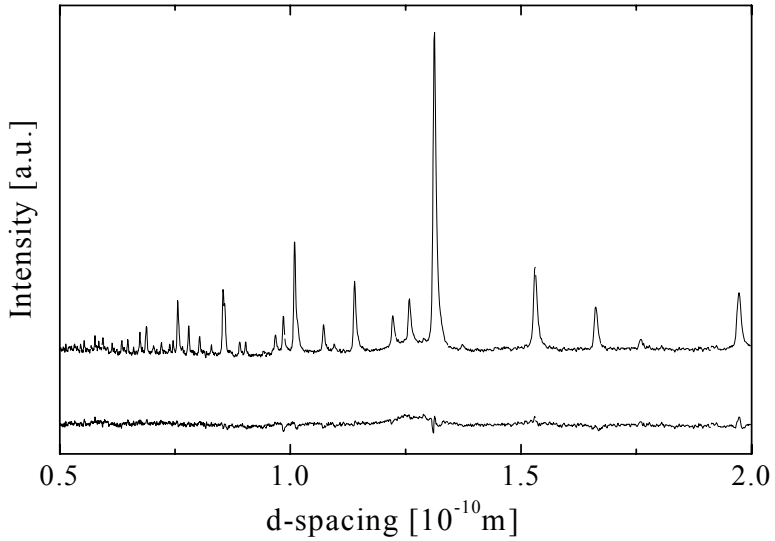

Figure 3-4 Neutron diffraction pattern of $H_{0.90}Li_{0.43}Ti_{1.67}O_4$ with fitting residual below

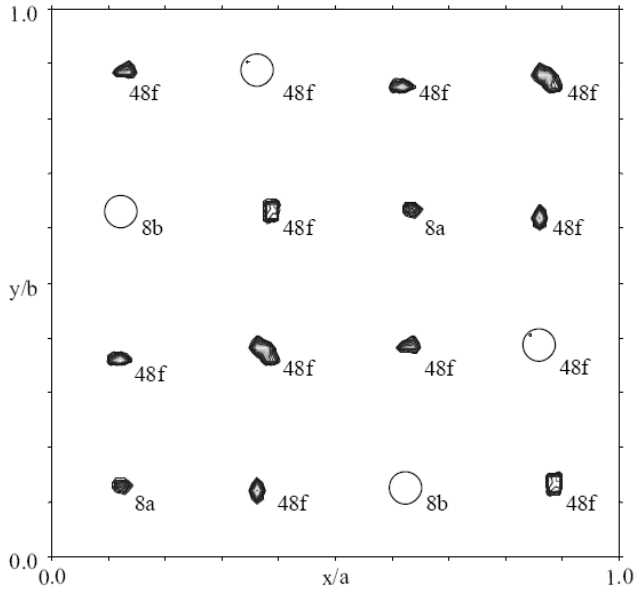

Figure 3-5 Cross section positional map showing protons and Li^+ ions that reside in $H_{0.90}Li_{0.43}Ti_{1.67}O_4$. The dark spots mark the positions of these ions and the white circles indicate empty sites

Table 3-2 Position of ions from Rietveld fitting results with the occupancy is listed

Atom	Site	x/a, y/b, z/c	Occupancy
H	48f	0.9111, 1/8, 1/8	0.026
H	8a	1/8, 1/8,1/8	0.728
Li	8a	1/8, 1/8,1/8	0.097
Li	16d	1/2, 1/2,1/2	0.14
Ti	16d	1/2, 1/2,1/2	0.83
O	32e	0.2615, 0.2615, 0.2615	1.0

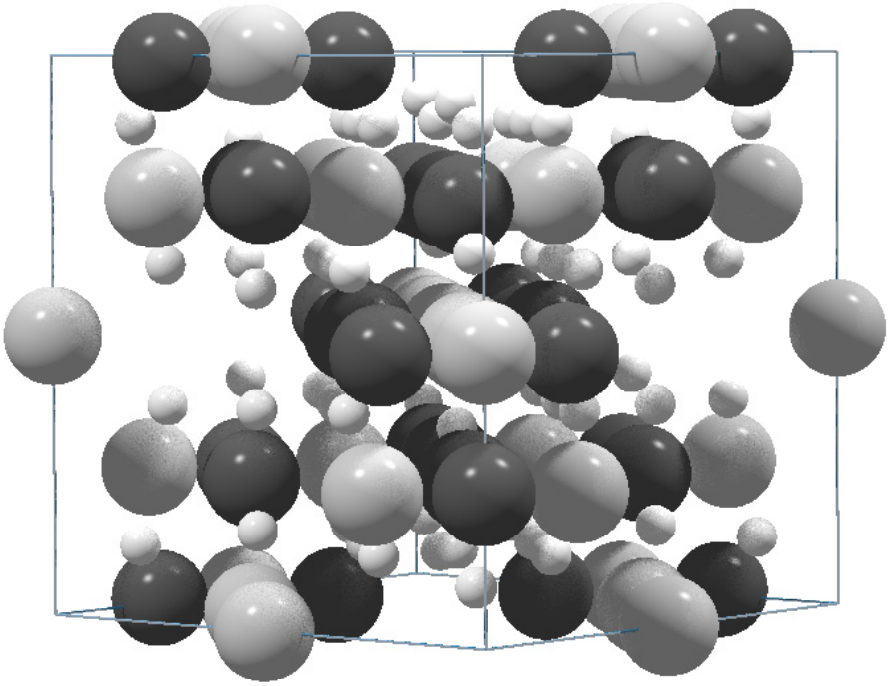

Figure 3-6 A schematic drawing of the $H_{0.90}Li_{0.43}Ti_{1.67}O_4$ material. Large dark spheres represent oxide ions. To illustrate the planes that these ions lay, the large light spheres are 16d Li and Ti ions and small spheres are randomly distributed Li ions and protons

The structure can be described best as alternating sheets of octahedrally positioned Li^+ and Ti^{4+} ions with tetrahedral 8a protons and Li^+ ions, and protons positioned on the 48f sites. Figure 3-6 graphically presents the positions of these atoms. The 8a and 48f sites that are indicated by the small spheres in this figure are located between the planes of oxide ions and octahedrally positioned Ti^{4+} and Li^+ atoms and the oxide ion framework as indicated by the large spheres in this figure.

The 48f sites have in addition to the oxide-ion tetrahedron, 2 $-Ti^{4+}$ neighbors at a distance comparable to the nearest oxide ion. As somewhat expected, the proton does not lie directly in the center of the oxide-ion tetrahedron of the 48f site, but is shifted towards the nearest oxide ion and away from the two nearest Ti^{4+} ions. This may be due to the local positive partial charges that the two Ti^{4+} ions exert on this site. This is the reason that the proton density is not visible for the two 48f sites shown in Figure 3-5. Although the 8b sites lay on the same plane as the 48f and 8a sites, the 8b sites contain tetrahedrally coordinated oxide ions and 4 $-Ti^{4+}$ neighbors. The 8b sites are not occupied probably because of the positive partial charges that that this site contains from the 4 – Ti^{4+} ion neighbors.

The fit also provided a significant but small decrease of the lattice parameter of 0.25%. The lattice parameter for the pure material and proton-exchanged material was 8.3595 Å and 8.3381 Å, respectively. Although it is known that the same material does not exhibit any obvious volume change when Li^+ ions are inserted (22,23), it is nevertheless unusual that the proton exchange has such small a affect on the volume change. Generally, the volume shrinkage for other proton-exchanged materials are rather significant when compared to $Li_4Mn_5O_{12}$ (1.35%) (24) as well as other lithium titanates (3.61%) (19).

3.3.1.5 Thermogravimetric analysis and XRD

Figure 3-7 presents comparative curves of weight loss as a function of temperature between untreated and treated samples. For the material that was not treated with acid, a slight weight loss was observed. It was also observed that a slight difference of weight loss occurred when comparing the non-ball milled material to the ball-milled material. This may be due to the increased surface area when the material was ball milled and ex-

posed to normal air. The greatest weight loss for all samples occurred in a temperature range of 240-440^{O}C. Beyond 440^{O}C, all samples were relatively stable up to 600^{O}C.

By comparing the traces between the treated and untreated samples, the amount of weight loss between these samples is significant. For the untreated samples, the largest amount of weight loss at 600^{O}C is 0.75%. When comparing the 6-hour ball milled sample that has been treated, the weight loss is 4.24% at 600^{O}C. Since all of the curves for all of the samples show similar behaviour, it is anticipated that the same reaction occurs for all measured samples.

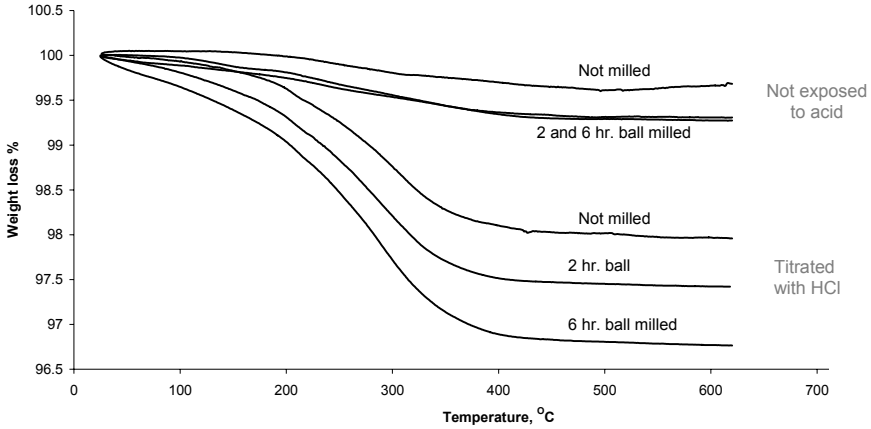

Figure 3-7 TGA curves for ball milled and non-milled samples that were treated and untreated in acidic solutions

Figure 3-8 presents a series of XRD patterns for the 6-hours ball-milled samples that were taken before titration, after titration and, heated to 600^{O}C. As shown previously from Figure 3-2, this material does not change before or after titration. However, when this material was heated to 600^{O}C, the XRD pattern shows the presence of two distinct phases. The first phase is the spinel phase while the second phase is the anatase TiO_2 phase. This suggests that protons leave the structure as water when heated. It is presumed that practically all of the protons exit the structure as water beyond 440^{O}C since the TGA trace is relatively stable beyond that temperature.

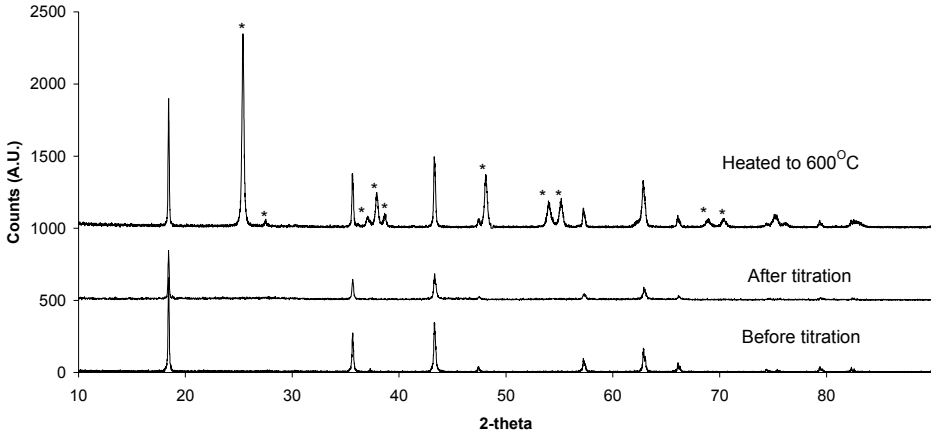

Figure 3-8 XRD patterns for the 6-hours ball-milled sample before and after titration and heated to 600°C. The astrix designates anatase TiO_2 phase

To ensure the correct composition of protons in the structure, the weight loss measured by TGA is compared to the amount of protons in the structure measured by AAS. This comparison is presented in Table 3-3. From this table, a good match between the results of both analytical techniques is found within the experimental error. Thus, the degree of proton exchange between the materials seems reasonable.

Table 3-3 Comparison of weight loss at 600°C between TGA measurements and the amount of protons calculated in the structure using AAS results

Sample	TGA results	AAS calculated	% Difference
D	3.2147	3.26	1.39
E	3.8484	4.03	4.51
F	5.5873	5.60	0.23

3.3.1.6 Reaction mechanism

Two reactions are being proposed when this material is exposed to acidic environments. The first reaction is the ion exchange reaction given in Equation 3-1. The second proposed reaction is presented in Equation 3-2. This equation expresses the changes that the exchanged material experiences when heated above 440°C.

$$Li_4Ti_5O_{12(s)} + xH^+_{(aq)} \rightarrow H_xLi_{(4-x)}Ti_5O_{12(s)} + xLi^+_{(aq)} \quad (3.1)$$

$$4H_xLi_{(4-x)}Ti_5O_{12(s)} \xrightarrow[440°C]{} 2xH_2O_{(g)} + 5xTiO_{2(s)} + (4-x)Li_4Ti_5O_{12(s)} \quad (3.2)$$

3.3.2 Electrochemical characterization

3.3.2.1 Proton-exchanged material

The next three figures present the cell potential versus lithium metal with intercalation and deintercalation of Li^+ ions as more protons are present in this spinel. It may be helpful at this point to review the relation between potential curves and the phases that are associated with these curves. It is generally accepted that sharp potential slopes indicate single-phase regions, while a gradual sloping potential indicates a solid-solution region. A flat potential curve typically represents a two-phase region (25).

For the pure $Li_4Ti_5O_{12}$ spinel material, a simple potential curve is found as lithium is intercalated and deintercalated. From literature, as lithium is intercalated into this material, a sharp potential drop from its open circuit voltage of 2.9 to 1.55V indicates a single-phase region $Li_4Ti_5O_{12}$. A flat potential or a two-phase region with phases $Li_4Ti_5O_{12}$ plus $Li_7Ti_5O_{12}$ at 1.55V for 95% of its capacity follows this single-phase region. Finally, a single-phase region, $Li_7Ti_5O_{12}$, with a sharp potential drop from 1.55 to 0.8V was found. These phases are extremely reversible as lithium is extracted from the structure with less than 2% capacity loss (26).

The cell potential curves for sample A are presented in Figure 3-9a. This material contains the least amount of protons. An immediate potential drop from 2.6V to 1.8V is first observed as Li^+ ions are intercalated into the structure. This indicates that a single phase is present. A sloping potential curve that corresponds to a solid solution region is observed between a potential range of 1.8 to 1.55V. As intercalation proceeds, a relatively flat potential that indicates a two-phase region at 1.55V is present. Finally, a gradual slope from 1.55 V to 0.6V is observed, which indicates a solid-solution phase.

These phases are reversible as Li^+ ions are deintercalated from the material. A sloping potential is first observed between 0.6 to 1.55V. This is followed by a relatively flat potential for most of its capacity at 1.55V. Finally, a sloping potential is seen in a potential range of 1.55 to 2V.

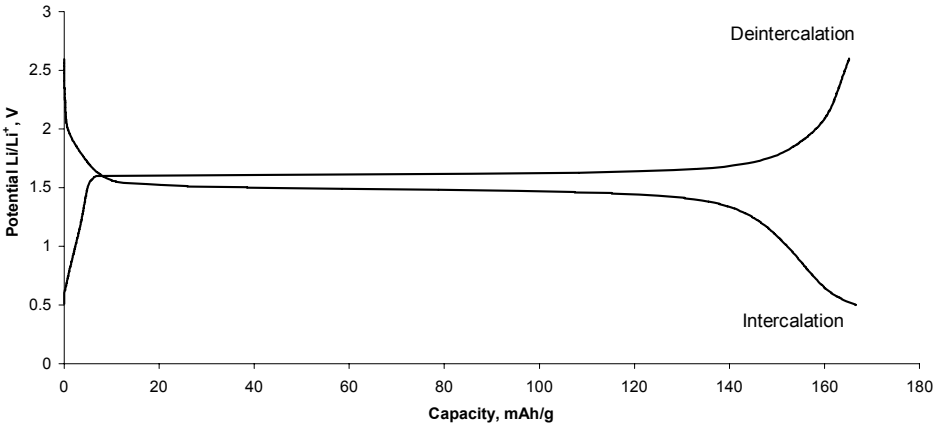

Figure 3-9a Potential vs. capacity of sample A ($H_{0.23}Li_{0.90}Ti_{1.67}O_4$). Li metal was used as a counter and reference electrode

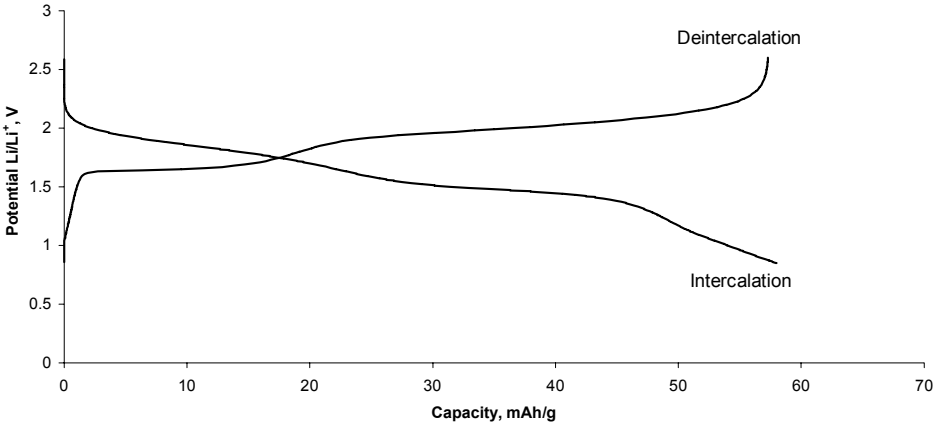

Figure 3-9b Potential vs. capacity of sample D ($H_{0.53}Li_{0.80}Ti_{1.67}O_4$). Li metal was used as a counter and reference electrode

As more protons are present in the structure, the cell capacity decreases while the first solid solution phase dominates the potential curve. Figure 3-9b presents the potential curves for sample D where the proton mol ratio was calculated to be 0.53. This figure clearly presents the existence of all present phase regions. As lithium is intercalated into this structure, a single phase between a potential range of 2.6 to 2V. This is followed by a solid solution in a potential range of 2 to 1.55V. A two-phase region at 1.55V for approximately 25% of its capacity is present. Finally, a solid-solution region in a potential region of 1.5 to 0.8 V is present. These phases are reversible as lithium is deintercalated from the structure.

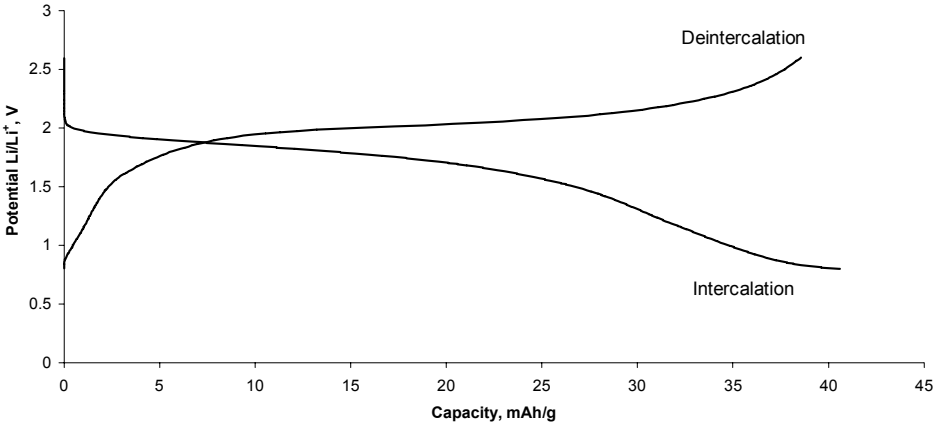

Figure 3-9c Potential vs. capacity of sample F ($H_{0.90}Li_{0.43}Ti_{1.67}O_4$). Li metal was used as a counter and reference electrode

The potential curves for sample F, which contains the largest amount of protons in the spinel ($H_{0.90}$), is presented in Figure 3-9c. One of the features for this material is the lack of the flat 1.55V plateau region. However, two sloping potentials are present between the potentials of 2 and 1.55V and from the 1.55 to 0.8V potential range. These potential curves are reversible. This implies that protons remain in the structure during the intercalation process.

3.3.2.2 Commercial $Li_4Ti_5O_{12}$

The electrochemical results of the commercial $Li_4Ti_5O_{12}$ spinel material gave some unexpected results. A series of electrochemical curves are presented in Figures 3-10a to 3-

10c. The first figure presents the intercalation and deintercalation potential curves for the commercial $Li_4Ti_5O_{12}$ spinel material, when just received. This material exhibits the well-known potential characteristics as Li^+ ions are inserted and extracted. A flat potential of 1.55V during most of its capacity is observed as well as a low polarization during charge and discharge.

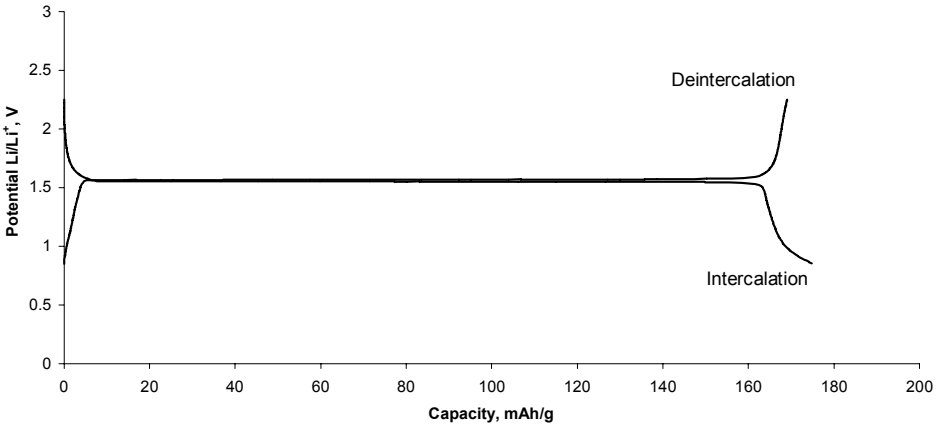

Figure 3-10a Potential vs. capacity of as received material. Li metal was used as a counter and reference electrode

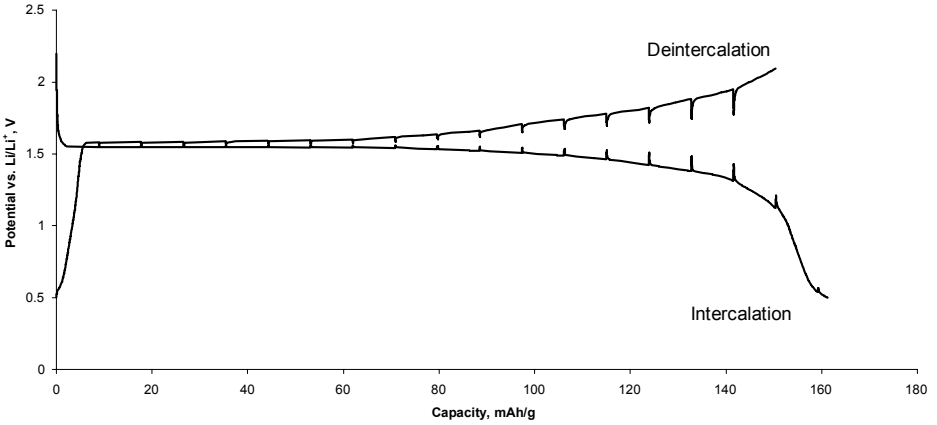

Figure 3-10b Potential vs. capacity of the same material as in Figure 3-11a that was exposed to air for 6 months. Li metal was used as a counter and reference electrode

However, when this material is exposed to air for more than 6 months, a change in the potential curves is observed which is presented in Figure 3-10b. This material exhibits a more pronounced polarization of the potential curve between intercalation and deintercalation of Li^+ ions. In the beginning of intercalation, an initial flat potential of 1.55V is observed. Unlike Figure 3-10a, the flat potential does not remain at 1.55V but rather gradually decreases below this potential as the insertion of Li^+ ions proceeds. Upon the removal of Li^+ ions, the initial flat potential of 1.55V is first observed but the potential gradually increases as deintercalation proceeds.

Figure 3-10c presents the potential curves as a function of capacity when the same air exposed material is annealed to $900^{O}C$. This material exhibits a similar shape of the potential curve as observed for the as received material for both intercalation and deintercalation. In addition, the polarization of the potential curve for intercalation and deintercalation is similar to that of the as received material.

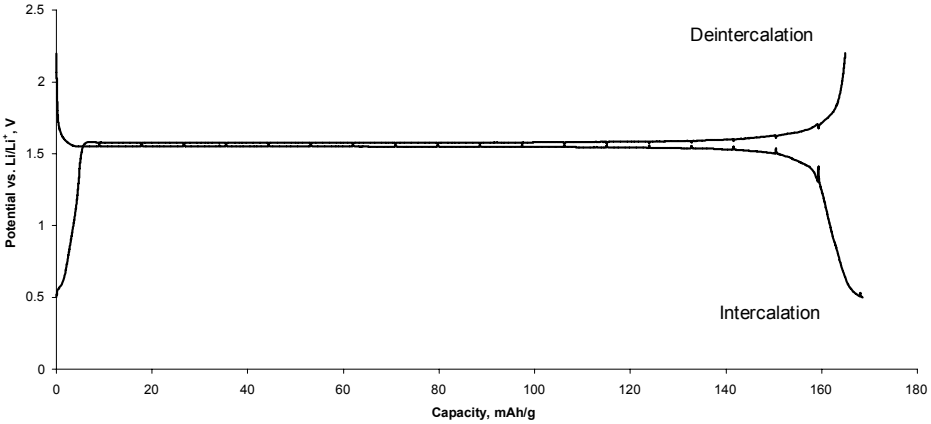

Figure 3-10c Potential vs. capacity of the same material as in Figure 3-11b that was annealed in air. Li metal was used as a reference

Because the XRD pattern of the 6-months air-exposed $Li_4Ti_5O_{12}$ material shows the same spinel pattern as for the as received $Li_4Ti_5O_{12}$ spinel, gross contamination (> 5% by volume) of the commercial material between the 6-month time period is unlikely. Furthermore, by annealing the 6-months air-exposed material, the electrochemical performance returns to its as received form. Taking this into consideration, it is suspected

that water from the atmosphere reacted with $Li_4Ti_5O_{12}$. Support for this explanation is given by Li et al. (27) where these authors predicted the stability of Li-containing materials in aqueous solutions. By using their calculations, this material should be stable at a solution pH in the range of 11.7-8.3. Experimental support of this prediction is given from the current work where the initial pH of 10.8 is observed in deionized water. Since the atmosphere pH is not strongly basic, the stability of $Li_4Ti_5O_{12}$ in a normal atmosphere is suspect. This may give rise to an ion exchange between Li^+ ions and protons at the surface of the particles. Because the exchange is slow, a small percentage of ion exchange occurs during the 6-months period probably occurred. Thus, the amount of capacity loss due to ion exchange before annealing or, due to the formation of anatase TiO_2, after annealing is small. However, the polarization of the cell is significant. In essence, care must be taken when storing these materials.

3.4 Conclusions

Based on the present results, the $Li_4Ti_5O_{12}$ spinel material is not stable towards acidic solutions. From potentiometric titration measurements, protons are being consumed as acid is continuously added into the solution with $Li_4Ti_5O_{12}$. Evidence of proton exchange has been given through AAS and FTIR measurements. From AAS analysis, only Li^+ ions leave the structure in the acidic solution. The FTIR transmission spectra have shown peaks where protons are generally present in a spinel material.

From neutron and XRD diffraction, the structure of the ion-exchanged material is spinel. It was found that most protons reside on the tetrahedrally coordinated 8a sites where part of the Li^+ ions resided in the pure material. In addition, some of the 16d Li sites have been replaced by protons but reside on the 48f sites. The structure is visualized as alternating planes of octahedrally coordinated 16d Li^+ and Ti^{4+} ions with planes of 8a and 48f sites of Li^+ ions and protons. Finally, a slight reduction of the initial volume of 0.25% is observed when comparing the initial material to the exchanged material.

Upon heating the exchanged material, protons begin to leave the structure at 240^OC as water and at 440^OC the protons are completely removed. The resulting material is a composite consisting of anatase TiO_2 and $Li_4Ti_5O_{12}$ spinel that presumably have not

been exchanged. Two reactions are proposed: first a direct ion exchange between Li^+ ions and protons and second the removal of protons as water when the material is heated at 400^OC.

Electrochemical results show that the capacity of the material decreases with increasing ion exchange. As more protons are present in the structure, the original flat potential at 1.55V becomes less distinguishable, while the formation of sloping potentials above and below the original 1.55V plateau are observed.

The stability of the commercial $Li_4Ti_5O_{12}$ material when exposed to open air for a 6-month time period is suspect. Additional electrochemical results show the performance of this material degrades as the polarization of the potential has increased. This may be linked to the proton exchange that was observed in this study. However, the performance of this material is returned to its original properties by an annealing process.

3.5 References

1. Thackeray, M. M. *Progress in Solid State Chemistry* **1997,** *25* (1-2), 1-71.
2. Aurbach, D.; Weissman, I.; Zaban, A.; Dan, P. *Electrochimica Acta* **1999,** *45*(7), 1135-1140.
3. Aurbach, D.; Schechter, A. *Electrochimica Acta* **2001,** *46*(15), 2395-2400.
4. Lavela, P.; Sanchez, L.; Tirado, J. L.; Bach, S.; Pereira-Ramos, J. P. *J. Solid State Chem.* **2000,** *150*(1), 196-203.
5. Feng, Q.; Kanoh, H.; Miyai, Y.; Ooi, K. *Chem. Mater.* **1995,** *7*(2), 379-384.
6. Feng, Q.; Miyai, Y.; Kanoh, H.; Ooi, K. *Langmuir* **1992,** *8*(7), 1861-1867.
7. Hunter, J. C. *J. Solid State Chem.* **1981,** *39* 142-147.
8. Lubin, F.; Lecerf, A.; Broussely, M.; Labat, J. *J. Power Sources* **1991,** *34*(2), 161-173.

9. Ammundsen, B.; Jones, D. J.; Roziere, J.; Burns, G. R. *Chem. Mater.* **1996,** *8*(12), 2799-2808.

10. Ammundsen, B.; Aitchison, P. B.; Burns, G. R.; Jones, D. J.; Roziere, J. *Solid State Ionics* **1997,** *97*(1-4), 269-276.

11. Aitchison, P.; Ammundsen, B.; Bell, T.; Jones, D.; Roziere, J.; Burns, G.; Berg, H.; Tellgren, R.; Thomas, J. *Physica B* **2000,** *276* 847-848.

12. Colbow, K. M.; Dahn, J. R.; Haering, R. R. *J. Power Sources* **1989,** *26*(3-4), 397-402.

13. Ohzuku, T.; Ueda, A.; Yamamoto, N. *J. Electrochem. Soc.* **1995,** *142*(5), 1431-1435.

14. Williams, W. *Physica B* **1998,** *241-243* 234-236.

15. Ammundsen, B.; Jones, D. J.; Roziere, J.; Berg, H.; Tellgren, R.; Thomas, J. O. *Chem. Mater.* **1998,** *10*(6), 1680-1687.

16. Ammundsen, B.; Roziere, J.; Islam, M. S. *J. Phy. Chem. B* **1997,** *101*(41), 8156-8163.

17. Ooi, K.; Miyai, Y.; Sakakihara, J. *Langmuir* **1991,** *7*(6), 1167-1171.

18. Kim, Y. S.; Kanoh, H.; Hirotsu, T.; Ooi, K. *Bull. Chem. Soc. Japan* **2002,** *75*(1), 55-58.

19. Corcoran, T. D. P; Irvine. J. *Solid State Ionics* **2000,** *136-137* 297.

20. Feng, Q.; Honbu, C.; Yanagisawa, K.; Yamasaki, N.; Komarneni, S. *J. Mater. Chem.* **2000,** *10*(2), 483-488.

21. Allen, G. C.; Paul, M. *Appl. Spectroscopy* **1995,** *49*(4), 451-458.

22. Ohzuku, T.; Ueda, A.; Yamamoto, N. *J. Electrochem. Soc.* **1995,** *142*(5), 1431-1435.

23. Scharner, S.; Weppner, W.; Schmid-Beurmann, P. *J. Electrochem. Soc.* **1999,** *146*(3), 857-861.

24. Ammundsen, B.; Jones, D. J.; Roziere, J.; Burns, G. R. *Chem. Mater.* **1996,** *8*(12), 2799-2808.

25. Bruce, P. G. *Solid State Electrochemistry;* First ed.; Cambridge: 1995.

26. Colbow, K. M.; Dahn, J. R.; Haering, R. R. *J. Power Sources* **1989,** *26*(3-4), 397-402.

27. Li, W.; McKinnon, W. R.; Dahn, J. R. *J. Electrochem. Soc.* **1994,** *141*(9), 2310.

4

Magnetic Characterization of $Li_{(1+\delta)}Mn_{(2-\delta)}O_4$ and Li extracted Spinels

Abstract

Magnetic characterization of chemically delithiated $Li_xMn_{(2-x)}O_4$ for $0 \leq x \leq 1$ are presented and compared with substituted $Li_{(1+\delta)}Mn_{(2-\delta)}O_4$ for $0 \leq \delta \leq 0.33$ spinels. From magnetic susceptibility measurements in the temperature range of 300-500K, two distinct trends were found as a function of the Weiss temperature and lattice parameter. The first trend involves both chemically delithiated and Li-substituted spinels. The second trend involves primarily from the chemically delithiated spinels. Furthermore, it was determined that all Mn^{3+} cations are in a high-spin configuration. An explanation of ion interactions with magnetic interactions is presented.

4.1 Introduction

As discussed in Chapter 1, the MnO_2 spinel framework provides room for lithium ion transport while maintaining its cubic structure over the compositional range $Li_xMn_2O_4$, with $0 \leq x \leq 1$. A gradual increase of the average Mn valence occurs over the valence range from 3.5 to 4.0. For battery applications, such as the Li-ion system, only extraction and insertion of Li^+ ions in the compositional range of $0 \leq x \leq 1$ is interesting. Upon Li-ion extraction, Mn^{3+} is oxidised to Mn^{4+}. It was found later that Li^+ ions cannot be extracted practically beyond a lithium content of 0.27(1). This leads to a capacity reduction of the material compared from the theoretical capacity of 148 mAh/g to a practical capacity of about 120 mAh/g.

Another way to extract Li^+ ions from the parent spinel is to chemically extract Li^+ ions by submersing the $LiMn_2O_4$ material into an acidic solution. In brief, this reaction involves a redox mechanism of the Mn^{3+} cations to Mn^{4+} and Mn^{2+} cations. The Mn^{2+} cations would go into solution, while the Mn^{4+} cations remain in the solid to eventually form the λ-MnO_2 spinel. Thus, the average Mn valence state would increase in the same manner as electrochemically removing the Li^+ ions (2-4).

Another way to increase the Mn valence state is by cation substitution. These doped materials use Li^+ ions as a substitute for a maximum of 1/6 of the Mn^{3+} cations in the $LiMn_2O_4$ material. This substitution also raises the average valence state of the Mn from 3.5 to 4.0. The empirical formula for these materials is $Li_{(1+\delta)}Mn_{(2-\delta)}O_4$ with $0 \leq \delta \leq 0.33$. The substituted spinels have also been used for battery applications (5,6). Typically for very low δ values (0.04) the spinel is used as a cathode in the Li-ion battery system. For high δ values (0.33) all Mn cations are in 4+ oxidation state. While, it was reported recently that this material may be used as a cathode (7), this spinel is generally used as an anode material.

The electrical conduction of this material has been examined by various groups (8,9). One way to obtain information about the electrical conduction of a material is to examine the magnetic interactions of ions in a material. These magnetic interactions may provide information on the electronic interactions between the ions within a material (10).

Many groups have reported the magnetic properties of the lithium manganate spinels (10-17). Typically, these properties were studied as a function of the increasing Mn oxidation state. There are two general cases where this was accomplished. Some groups have reported the magnetic properties of the substituted and defect spinels as more Mn is substituted for Li (13,18). Other groups have reported these properties for the Li-ion extracted spinels as a function of Li-ion extraction (14,15,17). Between the two cases, there seems to be a discrepancy in the Weiss temperature between the λ-MnO_2 and the fully substituted spinel $Li_{(1+\delta)}Mn_{(2-\delta)}O_4$ (δ=0.33) or $Li_4Mn_5O_{12}$. The negative or positive value of the Weiss temperature empirically indicates the antiferromagnetic and ferromagnetic interactions between the Mn cations, respectively. This work examines and compares the magnetic properties of the substituted and the chemically Li-extracted $LiMn_2O_4$ spinels as a function of lattice parameter and Mn valence state.

4.2 Experimental

4.2.1 Substituted spinels

Stoichiometric and substituted Li-Mn spinels ($Li_{(1+\delta)}Mn_{(2-\delta)}O_4$ with $0\leq\delta\leq0.33$) were produced from proper amounts of manganese acetate (Fluke) and lithium hydroxide (Fluke). Multiple heating schemes with a heating rate of 10°C/min and a cooling rate of 5°C/min and various soak temperatures and times were employed. In general, these schemes followed that of Masquelleir et al.(13) and are presented in Table 4-1 in Section 4.3.1.

4.2.2 Chemical extraction of $Li_{(1+\delta)}Mn_{(2-\delta)}O_4$

Chemical extraction of commercial $Li_{(1+\delta)}Mn_{(2-\delta)}O_4$ (Honeywell) with δ=0.04 was performed using a Metrohm automatic tritrator. A series of 4-grams powdered samples was submersed in 75 ml of de-ionized water. Li^+ ions were progressively extracted from the samples using 1M H_2SO_4(Baker). The volume of acid that was used was in the range of 2-20ml. This mixture was under constant stirring that continued, until a stable potential reading of a combined glass electrode with an Ag^+/AgCl reference electrode was achieved. Subsequently, the particles were collected, washed with deionised water, and dried at 120°C.

4.2.3 Determination of the Mn oxidation state

The Mn oxidation state was determined using the Jeager-Vetter titration technique as described in more detail elsewhere(19). In principle, the samples were first dissolved in a $FeSO_4$ solution and back titrated with $KMnO_4$ (Merck). A Metrohm automatic titrator was used for this measurement. These measurements were then used to calculate δ in $Li_{(1+\delta)}Mn_{(2-\delta)}O_4$ and the Mn oxidation state for chemically extracted $LiMn_2O_4$.

4.2.4 X-ray diffraction

All materials were structurally characterized by the X-ray diffraction technique (XRD). The X-ray diffraction measurements were performed on a Bruker-AXS with a diffracted beam graphite monochrometor using Cu K_α radiation at room temperature. The room temperature measurements were performed in the 2-Θ range of 10-90°.

4.2.5 Magnetic measurements

The magnetic susceptibility measurements were performed using the Faraday method with an ordinary magnet. The measurements were carried out in air and in a temperature range of 294-500K. Much care was taken towards the heating of the samples. Each point was measured after 1 hour of heating. The magnetic field that was used was 9000 Gaussians. Tris (ethylenediamine) nickel (II) thiosulfate or $Ni(en)_3S_2O_3$ was used as a calibration standard. Typical samples weighed approximately 35 mg after drying over-night in a furnace heated to 120^OC.

4.3 Results and Discussion

4.3.1 Structural and chemical characterizations

Figure 4-1 presents the XRD patterns for the stoichiometric composition as a function of processing temperature. The best processing temperature for this spinel is 800^OC. This is expected, since this temperature is close to the known optimal processing temperature for these spinels. If the processing temperature is below 800^OC, as for instance 700^OC for the stoichiometric composition, impurities of Mn_2O_3 can be found. If this

composition is heated beyond 800^{O}C, as for instance 900^{O}C, impurities of Mn_3O_4 are observed. These results are in agreement with results from previous reports of processing this material (20).

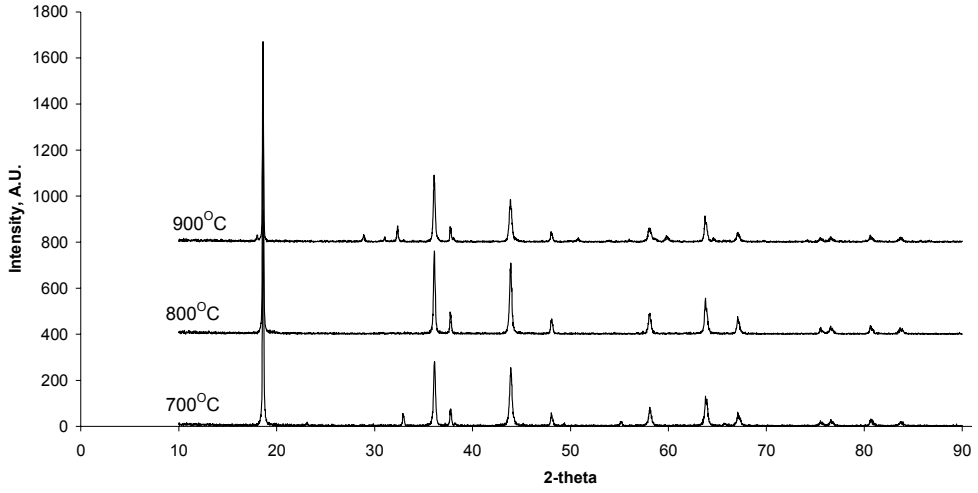

Figure 4-1 XRD spectra of the stoichiometric $LiMn_2O_4$ spinel for varying processing and annealing temperatures

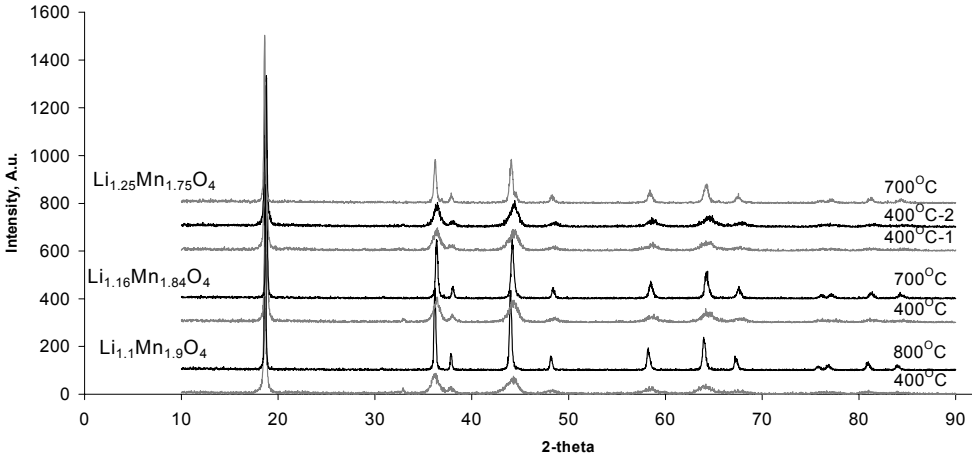

Figure 4-2 XRD spectra of the substituted spinels with increasing Mn substitution and varying processing temperatures

Figure 4-2 presents the XRD patterns of the substituted spinels, where the Mn cations are replaced by Li^+ ions. All as mixed precursors were amorphous and are not shown in this figure. These precursors were first annealed to 400^OC in air that is followed by a second annealing step. For comparison, this figure includes patterns after the first and second annealing steps. After the second annealing step, all patterns show sharp peaks with the exception of the most substituted spinel, i.e., $Li_{1.25}Mn_{1.75}O_4$. For this material, the spinel structure is also detected after the second annealing temperature of 400^OC, but the peaks in the spectra were broad and less intense. When this material was annealed in air to 700^OC impurities of the stoichiometric spinel were detected.

Figure 4-2 also shows that the lattice contracts as more Mn cations are substituted by Li^+ ions. The lattice contraction may be observed by a shift of the spectrum peaks towards higher angles. This is in agreement with other groups that have reported similar phenomena (13,22). From these patterns, the lattice parameter is calculated and tabulated in Table 4-1 in Section 4.3.1.

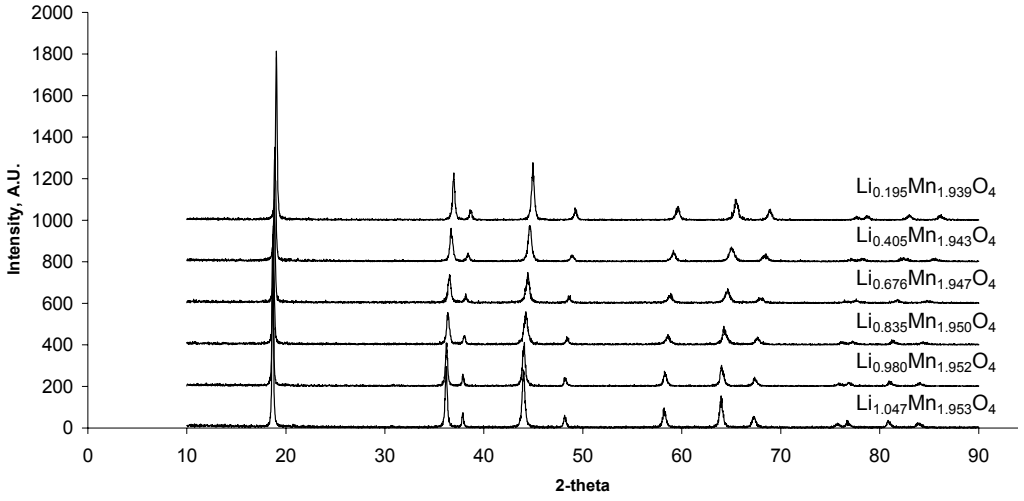

Figure 4-3 XRD spectra of chemically Li extracted spinels

Figure 4-3 presents XRD spectra for the chemically extracted Li^+ ions from the near stoichiometric spinel. As shown first by Hunter, the spinel framework remains through-

out the extraction despite the removal of both Li and Mn cations. Once again, as more Li^+ ions are extracted, the lattice contracts as seen by the shift of the spectra peaks towards higher angles. This is expected since the removal of Li and Mn from the spinel framework reduces the number of ions present in the structure. The lattice parameters are calculated from these patterns and are also presented in Table 4-1.

Results from the Jeager–Vetter titration establish the Mn oxidation state and thus the stoichiometry of the spinel could then be calculated. The calculated stoichiometry for these materials closely resembles the stoichiometry of the intended material as shown in Table 4-1. This point is further illustrated when the average Mn-oxidation state is plotted against the 2(Li/Mn) ratio as shown in Figure 4-4. From this figure, the experimental points of the chemically Li-ion extracted samples, i.e., a Li/Mn ratio less than one, fall closely on the line that represents the calculated Li-ion extraction line. In the case of Mn substitution, these points lie very close to the calculated Li substitution line.

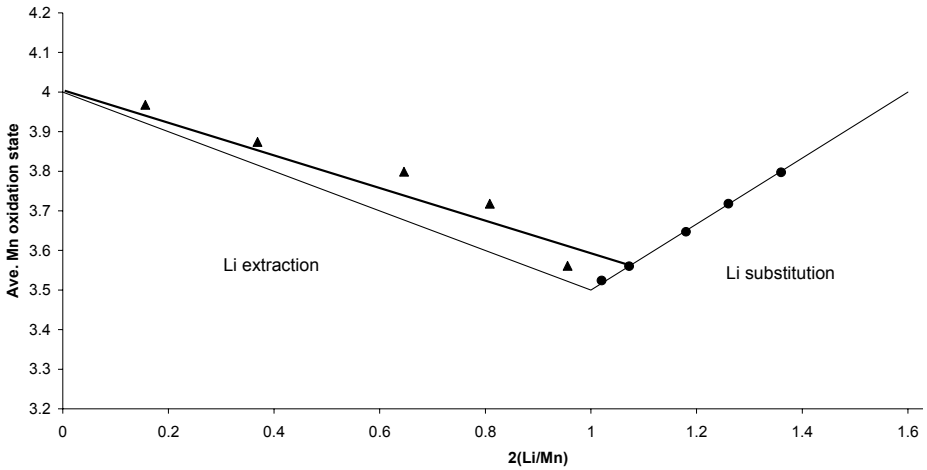

Figure 4-4 Average Mn oxidation state with 2(Li/Mn) ratio

Figure 4-5 presents the lattice parameter or constant, a, versus the 2(Li/Mn) ratio. By using the lattice parameters of the stoichiometric spinels, such as $LiMn_2O_4$, $Li_4Mn_5O_{12}$ and, λ-MnO_2, and assuming that the structure decreases linearly from $LiMn_2O_4$ to λ-MnO_2, a straight line is obtained between the lattice parameter and the 2(Li/Mn) ratio. The reported lattice parameters for these spinels are 8.24 Å for $LiMn_2O_4$ (2(Li/Mn) =1.0), 8.14 Å for $Li_4Mn_5O_{12}$ (2(Li/Mn) =1.6) and, 8.06 Å for the λ-MnO_2 (2(Li/Mn) = 0) spinel (23,24). This figure shows a reasonable linier relationship between the lattice parameter and the expected Li/Mn ration for both extracted and substituted spinels as shown in the solid lines. This figure also shows that the lattice parameter differs between λ-MnO_2 and the $Li_4Mn_5O_{12}$ spinel even though both structures have 100% Mn^{4+} cations. In addition, the final lattice parameter for all of the Li-substituted spinels after treated in acidic solution is 8.06 angstroms. It is interesting to note that all these materials posses approximately the same lattice parameter after the acidic treatment. This includes the highly substituted spinels that are known to exchange Li^+ ions for protons in acidic environments (25).

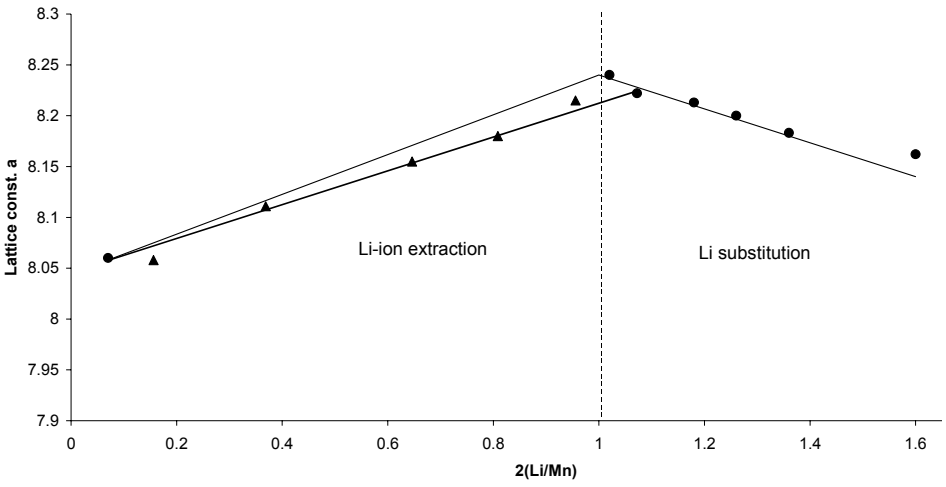

Figure 4-5 Lattice parameter vs. 2(Li/Mn) ratio

Table 4-1 Some physical results found in the lithium manganates

δ spinel samples	Preparation		a (Å)	Z_{Mn}		μ_{eff}	Θ
	1st heating	2nd heating		Exp.	Calc.		
$LiMn_2O_4$	700°C-24hrs	700°C-24hrs	Impurities were found				
$LiMn_2O_4$	900°C-24hrs	900°C-24hrs	Impurities were found				
$LiMn_2O_4$	800°C-24hrs	800°C-24hrs	8.24	3.52(4)	3.500	4.45(1)	-317
$Li_{1.1}Mn_{1.9}O_4$	400°C-24hrs	800°C-24hrs	8.23	3.64(7)	3.632	4.36(9)	-301
$Li_{1.16}Mn_{1.84}O_4$	400°C-24hrs	700°C-24hrs	8.19	3.71(8)	3.717	4.16(2)	-196
$Li_{1.25}Mn_{1.75}O_4$	400°C-24hrs	400°C-24hrs	8.16	3.79(7)	3.857	3.77(2)	-72
Chemical Li-extraction	Preparation		a (Å)	Z_{Mn}		μ_{eff}	Θ
				Exp.	Calc.		
$Li_{1.047}Mn_{1.953}O_4$	775°C 30hrs		8.22	3.56(0)	3.560	4.30(0)	-252
$Li_{0.980}Mn_{1.952}O_4$	0.5ml/g 1M H_2SO_4		8.21	3.56(1)	3.597	4.50(8)	-301
$Li_{0.835}Mn_{1.950}O_4$	1.5ml/g 1M H_2SO_4		8.18	3.71(8)	3.675	4.16(5)	-108
$Li_{0.676}Mn_{1.947}O_4$	2.5ml/g 1M H_2SO_4		8.13	3.79(9)	3.761	4.02(8)	-101
$Li_{0.405}Mn_{1.943}O_4$	4.0ml/g 1M H_2SO_4		8.11	3.87(4)	3.909	3.79(1)	-66
$Li_{0.198}Mn_{1.939}O_4$	5.0ml/g 1M H_2SO_4		8.06	3.96(8)	4.000	3.87(2)	-133

4.3.2 Magnetic characterization

The inverse magnetic susceptibility as a function of temperature in the range of 294-500K for the substituted and chemically delithiated $LiMn_2O_4$ is presented in Figures 4-6 and 4-7, respectively. These plots follow the Curie-Weiss law,

$$\frac{1}{x_m} = \frac{(T - \Theta)}{C_m} \tag{4.1}$$

where, χ_m is the molar magnetic susceptibility, T the temperature in K, Θ the Weiss temperature, and C_m the molar Curie constant. From these plots, the calculation of the Curie constant, C_m, which is the inverse of the slope, and Θ, which is the intercept of the curve, was performed.

In Figures 4-6 and 4-7 the slope of these curves progressively become steeper as more Mn is substituted or more Li is chemically extracted from the spinels. It is also observed that the curves overlap as more Li is extracted. This overlap affects the Weiss temperature that is presented in Table 4-1.

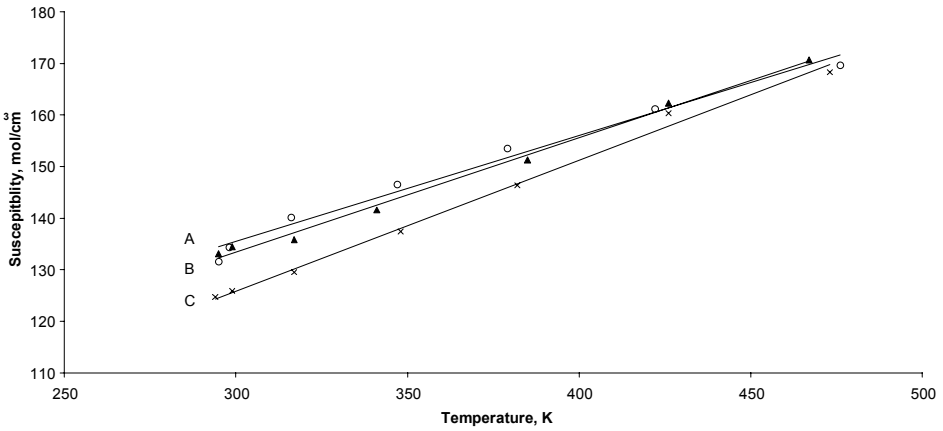

Figure 4-6 Magnetic susceptibility as a function of temperature for x is A:0.01, B:0.11, C:0.16

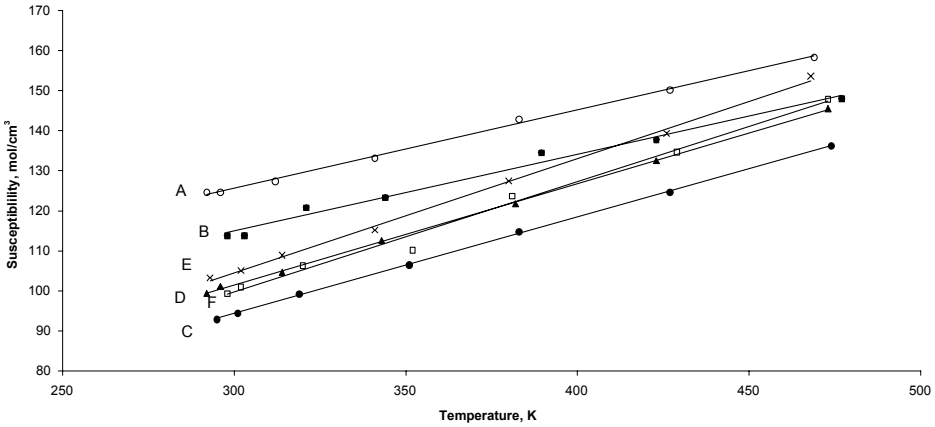

Figure 4-7 Magnetic susceptibility with temperature for the chemically delithiated spinels for x is A: 0.04(7), B: 0.98(0), C: 0.83(5), D: 0.67(6), E: 0.40(5), F: 0.19(8)

Figure 4-8 presents the effective magnetic moment, μ_{eff}/μ_B , as a function of the Mn oxidation state, Z_{Mn}. The effective magnetic moment is calculated from the molar Curie constant C_m from Equation 4.1 and is shown below in Equation 4.2.

$$\frac{\mu_{eff}}{\mu_B} = \left(\frac{3kC_m}{N_A \mu_B^2} \right)^{\frac{1}{2}} \tag{4.2}$$

In this equation, k is Boltzman's constant, N_A Avogadro's number, and μ_B the Bohr magneton.

Figure 4-8 shows that as the average Mn oxidation state of the spinels increase from 3.5-4.0 either by Li-ion extraction or by Li-substitution, all Mn^{3+} cations are in a high-spin electronic configuration. If spin-only considerations were used, these points clearly lay close to the theoretical line where the theoretical effective moment μ_{eff} =4.38 μ_B for high-spin Mn^{3+} cations and μ_{eff} =3.87 μ_B for Mn^{4+}. These results are consistent for both Li-substituted and Li-ion extracted spinels up to an average Mn oxidation state of 3.9.

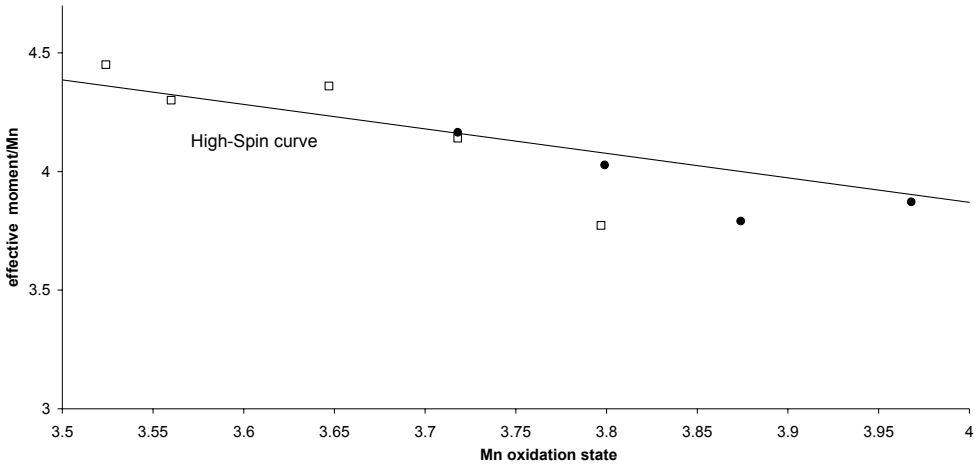

Figure 4-8 The effective magnetic moment as a function of the average Mn oxidation state

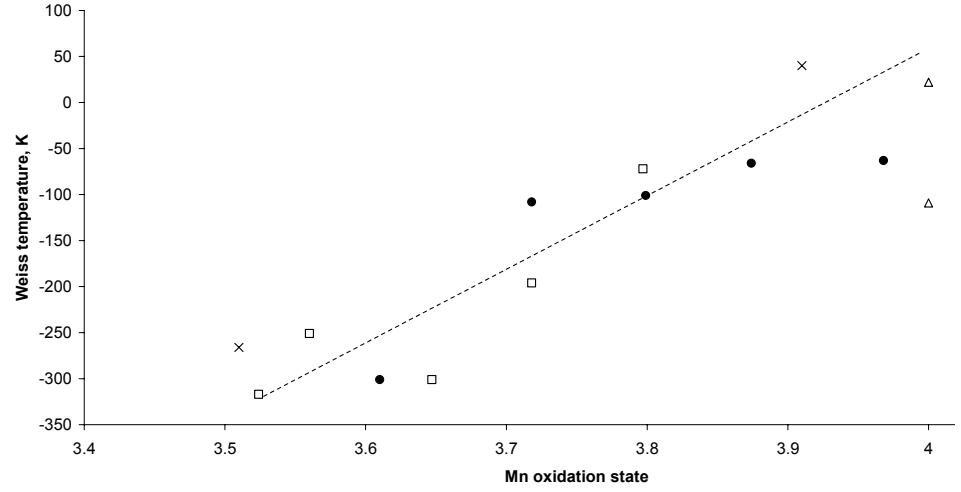

Figure 4-9 Weiss temperature as a function of the average Mn oxidation state where; □ is Mn substitution, ● is Li extracted, ∆ is Ariza ref. (24) $Li_4Mn_5O_{12}$ and protonated $Li_{4-x}H_xMn_5O_{12}$ and, x is Masquelier ref. (12) Mn substitution

Figures 4-9 presents the Weiss temperature for the spinels as a function of the average Mn valence. All plotted data are listed in Table 4-1. Included in this figure is part of the work from Masquelier et al.(13), and Ariza et al.(24). If the Weiss temperature is plotted against the average Mn oxidation state, a rough trend is observed. This implies that all samples behave in a similar manner.

However, if the same data is plotted against the lattice parameter, as presented in Figure 4-10, two distinct trends are present. One distinct trend shows a steady increase in the Weiss temperature as the lattice parameter decreases from 8.24 Å to 8.14 Å that coincides with the increasing values of the Mn valence state from 3.52 to 4.00. The near stoichiometric spinel material with a lattice parameter of 8.24 Å and an average Mn oxidation state of 3.52 possesses a rather strong negative Weiss value (θ =-250K) that indicates empirically strong antiferromagnetic interactions of the octahedrally positioned Mn cations. This value is in good agreement with reports from similar materials (26-29). This trend can be extended to the lattice parameter of 8.14 Å and a Mn oxidation state close to 4.00 by including the data from other previous studies (13,24).

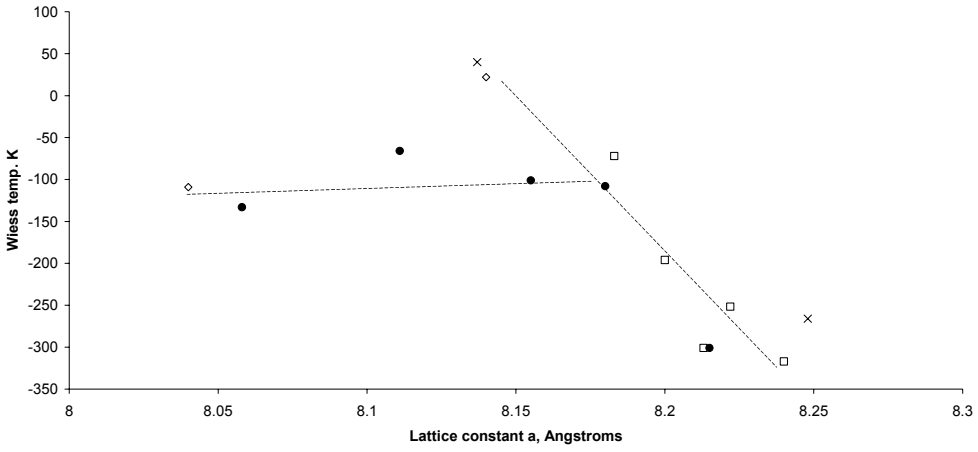

Figure 4-10 Weiss temperature as a function of lattice parameter where; □ is Mn substitution, ● is Li extracted, ◊ is Ariza $Li_4Mn_5O_{12}$ and protonated $Li_{4-x}H_xMn_5O_{12}$ and, x is Masquelier Mn substitution

The other distinct trend presented in Figure 4-10 originates primarily from the chemically Li-ion extraction samples. In this trend, the Weiss temperature is relatively constant around the value of –100K. This trend is present for the average Mn valence in the range of 3.7 to 3.9. This value is also in good agreement with other previously reported values (Θ=~-70K) for the λ-MnO_2 material (14,17). The broken lines in this figure are used only to guide the reader.

Attempts to produce the $Li_4Mn_5O_{12}$ spinel have failed in this study but recently other groups have reported positive Weiss temperature values, that empirically indicate weak ferromagnetic interactions between the Mn cations in this material (13,24,29). Moreover, when one of these groups treated this spinel material with acid, the Weiss temperature changed from slightly positive to slightly negative. The decrease in the lattice parameter for this material was due to an ion exchange between protons with Li^+ ions. The change of the Weiss temperature from a slightly positive to a slightly negative values was due to the decrease in the lattice parameter. (24). In general, the Weiss temperature values that were reported fit well with the trends of the work presented here.

4.3.3 Characterization of the near stoichiometric $LiMn_2O_4$ spinel

To determine the quality of the near stoichiometric material, further characterization of this spinel has been performed. It has been known that the stoichiometric spinel changes from a cubic to an orthogonal configuration at slightly below room temperature (9,30). This structural change can be detected using differential scanning calorimetry (DSC). This analysis has been performed on the present stoichiometric spinel in the temperature range between –75 to 100^{O}C at 5^{O}C/min. and is presented in Figure 4-11.

From this figure, an endothermic peak at 6.9^{O}C is observed when the sample is cooled from room temperature to -75^{o}C. This transition is reversible when this sample was heated from -75^{o}C to 100^{o}C. An exothermic peak is observed at a temperature of 30.5^{O}C. These transition temperatures agree with the structural transition from cubic to the orthogonal phase found in literature (8).

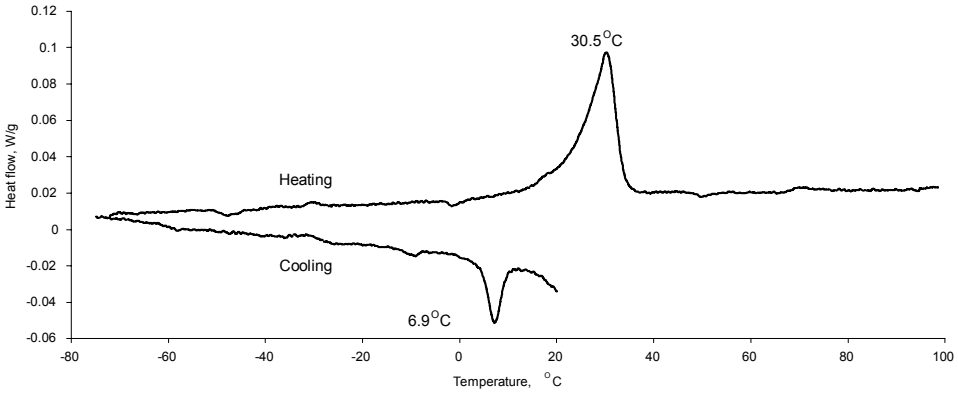

Figure 4-11 DSC traces for $LiMn_2O_4$ upon cooling and heating

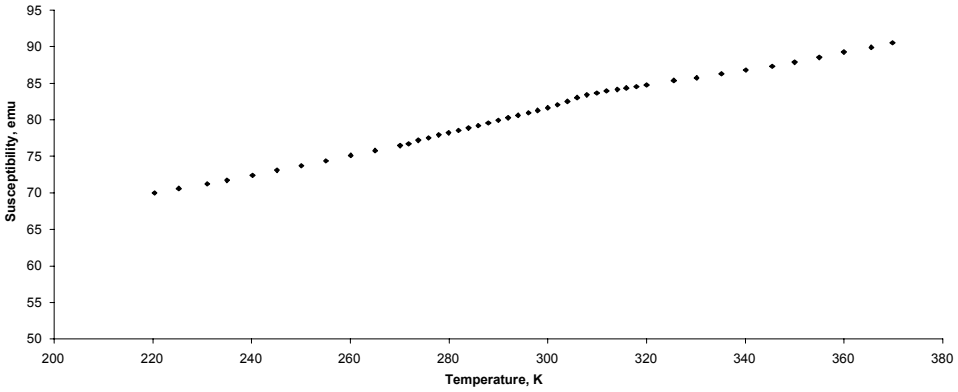

Figure 4-12 Magnetic susceptibility for $LiMn_2O_4$ as a function of temperature when heated from 180 to 375K

With the use of a SQUID magnet at 10^4 Gausians, the magnetic transition between the cubic and orthogonal structures can also be observed. The structural transition is approximately 308 K (35^OC) when heated from 185 K to 375 K as presented in Figure 4-12. The temperature corresponding to the structural change is in good agreement with the present DSC findings as well as with data reported by Shimahawa et al. (28). The

magnetic anomaly corresponds to the order/disorder of charge of the Mn^{3+}cations (16). The charge ordering when the material is cooled gives rise to the cooperative Jahn-Teller distortion of the spinel to form an orthogonal structure. This effect is reversible when the material is heated and a charge disorder occurs. Thus, a cubic spinel is the resulting structure.

The wide variation in the peak transition temperatures between heating and cooling this sample is probably due to the relatively fast scan rate that was applied in the DSC measurement. Because this effect occurs in a very narrow compositional range, the attempt to produce a near stoichiometric spinel in our study seems successful.

4.3.4 The Mn^{3+} electronic spin configuration

The Mn^{3+} cation contains four electrons in the 3d-band. When this cation occupies an octahedral site, the d-band splits into two energy levels due to the octahedral crystal field. The lower energy level is referred to as the t_{2g} level. This level contains the three orbitals that may contain up to 6 electrons. Since these orbitals lie in between the oxygen 2p orbitals, these orbitals are also referred to as bonding orbitals. The higher energy level in the d-band is referred to as e_g level. This level contains 2 orbitals where up to four electrons may be placed. These orbitals are at a higher energy level because they face directly to the oxygen 2p orbitals on the axes. These orbitals are referred to as anti-bonding orbitals (31).

When placing electrons into energy levels, Hund's rule is usually applied. In essence, this rule places each electron in each energy level beginning with the lowest energy. Once all energy levels are half-filled, a second electron is placed in the half-filled energy level beginning with the lowest energy level. The reasoning behind this rule is that the spin-paring energy is greater than the crystal field energy (31).

In the case of the Mn^{3+} cation, four electrons are present in which there are two possible electron configurations. These configurations are referred to as either high or low-spin configurations. If Hund's rule is applied, then all of the t_{2g} energy levels and one of the e_g energy levels is half-filled with an electron. This electron configuration is

called a high-spin configuration. In a low-spin configuration, all four electrons occupy the t_{2g} energy levels. This results in one of the t_{2g} energy levels to be full while the other two energy levels to be half-full. This configuration does not follow Hund's rule.

In the case of the stoichiometric spinel $LiMn_2O_4$, it has been suggested that approximately 20% of the Mn^{3+} cations are in a low-spin configuration (32). This was found experimentally by Endres et al. (29) and used by Chung et al. as a parameter for calculating structures of substituted spinels (33). The present work contradicts all of these findings as the magnetic moment for all present materials lies near the theoretical line for a high-spin configuration. In support of the present findings, one can argue that the crystal field energy for the high-spin configuration is lower than the spin-paring energy, which follows Hund's rule. By referring to the Tanabe-Sugano diagrams, the energy of the crystal field required to change the spin configuration of Mn^{3+} cations from high to low-spin is approximately 3.4 eV (34). In other words, when the band gap between the t_{2g} and e_g levels is greater than 3.4 eV, the spin paring energy of an electron is less than placing electron at the e_g energy level. Thus, and a low-spin configuration occurs.

Recently, the crystal field energy has been measured experimentally by using optical absorption of thin films of $LiMn_2O_4$ and λ-MnO_2 (35). The results indicate an energy gap between the t_{2g} and e_g levels of 1.91eV for the Mn^{4+} cations in the λ-MnO_2 spinel. This energy is significantly smaller than the required energy for the electron to be in a low-spin state. Therefore, the probability that any of the Mn^{3+} cations is in a low-spin configuration is small.

In regards to the reporte of Endres et al. (29), it was found that a normalization was not used. Without normalizing, the value of the magnetic moment is 6.05 Bohr magnetons. This value is larger than the theoretical value given for either high or low-spin electron configuration of the Mn^{3+} cations in $LiMn_2O_4$. Nevertheless, this value leads to the interpretation that 20% of Mn^{3+} cations in $LiMn_2O_4$ are in a low-spin state. By normalizing the Currie constant per Mn mol ratio of the empirical formula, the effective moment is calculated to be 4.27 Bohr magnetons/Mn. This value is much closer to the theoretical value of 4.38 Bohr magnetons/Mn that corresponds to a high-spin electron configuration. Thus, by normalizing the data from this report, similar results were calculated as were found in the present work.

4.3.5 The relation between ion interactions and magnetic interactions

It is known that two types of interactions exist for the octahedrally coordinated cations. The first type is direct interaction while the second type is 90° super exchange between an oxide anion (31,36). For the high-spin Mn^{3+} ($t_{2g}3\ e_g1$) and Mn^{4+} ($t_{2g}3\ e_g0$) cations, the t_{2g} orbitals are half filled. Since these cations share an octahedral-site edge, the electrons from these cations could interact directly. This effect causes antiferromagnetic interactions. In addition, since the spinel is cubic, the lattice parameter has an effect on these interactions due to the proximity of the Mn cations. Therefore, as the lattice constant decreases, the Mn-Mn distance also decreases and the strength of antiferromagnetic interactions increases resulting in a stronger negative value of the Weiss temperature. The second type involves the anion, in this case the oxide anion, where the 90° Mn-O-Mn Goodenough-Kanamori superexchange occurs. This exchange takes place via the O 2p orbital that couples with the e_g orbital of one Mn cation and the t_{2g} orbital of the adjacent Mn cation. High-spin Mn^{3+} cations that possess a half-filled e_g orbital cause antiferromagnetic interactions between other Mn^{3+}, or Mn^{4+} cations that posses half-filled t_{2g} orbitals. This is opposed to the Mn^{4+} cations that contain no electrons in the e_g orbital. The half-filled t_{2g} orbital of one Mn^{4+} cation couples with the empty e_g orbital from the next Mn^{4+} cation. This coupling causes ferromagnetic interactions between the cations that leads to a is positive Weiss temperature.

From previous studies, it is observed that the Weiss temperature increases as a function of the average Mn oxidation state. This implies a weakening of the antiferromagnetic interactions. The model for this behaviour is that the ferromagnetic 90° Mn^{4+}-O-Mn^{4+} super-exchange interactions gradually dominate the antiferromagnetic high-spin Mn^{3+}-Mn^{3+}, Mn^{3+}-Mn^{4+}, Mn^{4+}-Mn^{4+} and Mn^{3+}-O-Mn^{4+} interactions (13). This model seems to fit with our results when the average Mn valence for both types of lithium manganate spinels is in the range of 3.5 to 3.7. In Figure 4-9, a single trend is observed where the Weiss temperature steadily increases from strongly negative to less negative for both Li-extracted and Li-substituted spinels. This trend coincides with the increase of the average Mn valence for Li-extracted and Li-substituted spinels from 3.5 to 3.7. A summary of Mn interactions with the magnetic interactions is presented in Table 4 -2.

Table 4-2 Summary of ion interactions with magnetic interactions

Ion interactions	Magnetic interactions
Mn^{3+}-Mn^{3+}	antiferromagnetic
Mn^{3+}-Mn^{4+}	antiferromagnetic
Mn^{4+}-Mn^{4+}	antiferromagnetic (very weak)
90^{O} Mn^{3+}-O-Mn^{4+}	antiferromagnetic
90^{O} Mn^{4+}-O-Mn^{4+}	ferromagnetic

Although the type of magnetic interactions is important, another factor must account for the second trend presented in Figure 4-9 where the Weiss temperature is relatively constant. The constant Weiss temperature applies only to the Li-ion extracted spinels where the average Mn oxidation state is between 3.7 to 3.9. The second factor may come from the work of Blasse in which it was shown that direct Mn^{4+}-Mn^{4+} antiferromagnetic interactions are by nature very weak (27). Thus, the proximity of the Mn cations to each other is significant.

When the average Mn oxidation state is beyond 3.7 for both lithium manganate spinels, the population of the Mn^{4+} cations increases. However, two distinct trends are observed. In the case of Li-ion extraction, the direct Mn^{4+}-Mn^{4+} interactions dominate the Mn^{3+}-Mn^{3+} and Mn^{3+}-Mn^{4+} interactions. Their influence becomes stronger as the lattice constant decreases. This provides weak antiferromagnetic interactions between the cations and the Weiss temperature remains negative. In the case of Li-substituted spinels, the population of Mn^{4+} cations also increases as substitution proceeds. In addition, the lattice does not contract as much as the Li-ion extracted spinels. These two effects cause the direct Mn-Mn interactions to be either more weak or nonexistent. The magnetic interactions may then apply to the 90° Mn^{4+}-O-Mn^{4+} exchange mechanism. These interactions are ferromagnetic as empirically indicated by the increasing Weiss temperature. However as shown by Ariza et al., if the lattice of the most Li-substituted spinel, $Li_4Mn_5O_{12}$, shrinks as a result of ion exchange with protons, the Mn^{4+}-Mn^{4+} interactions may once again be established. This causes the material to possess antiferromagnetic interactions and a slightly negative Weiss temperature (24).

The electrical measurements of these spinels are concordant with the present findings. Recently, electrical measurements were performed on Li-ion extracted spinels by Molenda et al. (8). Their results have shown that the activation energy for electrical conduction decreases rather linearly as a function of Li-extraction up to $Li_{0.5}Mn_2O_4$ or a Mn oxidation state of 3.75. Beyond this point, i.e., from $Li_{0.5}Mn_2O_4$ to λ-MnO_2 , the activation energy is relatively constant. The electrical measurements show, at least in the case of the Li-ion extracted spinels, that the present trend for magnetic measurements coincides with the trend of electrical measurements.

4.4 Conclusions

Magnetic characterizations of $LiMn_2O_4$ as a function of Li-ion extraction by chemical means have been performed. Through XRD and Jeager-Vetter titration analysis, the lattice parameter linearly decreases as the oxidation state increases. In addition, the optimal processing temperature for the near stoichiometric spinel was found to be 800^{o}C. In the case of Mn-substituted spinels, the processing temperature decreases as substitution increases.

DSC and magnetic measurements using a SQUID magnet have further characterized the quality of the near stoichiometric $LiMn_2O_4$ spinel. From the DSC analysis, endothermic and exothermic reactions occur when the material is cooled and heated. From the SQUID measurements, a magnetic anomaly is observed when heated from 220 K that corresponds to the peak temperature of the exothermic peak of the DSC. This is interpreted as a reversible structural transformation from cubic to an orthogonal structure due to charge ordering of $LiMn_2O_4$ as the temperature decreases.

From magnetic measurements, it was found that all Mn^{3+} cations are in a high-spin configuration. The effective magnetic moment lies near the theoretical value for all measured spinels. This finding is supported by other reports of the same material as well as from theoretical aspects.

Ion interactions indicate that the original spinel begins with a strong negative Weiss temperature, that indicates antiferromagnetic behaviour. This gradually changes and becomes more ferromagnetic as the average Mn oxidation state increases. Two distinct

trends are observed between the Weiss temperature and the lattice parameter for the two types of spinels. In the case of Li substitution, the Weiss temperature steadily increases with increasing Li substitution and decreasing lattice parameter. In the case of Li-ion extraction, the Weiss temperature also steadily increases as Li^+ ions are extracted from the spinel up to a Mn oxidation state of 3.7 and a lattice parameter of 8.16 Å. Beyond this point, the Weiss temperature is relatively constant at an average Mn oxidation state of 3.97 with a lattice parameter of 8.05 Å. A combination of ionic interactions and proximity of the Mn cations influences the antiferromagnetic/ferromagnetic behaviour.

4.5 References

1. Ohzuku, T.; Kitagawa, M.; Hirai, T. *J. Electrochem. Soc.* **1990,** *137*(3), 769-775.

2. Hunter, J. C. *United States Patent* **1982,** *4,312,930*.

3. Hunter, J. C. *J.Solid State Chem.* **1981,** *39* 142-147.

4. Feng, Q.; Kanoh, H.; Ooi, K. *J. Mater. Chem.* **1999,** *9*(2), 319-333.

5. Berg, H.; Kelder, E. M.; Thomas, J. O. *J. Mater. Chem.* **1999,** *9*(2), 427-429.

6. Thackeray, M. M.; de Picciotto, L. A.; de Kock, A.; Johnson, P. J.; Nicholas, V. A.; Adendorf, K. T. *J. Power Sources* **1987,** *21* 1-8.

7. Johnson, C. S.; Li, N.; Vaughey, J. T.; Hackney, S. A.; Thackeray, M. M. *Electrochem. Commun.* **2005,**(7), 528.

8. Molenda, J.; Swierczek, K.; Molenda, M.; Marzec, J. *Solid State Ionics* **2000,** *135*(1-4), 53-59.

9. Marzec, J.; Swierczek, K.; Przewoznik, J.; Molenda, J.; Simon, D. R.; Kelder, E. M.; Schoonman, J. *Solid State Ionics* **2002,** *146*(3-4), 225-237.

10. Massarotti, V.; Capsoni, D.; Bini, M.; Chiodelli, G.; Azzoni, C. B.; Mozzati, M. C.; Paleari, A. *J. Solid State Chem.* **1997,** *131*(1), 94-100.

11. Tabuchi, M.; Masquelier, C.; Kobayashi, H.; Kanno, R.; Kobayashi, Y.; Akai, T.; Maki, Y.; Kageyama, H.; Nakamura, O. *J. Power Sources* **1997,** *68*(2), 623-628.

12. Masquelier, C.; Tabuchi, M.; Ado, K.; Kanno, R.; Kobayashi, Y.; Maki, Y.; Nakamura, O.; Goodenough, J. B. *J. Solid State Chem.* **1996,** *123*(2), 255-266.

13. Masquelier, C.; Tabuchi, M.; Ado, K.; Kanno, R.; Kobayashi, Y.; Maki, Y.; Nakamura, O.; Goodenough, J. B. *J. Solid State Chem.* **1996,** *123*(2), 255-266.

14. Goodenough, J. B.; Manthiram, A.; Jones, A. C. W. P.; Strobel, P. *MRS Symposium Proceedings* **1989,**(135), 391.

15. Greedan, J. E.; Raju, N. P.; Wills, A. S.; Morin, C.; Shaw, S. M.; Reimers, J. N. *Chem. Mater.* **1998,** *10*(10), 3058-3067.

16. Wills, A. S.; Raju, N. P.; Greedan, J. E. *Chem. Mater.* **1999,** *11*(6), 1510-1518.

17. Jang, Y.-I.; Huang, B.; Chou, F. C.; Sadoway, D. R.; Chiang, Y. M. *J. Appl. Phys.* **2000,** *87*(10), 7382.

18. Tabuchi, M.; Masquelier, C.; Kobayashi, H.; Kanno, R.; Kobayashi, Y.; Akai, T.; Maki, Y.; Kageyama, H.; Nakamura, O. *J. Power Sources* **1997,** *68*(2), 623-628.

19. Kelder, E. M.; Ooms, F. J. B.; Perego, R.; Schoonman, J. *J. Power Sources* **2001,** *97-8* 433-436.

20. Gao, Y.; Dahn, J. R. *J. Electrochem. Soc.* **1996,** *143*(1), 100-114.

21. Rousse, G.; Masquelier, C.; Rodriguez-Carvajal, J.; Elkaim, E.; Lauriat, J. P.; Martinez, J. L. *Chem. Mater.* **1999,** *11*(12), 3629-3635.

22. Pickup, D. M.; Simon, D.; Fooken, M.; Krampitz, H.; van Eck, E. R. H.; Kelder, E. M. *J. Mater. Chem.* **2003,** *13*(4), 963-968.

23. Ammundsen, B.; Roziere, J.; Islam, M. S. *J. Phys. Chem. B* **1997,** *101*(41), 8156-8163.

24. Ariza Maria J.; Jones, D. J.; Roziere, J.; Lord, J. S. *J. Phys. Chem. Solids* **2004,** *65* 597.

25. Ammundsen, B.; Jones, D. J.; Roziere, J.; Berg, H.; Tellgren, R.; Thomas, J. O. *Chem. Mater.* **1998,** *10*(6), 1680-1687.

26. Schoonman, J.; Tuller, H. L.; Kelder, E. M. *J. Power Sources* **1999,** *81-82* 44.

27. Blasse, G. *Philips Research Reports* **1963,** *18* 400-404.

28. Shimakawa, Y.; Numata, T.; Tabuchi, J. *J. Solid State Chem.* **1997,** *131*(1), 138-143.

29. Endres, P.; Fuchs, B.; Kemmler-Sack, S.; Brandt, K.; Faust-Becker, G.; Praas, H. W. *Solid State Ionics* **1996,** *89* 221.

30. Hayakawa, H.; Takada, T.; Enoki, H.; Akiba, E. *J. Mater. Sci. Letters* **1998,** *17*(10), 811-812.

31. Goodenough, J. B. *Magnetism and the Chemical Bond;* John Wiley and Sons: 1963; Vol. 1.

32. Schutte, L.; Colsmann, G.; Reuter, B. *J. Solid State Chem.* **1979,** *27* 227.

33. Chung, H. T.; Myung, S. T.; Cho, T. H.; Son, J. T. *J. Power Sources* **2001,** *97-8* 454-457.

34. Ballhausen *Introduction to Ligand Field Theory;* McGraw-Hill: 1962.

35. Kushida, K.; Kuriyama, K. *App. Phys. Letters* **2000,** *77* (25), 4154.

36. Kanamori, J. *J. Phys. Chem. Solids* **1959,** *10* 87.

5

Open-circuit potential measurement of $LiMn_2O_4$ in aqueous solutions

Abstract

The open-circuit potential of a Pt electrode in an acidic solution that contains $LiMn_2O_4$ particles has yielded a similar potential curve to that of an electrochemical cell as a function of Li-ion extraction. This is due to the fact that the corrosion potential of $LiMn_2O_4$ is the same when comparing the potential for an electrochemical cell. Additionally, a linear relationship with a slope of –0.1178 V was found between the open-circuit potential of the Pt electrode and the pH in solution. This relationship proves the relationship between pH of a solution that contains $LiMn_2O_4$ particles and the Li-ion capacity of $LiMn_2O_4$.

5.1 Introduction

Through the work of Hunter (1), it has been shown that Li^+ ions may be chemically extracted from $LiMn_2O_4$ when in contact with acidic aqueous solutions (2). The resulting material is a spinel material of manganese oxide that was named λ-MnO_2. Hunter (1,2) proposed that a disproportionation reaction of the Mn^{3+} cations is the redox mechanism behind this extraction. This reaction involves the oxidation and reduction of Mn^{3+} cations to form Mn^{4+} and Mn^{2+} cations, respectively. This is known as Hunter's Equation that is given below (1),

$$2LiMn_2O_{4(s)} + 4H^+_{(aq)} \rightarrow 3(\lambda - MnO_2)_{(s)} + 2Li^+_{(aq)} + Mn^{2+}_{(aq)} + 2H_2O_{(aq)} \quad (5.1)$$

The products of Equation (5.1) include Mn^{4+} cations that remain in the solid, while Li^+ and Mn^{2+} cations go into solution. The acid is neutralized by the removal of oxygen from the $LiMn_2O_4$ spinel.

In later reports by Ooi et al., λ-MnO_2 could be reduced back to $LiMn_2O_4$ when in contact with a basic lithium salt solution such as LiOH. This reaction involves the reduction of the Mn^{4+} cations and the oxidation of oxide ions that in turn forms a gas as presented in Equation (5.2) for n equal to one (3,4).

$$Mn^{4+}_2O_{4(s)} + nLiOH_{(aq)} \rightarrow Li_n[Mn^{3+}_n Mn^{4+}_{2-n}]O_{4(s)} + \frac{n}{2}H_2O_{(aq)} + \frac{n}{4}O_{2(g)} \quad (5.2)$$

The same group has also performed extensive studies on the response of $LiMn_2O_4$ and λ-MnO_2 with different solutions. These studies revealed that λ-MnO_2 exhibits a Nernst type response to the concentration of Li^+ ions in solution and derived an expression for this response (3,5).

$$E = Const. + \mu^o_{Li^+} + (RT/F)\ln a_{Li^+} \quad (5.3)$$

where the terms E, R, T, F, and $\mu^o_{Li^+}$ are the electrode potential, the gas constant, temperature, Faraday's constant, and the standard chemical potential of Li^+ ion, respectively. In the natural log term, a_{Li^+} is the activity of Li ion.

Furthermore, by using a λ-MnO_2 electrode, Ooi et al. showed that this electrode exhibited a linear response to the change in pH of the solution. In the acidic region of a solution within pH values of 3 to 5, a large negative slope of –112.4 mV was observed. This slope changed to a near Nernstian response of –61.1 mV between pH values of 5 to 9.5 (5).

Some groups have reported the open-circuit potential of a Pt electrode in a solution with the solids present. Caudel et al. have shown that a Nernstian response can also be found by using this scheme. These authors have shown that a Pt electrode measures a linear open-circuit potential response as a function of the pH of a solution that contained manganese oxide particles (6).

Other potentiometric measurements were directed towards the pH of the solution that contained solid particles. Kelder et al. have measured the pH of a solution that contained $LiMn_2O_4$ particles through the potential response of a glass electrode (7). It was observed that the shape of the titration curve (i.e., pH of the solution versus volume of acid introduced into the solution) is similar to that of the potential curve of an electrochemical cell if Li^+ ions are extracted from $LiMn_2O_4$. From this comparison, Kelder et al. claimed that the capacity and rate capability of the electrode could be predicted in a relatively short period of time.

Despite the similarity in the shape of the two potential curves, a relation between these curves has not been fully established by Kelder et al. This chapter measures the pH and the open-circuit potential of a solution that contains $LiMn_2O_4$ particles. From these measurements, the relation between the pH and the potential curves of the solution that contain $LiMn_2O_4$ particles to the potential of Li-ion extraction from $LiMn_2O_4$ in an electrochemical cell is explained.

5.2 Theoretical aspects

The aim in this section is to derive the electric potential of an electrochemical cell and the Nernst potential of Hunter's equation as a function of Li-ion extraction from $LiMn_2O_4$ by electrochemical and chemical means, respectively.

5.2.1 The electric potential as a function of Li-ion extraction from $LiMn_2O_4$ using an electrochemical cell

The half-cell reactions for the electrochemical Li^+-ion extraction from $LiMn_2O_4$ using Li metal as a counter and reference electrode are,

$$LiMn_2O_4 \rightarrow Li_{(1-x)}Mn_2O_4 + xLi^+ + xe^- \tag{5.4}$$

$$xLi^+ + xe^- \rightarrow xLi_{Metal} \tag{5.5}$$

Equation (5.4) refers to the anodic reaction or oxidation of $LiMn_2O_4$ as a function of x Li^+ ions extracted from $Li_{(1-x)}Mn_2O_4$ for $0 \leq x \leq 1$. Equation (5.5) refers to the cathodic reaction or reduction of lithium ions in an electrochemical cell. The potentials of these half-cell reactions are,

$$-E_{an}^{cell(x)}F = \mu_{LiMn_2O_4}^0 - \mu_{Li_{(1-x)}Mn_2O_4} - x\left(\mu_{Li^+}^o + RT\ln a_{Li^+}\right) \tag{5.6}$$

$$-E_{cat}^{cell(x)}F = \mu_{Li}^o - x\left(\mu_{Li^+}^o + RT\ln a_{Li^+}\right) \tag{5.7}$$

where E is the potential of the anode and cathode half-cell reaction, respectively, as a function of x Li^+ ions, F is Faraday's constant, μ_{Li}^o and $\mu_{Li^+}^o$ is the standard chemical

potential of Li metal and Li^+ ion, respectively, $\mu^o_{LiMn_2O_4}$ is the standard chemical potential of $LiMn_2O_4$, and $\mu_{Li_{(1-x)}Mn_2O_4}$ is the chemical potential of $Li_{(1-x)}Mn_2O_4$ as a function of x Li^+ ions for $0 \leq x \leq 1$. The total cell potential as a function of x Li^+ ions is the difference between each half-cell electric potentials of the cathode and the anode. Thus,

$$E_{Cell(x)} = E_{cat}^{cell(x)} - E_{an}^{cell(x)} \tag{5.8}$$

In this cell, the electric potential of the cathodic half-cell reaction, i.e. the reduction of Li metal, is constant or,

$$E_{cat}^{cell(x)} = const. \tag{5.9}$$

By substituting this constant into Equation (5.8),

$$E_{Cell(x)} - const. = -E_{an}^{cell(x)} \tag{5.10}$$

Thus, the change in the electric potential of the total cell is solely due to the anodic half-cell reaction.

5.2.2 The electric potential based on Hunter's equation

The reaction of Hunter's equation, Equation (5.1), may also be written as a function of x Li^+ ions extracted from $LiMn_2O_4$ to produce $Li_{(1-x)}Mn_2O_4$ by chemical means for $0 \leq x \leq 1$. The half-cell reactions are as follows,

$$LiMn_2O_4 \rightarrow Li_{(1-x)}Mn_2O_4 + xLi^+ + xe^- \tag{5.11}$$

$$\frac{1+x}{2} LiMn_2O_4 + xe^- + 4xH^+ \rightarrow \frac{1}{2} Li_{(1-x)}Mn_2O_4 + xMn^{2+} + xLi^+ + 2xH_2O \tag{5.12}$$

where Equations (5.11) and (5.12) are the anodic and cathodic reactions, respectively. Equation (5.11) expresses the oxidation of the Mn^{3+} cations in $LiMn_2O_4$ to Mn^{4+} that remain as a solid. Equation (5.12) presents the reduction of Mn^{3+} in $LiMn_2O_4$ to Mn^{2+} that is in solution. Additionally, the neutralization of the acid in solution also occurs in the cathodic reaction and the release of Li^+ ions from $LiMn_2O_4$ occurs in both equations. The total reaction is

$$\frac{3+x}{2} LiMn_2O_{4(s)} + 4xH^+_{(aq)} \rightarrow \frac{3}{2} Li_{(1-x)}Mn_2O_{4(s)} + 2xLi^+_{(aq)} + xMn^{2+}_{(aq)} + 2xH_2O_{(aq)} \tag{5.13}$$

The electric potentials of the above half-cell equations are,

$$-E^{chem}_{an} F = \mu^o_{LiMn_2O_4} - \mu_{Li_{(1-x)}Mn_2O_4} - x\left(\mu^o_{Li^+} + RT \ln a_{Li^+}\right) \tag{5.14}$$

and

$$-E^{chem}_{cat} F = \frac{1}{2}\mu_{Li_{(1-x)}Mn_2O_4} - \left(\frac{1+x}{2}\right)\mu^o_{LiMn_2O_4} + x\left[\Delta G^o_{aq} + RT \ln\left(\frac{a_{Li^+} a_{Mn^{2+}}}{a^4_{H^+}}\right)\right] \tag{5.15}$$

where the terms in the square brackets refer to ions in the aqueous phase. ΔG^o_{aq} is the sum of all the standard potential terms of the aqueous phase. The other terms in Equation (5.15) a_{Li^+}, $a_{Mn^{2+}}$, and $a^4_{H^+}$ are the activities of Li^+, Mn^{2+}, and H^+ ions, respectively. The total electric potential of Hunter's equation is,

$$-E_{Chem}F = \frac{3}{2}\mu_{Li_{(1-x)}Mn_2O_4} - \left(\frac{3+x}{2}\right)\mu^{o}_{LiMn_2O_4} + x\left[\Delta G^{o}_{aq} + RT\ln\left(\frac{a^{2}_{Li^+}a_{Mn^{2+}}}{a^{4}_{H^+}}\right)\right] \tag{5.16}$$

where electric potential E_{Chem} is the total cell potential based on Hunter's equation.

5.2.3 The relation between the open-circuit potential of $LiMn_2O_4$ in solution to the electric potential of the electrochemical cell

If the reaction based on Hunter's equation is more carefully examined, the disproportionation reaction of the Mn^{3+} cations may be viewed as a corrosion process. According to Bockris and Reddy, in cases where corrosion occurs, the electron transfer is within the same material. Thus, the two electrodes are short circuited (8).

This is indeed the case for $LiMn_2O_4$, where the Mn^{3+} cations in the solid material reduce and oxidize at the same time. The redox reaction of the Mn^{3+} cations can be split into two half-cell reactions as expressed in Section 5.2.2. At equilibrium, the potential based on Hunter's equation, Equation (5.16), is zero. As a consequence, the potential of the cathodic reaction, Equation (5.15), is equal to the potential of the anodic reaction, Equation (5.14). Using the above argument, the following relation is,

$$E_{Chem} = E^{chem}_{cat} - E^{chem}_{an} = 0 \tag{5.17}$$

Thus,

$$E^{chem}_{cat} = E^{chem}_{an} \tag{5.18}$$

The corrosion potential is the equilibrium potential where the potentials of the cathodic and anodic reactions are equal and the current from both electrodes are at equilibrium. Thus,

$$E_{corr} = E_{cat}^{chem} = E_{an}^{chem} \tag{5.19}$$

where E_{corr} is the corrosion potential.

The anodic half-cell potentials for Li-ion extraction of $LiMn_2O_4$ by electrochemical means and by chemical means are exactly the same as presented in Equations (5.4) and (5.11). Thus, the corrosion potential of $Li_{(1-x)}Mn_2O_4$ in an acidic solution as a function of x Li^+ ions is the same potential as the anodic half-cell potential of the electrochemical cell or,

$$E_{corr(x)} = E_{an}^{chem(x)} = E_{an}^{cell(x)} = -E_{Cell(x)} + const. \tag{5.20}$$

Equation (5.20) presents the relationship between the open-circuit potential or corrosion potential of $Li_{(1-x)}Mn_2O_4$ in an acidic solution to the electric potential of $Li_{(1-x)}Mn_2O_4$ in an electrochemical cell as a function of x Li-ion extraction.

5.3 Experimental

5.3.1 Electrochemical characterization

Electrochemical tests were preformed using a MACCOR battery tester. Preparation of the electrodes was described in the first chapter. In brief, a slurry of electrode material was casted onto an aluminum substrate via the doctor blading technique. The amount of carbon for each electrode was kept constant at 5% by weight. Another 5% by weight was reserved for the binding material polyvinyl diflouride. Thus, 90% of the electrode was electrochemically active by weight. The counter and reference electrode was lithium metal. A 1M $LiPF_6$ salt in a 1:1 ethylene carbonate to dimethyl carbonate solvent (Merck) was used as the electrolyte. A porous polyethylene sheet (Solupor) separated the electrodes in a coin cell CR 2320 package (Hohsen). All cells were assembled in a Ar-filled glovebox.

The cell was charged at a C/10 rate and the current was interrupted at every 5% of the rated capacitive charge. The cell was standing at open circuit for approximately 20 minutes between each interruption. The measured open-circuit potential of the cell was directly taken at the end of the 20-minute period.

5.3.2 Open-circuit potential of $LiMn_2O_4$ in an acidic solution

Open-circuit potential measurements of $LiMn_2O_4$ in an acidic solution were performed by constructing a three-electrode cell. The $LiMn_2O_4$ electrode was in a pellet form that was 15 mm in diameter and 1mm thick. The pellet was pressed onto a Pt metal back contact. The other electrode was a Pt metal strip and the third electrode was a Ag/AgCl reference electrode. All three electrodes were submersed in an acidic solution with a pH value of 1. The open-circuit potential of the $LiMn_2O_4$ and Pt electrodes was measured against the Ag/AgCl reference electrode. The Pt back contact of the $LiMn_2O_4$ pellet was isolated from the solution. A MACCOR battery test system was used to record the open-circuit potential

5.3.3 Monitoring the open-circuit potential and pH of a solution containing $LiMn_2O_4$ particles as a function of Li-ion extraction

Chemical Li-ion extraction studies of $LiMn_2O_4$ were performed using a Metrohm titration system. One gram of 10 micron size particles of $LiMn_2O_4$ (Honeywell) was placed in a beaker and filled with 25ml of a 1M LiCl solution. Small amounts of 1M HCl acid (Baker) were automatically injected into the system under constant stirring. The equilibration time between each injection was 10 minutes.

The open-circuit potential of the Pt electrode in this solution was measured against a Ag/AgCl reference electrode. The open-circuit potential of this electrode couple was constantly measured as acid was continuously added to the system. The potential was recorded using the MACCOR battery test system. Care was taken to clean the Pt electrode with 1M HCl to remove any OH groups on the surface and stored in a slightly acidic solution before each experiment.

The open-circuit potential between a glass electrode versus a Ag/AgCl reference electrode was used to monitor the pH of the solution as additional acid was injected into the system. This electrode couple was calibrated between pH and potential using standardized buffer solutions (Fisher Scientific) of 2, 5, 8, and 11 pH before each experiment. The potential monitoring of this electrode couple was performed using a MACCOR battery test system.

5.4 Results and discussion

5.4.1 Open-circuit potential curve of the electrochemical cell

Figure 5-1 presents the open-circuit electric potential between the $LiMn_2O_4$ and lithium metal electrodes at every 5% of charge. The points are connected to show the well-known two-plateaux potential curve at 3.95V and 4.10V. As expected from previous studies (9), the first plateau slightly slopes while the second plateau is rather flat. It has been reported that the first plateau refers to a solid-solution phase between the compositions of $LiMn_2O_4$ and $Li_{0.5}Mn_2O_4$, while the second plateau refers to a two-phase region between the phases of $Li_{0.5}Mn_2O_4$ and λ–MnO_2.

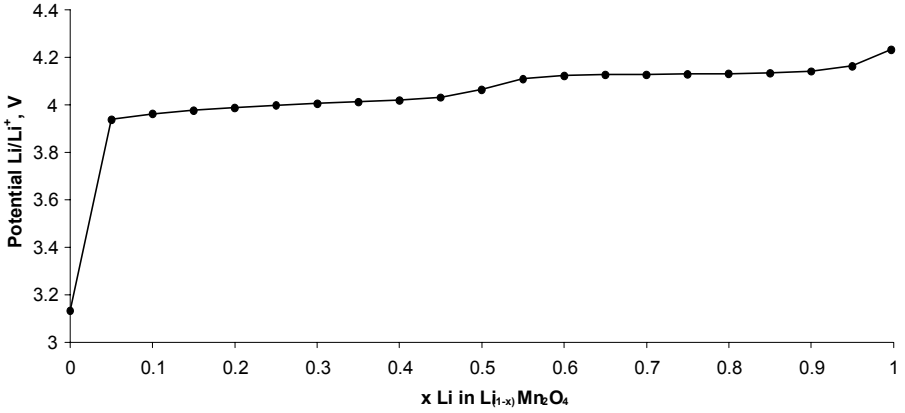

Figure 5-1 Open-circuit potential of $Li_{(1-x)}Mn_2O_4$ vs. Li metal as a function of x Li mole fraction

5.4.2 Chemical titration of $LiMn_2O_4$

5.4.2.1 Open-circuit potential measurements of $LiMn_2O_4$ in aqueous solution

The aim of this experiment is to measure the corrosion potential of $Li_{(1-x)}Mn_2O_4$ in an acidic solution. Since this cell is constructed using $LiMn_2O_4$, and Pt electrodes, and a Ag/AgCl reference electrode as described in Section 5.3.2, it is possible to measure the potential of each electrode to the reference electrode. The construction of each half-cell is the following,

Half-cell 1 $Pt / Li_{(1-x)}Mn_2O_4 / sol.//(3M)KCl / AgCl / Ag$

and

Half-cell 2 $Pt / sol.//(3M)KCl / AgCl / Ag$

where the single stripe and the double stripe refers to a phase boundary and the liquid junction, respectively. The term *sol.* refers to the aqueous solution that includes the products in solution based on Hunter's equation (Equation (5.1)). The total open-circuit potential for each half-cell may be expressed as the potential difference across each phase boundary. Thus,

$$E_{Half-cell1} = (\Psi_{Pt} - \Psi_{Li_{(1-x)}Mn_2O_4}) + (\Psi_{Li_{(1-x)}Mn_2O_4} - \Psi_{sol.}) + (\Psi_{sol.} - \Psi_{KCl}) + (\Psi_{KCl} - \Psi_{AgCl}) + (\Psi_{AgCl} - \Psi_{Ag}) \quad (5.21)$$

and

$$E_{Half-cell2} = (\Psi_{Pt} - \Psi_{sol}) + (\Psi_{sol} - \Psi_{KCl}) + (\Psi_{KCl} - \Psi_{AgCl}) + (\Psi_{AgCl} - \Psi_{Ag}) \quad (5.22)$$

where Ψ is the electric potential of each phase in the cell. In both half-cell cases the potential across the liquid junction, i.e., the potential difference between the solution and the KCl solution may be regarded as negligible or at least constant (10). Furthermore, the potential differences across the KCl – AgCl and AgCl-Ag boundaries are constant. Thus, Equations (5.21) and (5.22) become,

$$E_{Half-cell1} = (\Psi_{Pt} - \Psi_{Li_{(1-x)}Mn_2O_4}) + (\Psi_{Li_{(1-x)}Mn_2O_4} - \Psi_{sol}) + k \qquad (5.23)$$

and

$$E_{Half-cell2} = (\Psi_{Pt} - \Psi_{sol}) + k \qquad (5.24)$$

where k is the constant potential of the Ag/AgCl reference electrode. In this scheme, Half-cell 1 measures the potential of $LiMn_2O_4$ in solution and Half-cell 2 measures the potential of the solution relative to the Ag/AgCl reference electrode.

Figure 5-2 presents the open-circuit potential curves for both half-cells as a function of time. Half-cell 1 is the potential between the phase boundaries of $Pt/Li_{(1-x)}Mn_2O_4$ and $Li_{(1-x)}Mn_2O_4$/sol. Half-cell 2 is the potential between the phase boundary of Pt/sol. It is observed that these curves are similar in shape and in potential. Furthermore, the difference of measured open-circuit potentials of each cell becomes less over time as presented in Figure 5-3. This is probably due to the system coming into equilibrium over time. Since a pellet of $LiMn_2O_4$ was used, a significant amount of time is required for the system to achieve equilibrium. Based on these observations, it seems that the open-circuit potential of the Pt electrode in Half-cell 2 follows closely the corrosion potential of $Li_{(1-x)}Mn_2O_4$ in the acidic solution according to Hunter's equation.

One of the inconveniences with this experiment is the long time that is required for the cell to reach equilibrium. In the current study, a $LiMn_2O_4$ pellet proved that the equilibration time is long even after 20 hours of monitoring. The time for equilibrium to be reached may be shortened by increasing the surface area of the $LiMn_2O_4$, which will increase the contact between the solid and solution.

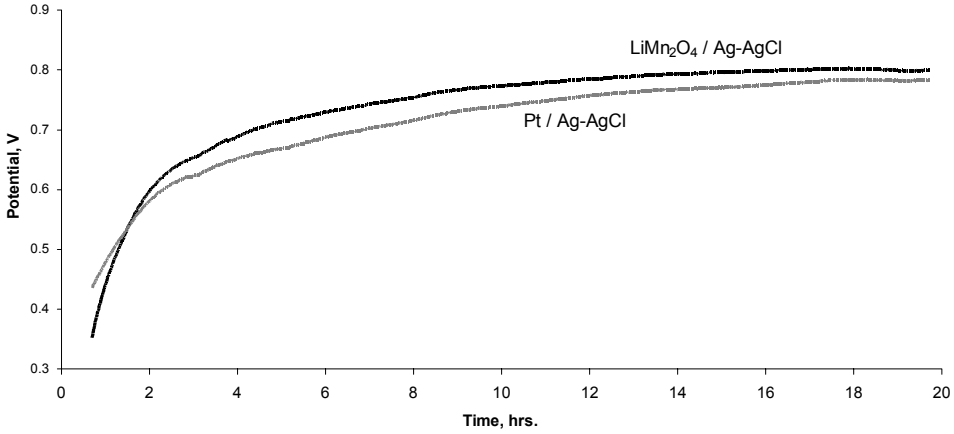

Figure 5-2 Potential curves as a function of time for each half-cell for a Pt / $LiMn_2O_4$ cell in an acidic solution using a Ag-AgCl reference electrode

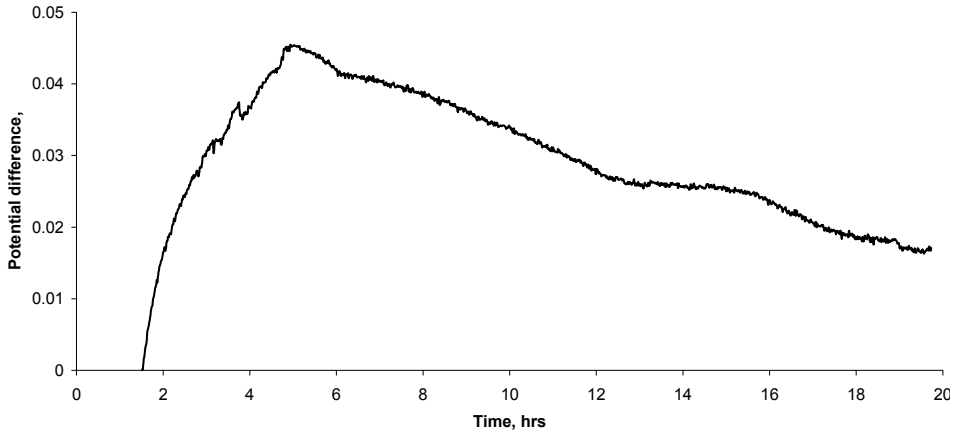

Figure 5-3 The potential difference as a function of time between the Pt and $LiMn_2O_4$ electrodes in an acidic solution

5.4.2.2 *Open-circuit potential of Pt / Ag-AgCl electrode couple in solution with $LiMn_2O_4$ particles*

Since the open-circuit potential of the Pt electrode is similar to the open-circuit potential of the $Li_{(1-x)}Mn_2O_4$ electrode as presented in Figure 5-2, it may be possible to measure the open-circuit potential or corrosion potential of $Li_{(1-x)}Mn_2O_4$ through the open-circuit potential of the Pt electrode. Using this argument, it is possible to increase the surface area of the $LiMn_2O_4$ by using this material in a particulate form in an acidic solution. A similar corrosion potential of $Li_{(1-x)}Mn_2O_4$ can then be measured through the Pt electrode in the solution that contains $LiMn_2O_4$ particles. This scheme has been described in more detail in Section 5.3.3.

The potential measured from the Pt/Ag-AgCl couple in aqueous solution that contains $LiMn_2O_4$ particles is presented in Figure 5-4. Using Hunter's equation, when 4 moles of H^+ ions react with 2 moles of $LiMn_2O_4$, 2 Li^+ ions are extracted from the $LiMn_2O_4$ material. By using this ratio, the amount of Li^+ ions extracted from $Li_{(1-x)}Mn_2O_4$ may be calculated for a specific volume of acid that is injected into the solution.

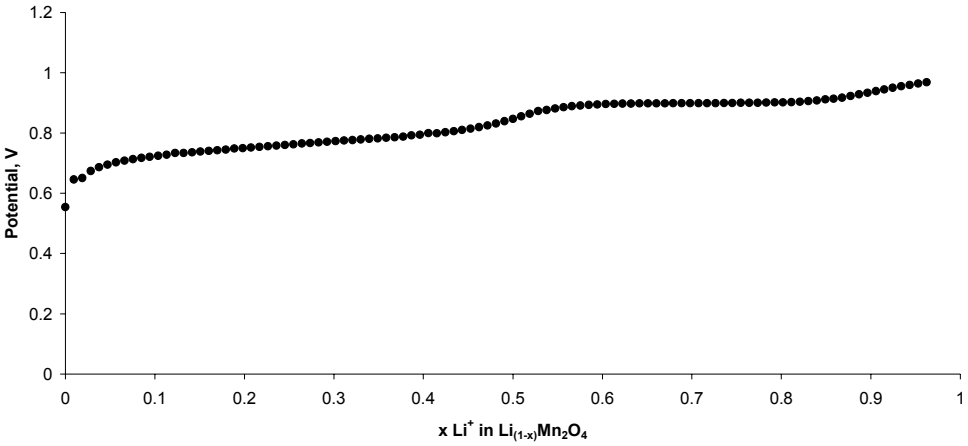

Figure 5-4 The potential curve as a function of Li-ion extraction of $LiMn_2O_4$ using a Pt electrode in an acidic solution that contains $LiMn_2O_4$ particles. The amount of Li-ion extraction was calculated by using Hunter's equation

Figure 5-5 presents the open-circuit potential curves as a function of Li-ion extraction from $LiMn_2O_4$ using the Pt electrode in a solution that contained $LiMn_2O_4$ particles and

from an electrochemical cell that used Li metal and $LiMn_2O_4$ electrodes. In addition, both potential curves were normalized to the hydrogen electrode (NHE). From this figure, the shape of both potential curves is similar. Furthermore, when both potential curves are normalized to the NHE, the two potential curves are very close to each other.

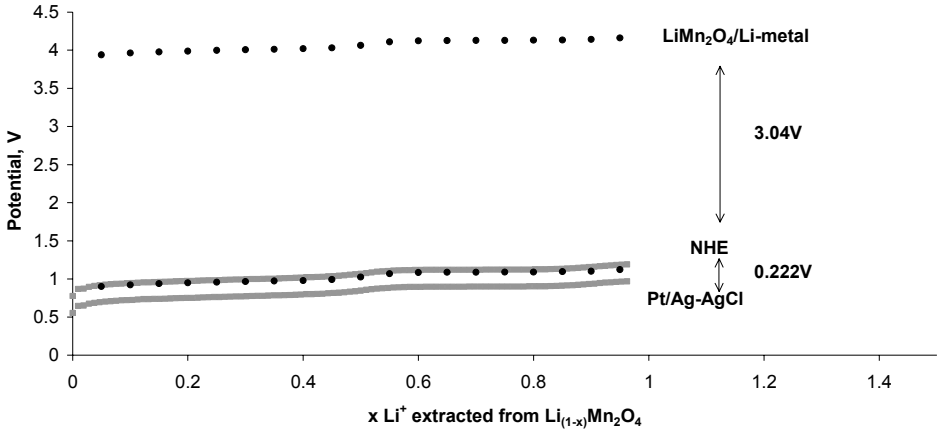

Figure 5-5 Comparison of potential curves between the electrochemical cell and Pt/Ag-AgCl electrodes as a function of x moles of Li^+ from $Li_{(1-x)}Mn_2O_4$. The amount of Li-ion extraction was calculated using Hunter's equation

This confirms that the open-circuit potential of the Pt/Ag-AgCl electrode couple is similar to the corrosion potential of $LiMn_2O_4$ in acid acidic solution according to Hunter's equation. Since the corrosion potential is equal to the half-cell potential based on Hunter's equation, and because the anodic half-cell reactions from Hunter's equation and from an electrochemical cell are the same, it is expected that the open-circuit potentials from both potentials are similar.

Although the potential curves presented in Figure 5-5 are close to each other, there is a small discrepancy. Figure 5-6 presents the normalized potential from Figure 5-5. One obvious explanation for this discrepancy is the equilibrium of the system. These experiments try to measure the open-circuit potential of both systems in equilibrium. However, it is rather difficult to determine the time it takes for equilibrium to be reached. Furthermore, the Pt electrode does not directly measure the corrosion potential

of $Li_{(1-x)}Mn_2O_4$. Thus, interfacial potentials must also be considered. Nevertheless, a basic relationship was found between the open-circuit potential of the electrochemical cell and the chemical extraction of Li^+ ions from $LiMn_2O_4$.

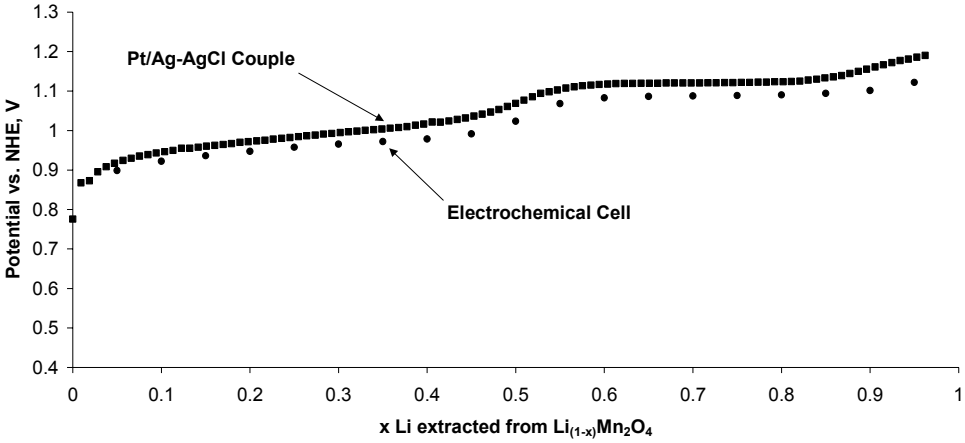

Figure 5-6 The potential curves as a function of Li-ion extraction from $LiMn_2O_4$ from Figures 5-5 normalized to the hydrogen electrode

5.4.2.3 Open-circuit potential as a function of pH

Figure 5-7 combines the measured open-circuit potential of the Pt/Ag-AgCl electrode couple as a function of the measured pH of a solution that contains $LiMn_2O_4$ particles. From this figure, a clear linear relationship between these two parameters is observed. A strong negative slope of -0.1178 V was observed within a pH range of 6 to 1.6.

In support of the current findings Kanoh et al. (5) have reported a similar slope of –0.1124 V by using a λ-MnO_2 spinel electrode vs. a calomel electrode between the pH of 5 to 3. In addition, Caudle et al. (6) have reported a similar large slope of –0.118 V. These authors have argued that the large negative slope was due to the disproportionation reaction of Mn^{3+} cations that oxidizes to Mn^{4+} and reduces to Mn^{2+} cations.

The slope value of –0.118 V seems to indicate that 2 moles of H^+ are involved in the chemical extraction of Li^+ ions from $LiMn_2O_4$. However, Hunter's equation uses 4 moles of H^+. This discrepancy may be resolved by the work of Caudle and co-workers

(6). These authors have argued that the neutralization of the acid from the disproportionation of manganese oxides particles in acidic solutions is an ion exchange between the proton and the manganese cation. This argument may also apply to the half-cell reaction presented in Equation (5.12) where the product of this reaction may be MnO. The following reaction would be an ion exchange between the Mn^{2+} cation of the oxide and two moles of H^+. This reaction would result in water plus the Mn^{2+} cation. Thus only 2 moles of H^+ are involved in the reduction of Mn^{3+} to Mn^{2+} cations that results in a negative slope of –0.118 V.

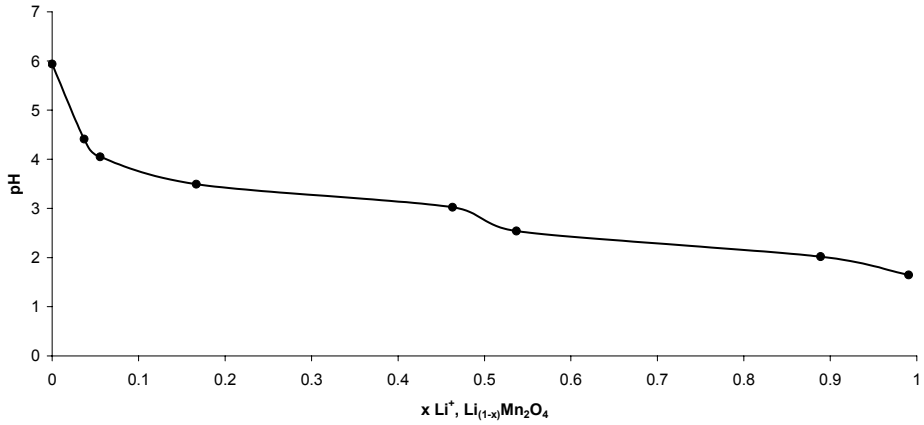

Figure 5-7 The potential of the Pt/Ag-AgCl electrode as a function of pH of the solution containing $LiMn_2O_4$ particles

5.4.2.4 pH as a function of Li-ion extraction from $LiMn_2O_4$

Figure 5-8 presents the measured pH as a function Li^+-ion extraction from $LiMn_2O_4$. Each point was measured at every 0.5 pH interval. From this figure, an outline of the two plateaux is observed. This corresponds to the observation reported by Kelder et al. (7).

Since a clear relationship between the open-circuit potentials from both methods using electrochemical and chemical Li-ion extraction has been found and that the pH of the solution is linearly related to these curves, it appears that the capacity of $LiMn_2O_4$ may be predicted by the pH of the solution. However, this requires both systems to be close

to equilibrium. To that respect, the findings here support the claims made by Kelder and co-workers (7).

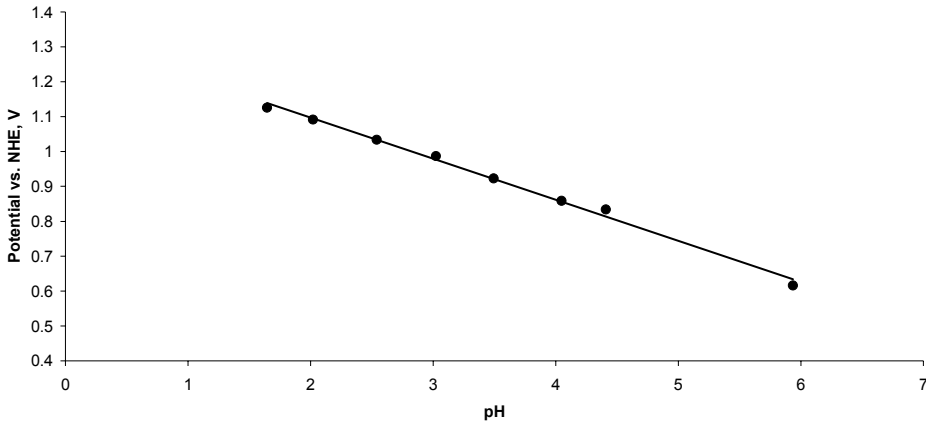

Figure 5-8 pH of solution with $LiMn_2O_4$ particles as a function of x moles of Li from $Li_xMn_2O_4$

5.5 Conclusions

The present findings support the claims stated by Kelder et al. that the capacity of $LiMn_2O_4$ may be predicted by measuring the pH of the solution when in contact with this material. This is due to the fact that the open-circuit potential of the solution as a function of x Li^+ ions in $LiMn_2O_4$ is similar to the open-circuit potential of a $LiMn_2O_4$ / Li metal electrode couple in an electrochemical cell. Furthermore, since the open-circuit potential of the solution is linearly related to the pH of the solution, the pH of the solution should also reflect the shape of the potential curve of an electrochemical cell as a function of x Li^+ ions in $LiMn_2O_4$.

5.6 References

1. Hunter, J. C. *J. Solid State Chemistry* **1981,** *39* 142-147.
2. Hunter, J. C. *United States Patent* **1982,** *4,312,930*.
3. Ooi, K.; Miyai, Y.; Katoh, S.; Maeda, H.; Abe, M. *Langmuir* **1989,** *5*(1), 150-157.
4. Ooi, K.; Miyai, Y.; Sakakihara, J. *Langmuir* **1991,** *7*(6), 1167-1171.
5. Kanoh, H.; Feng, Q.; Miyai, Y.; Ooi, K. *J.Electrochem. Soc.***1993,** *140*(11), 3162.
6. Caudle, J.; Summer, K. G.; Tye, F. L. *J. Chemical Society-Faraday Transactions* **1972,** *69* 889.
7. Kelder, E.; Ooms, F. J. B.; Perego, R.; Schoonman, J. *J.Power Sources* **2001,** *43*(26), 1.
8. Bockris, J. O.; Reddy, A. K. N. *Modern Electrochemistry;* Plenum Press: 1970.
9. Tarascon, J. M.; McKinnon, W. R.; Coowar, F.; Bowmer, T. N.; Amatucci, G.; Guyomard, D. *J. Electrochem. Soc.* **1994,** *141*(6), 1421-1431.
10. Bard, A. J.; Faulkner, L. R. *Electrochemical Methods;* John Wiley and Sons: 1980.

6

Summary / Samenvatting

Abstract / Samenvatting

A summary of the work in this thesis is presented which includes the results and major conclusions from each chapter. Furthermore a description for possible further research is discussed as a result of this work.

In dit hoofdstuk wordt een samenvatting van dit proefschrift gegeven met de belangrijkste conclusies uit ieder hoofdstuk. Daarnaast is een beschrijving van mogelijk toekomstig werk opgenomen, gebaseerd op de resultaten van dit proefschrift.

Introduction

Energy storage has been and will continue to be one of the most important areas in technology as energy consumption continually increases and the use of renewable energy sources like solar and wind energy also requires energy storage. One of the reasons for this increase in energy consumption is the increased use of portable electronic devices. Although portable electronics has existed since the early 20th century, the use of portable electronic devices to the everyday consumer has increases dramatically since the 1980's. The demand for such products stems from the fact that these devices are rather compact that makes them easy to carry. One of the most important reasons for the compactness of these devices is directly due to battery development that leads to the desired amount of dependable energy in such a compact volume.

This thesis examines two specific materials that are used in electrodes for a rechargeable Li-ion battery system. These are $Li_4Ti_5O_{12}$ and $LiMn_2O_4$ spinel materials. In the case of $Li_4Ti_5O_{12}$, the formation and the stability when treated with an acidic solution are studied. In the case of $LiMn_2O_4$, magnetic properties of the delithiated spinel by an acid are compared with $Li_{1+d}Mn_{2-d}O_4$. Finally, the corrosion potential of $LiMn_2O_4$ is correlated to the potential of an electrochemical cell as a function of Li-ion extraction.

Summary

In Chapter 2, the formation of $Li_4Ti_5O_{12}$ via solid-state or sol-gel routes are examined by using in-situ X-ray diffraction (XRD). By using this technique, the formation of $Li_4Ti_5O_{12}$ can be investigated in real time. In the case of the solid-state synthesis method, LiOH, Li_2CO_3, rutile and anatase TiO_2 were used as precursors. The sol-gel synthesis technique used Ti-isopropoxide and Li-acetate as precursors. From this investigation, it was found that the sol-gel synthesis process forms the spinel at a much lower temperature than the solid-state process. Furthermore, it was found that the $Li_4Ti_5O_{12}$ forms by the intermediate reaction of TiO_2 with Li_2TiO_3.

Chapter 3 investigated the reaction of $Li_4Ti_5O_{12}$ when in contact with an acidic solution. By using potentiometric titration of a solution that contains $Li_4Ti_5O_{12}$ particles with an acid, a buffer region in the potentiometric curve was observed. This means that acid was neutralized by the $Li_4Ti_5O_{12}$ particles. Through the use of atomic absorption spectroscopy (AAS), Li^+ ions were found in the solution after titration. From this result, it was reasoned that an ion exchange between the protons of the acid and Li^+ ions from $Li_4Ti_5O_{12}$ occurred. Further evidence of ion exchange was supported with results from infra-red (IR) spectroscopy on the exchanged material. In this IR spectrum, peaks were observed at wave numbers where protons are known to reside in spinels.

The lattice position of the exchanged protons was examined by using neutron diffraction. The position of these protons can be described as alternating sheets of octahedrally coordinated Li^+ and Ti^{4+} ions with tetrahedrally coordinated protons and Li^+ ions on 8a sites, as well as protons on the 48f sites. A graphical illustration of the ion-exchanged spinel is presented in Chapter 3.

Through the use of thermogravimetric analysis (TGA), it was found that the weight loss of the ion-exchanged material was substantial after heating to $440^{O}C$. From X-ray diffraction (XRD), the spinel and anatase TiO_2 phases are present after heating the material beyond $440^{O}C$. It seemed that the protons completely exit the spinel structure as water when heated beyond $440^{O}C$. Two proposed reactions are presented in Chapter 3 which include the ion exchange and the change of the exchanged material that occurs when heated above $440^{O}C$.

Electrochemical measurements of pristine $Li_4Ti_5O_{12}$ and the proton-exchanged spinel were performed using Li metal as a counter and reference electrode. The results show that as more protons are in the spinel structure, the potential deviates from a flat potential to a sloping potential as Li^+ ions intercalate and deintercalate from the spinel. Consequently, the capacity decreases as more protons are exchanged into the spinel.

Finally, a batch of $Li_4Ti_5O_{12}$ that was exposed to the atmosphere for a long period of time, showed a similar potential curve as for the proton exchanged material. By annealing the same material beyond $440^{O}C$, the potential curve was similar to that of the pris-

tine material. This indicated that $Li_4Ti_5O_{12}$ can react with the humidity of the normal atmosphere. The potential curves are presented in Chapter 3.

In Chapter 4, magnetic susceptibility measurements were performed on $LiMn_2O_4$ as a function of Li-ion extraction and on Li-substituted manganese spinels using the Faraday method. The results show that magnetic moments for all samples lie on the theoretical line where 100% of the Mn^{3+} cations in these spinels are in a high-spin electronic configuration. This is in contrast to previous reports where it was concluded that 80% of Mn^{3+} cations are in a high-spin configuration and 20% of these cations are in a low-spin configuration.

In addition, the Weiss temperature of these materials shows a similar trend from strongly negative to less negative as the average oxidation state of the Mn cations increases from 3.5 to 3.7. When the average Mn-oxidation state increases beyond 3.7, there are two distinct trends of the Weiss temperature. One trend shows very little change in the Weiss temperature as the average Mn-oxidation state increases from 3.7 to 3.9 when Li^+ ions are continuously removed from $LiMn_2O_4$. The other trend is a continuation of the original trend as the average Mn-oxidation state increases by the substitution of Mn cations by Li^+ ions. An explanation for the magnetic interactions is presented in Chapter 4.

Chapter 5 investigated the potential of a solution that contains $LiMn_2O_4$ particles as a function of pH and Li-ion extraction. It was known that a disproportionation reaction of the Mn^{3+} cations in $LiMn_2O_4$ occurs if this material is in contact with an acidic solution. As the disproportionation reaction proceeds, Li^+ ions and Mn^{3+} cations are extracted from the $LiMn_2O_4$ spinel material. If one traces the pH of the solution as a function of Li-ion extraction, a similarity in the shape of the curve is observed between the pH curve and the potential curve of an electrochemical cell as Li^+ ions are extracted from the $LiMn_2O_4$ spinel. This chapter finds that the open-circuit potential of the solution that contained $LiMn_2O_4$ particles as a function of Li-ion extraction had the same shape and potential if both potentials from the electrochemical curve and from the solution are normalized to the hydrogen electrode. By using a thermodynamic analysis of the two systems, it was determined that the corrosion potential of the $LiMn_2O_4$ is similar to the potential of an electrochemical cell as a function of Li-ion extraction. Additionally, a

linear relationship between the pH of the solution and the corrosion potential of $LiMn_2O_4$ was found.

Outlook

The future work that may be interesting and based on the work presented in this thesis could focus on,

- Applications of the proton exchanged $Li_4Ti_5O_{12}$
- Determining the diffusion coefficient of Li^+ ions in a material using potentiometric measurements of a solution containing $LiMn_2O_4$ particles

Several applications for proton-exchanged $Li_4Ti_5O_{12}$ can be anticipated. One obvious application is a proton conductor for an intermediate-temperature solid oxide fuel cell. Although ionic conductivity of the exchanged material has not been presented in this thesis, a report from Corcoran et al. has published another proton exchanged lithium titanium oxide for which conductivity measurements were performed (1). In their report, the ionic conductivity of that proton-exchanged material was difficult to measure because of the relatively large volume change between the non-exchanged and the exchanged material. This also would make it rather difficult to produce. An advantage of the proton-exchanged $Li_4Ti_5O_{12}$ spinel material is the small volume change that is less than 1%. Another application for this material is an electrolyte in a Nernst-type hydrogen sensor. A preliminary investigation observed a Nernst-type potential when this material was exposed to varying pressures of hydrogen gas (2). Although the preliminary investigation is promising, further work is needed in this area.

An interesting alternative route to determine the Li-ion diffusion coefficient of $LiMn_2O_4$ is to use potentiometric measurements of an acidic solution that contains $LiMn_2O_4$ particles. Since the corrosion potential, based on Hunter's equation, is equal to the potential of an electrochemical cell, these measurements may be monitored as a function of time and Li-ion extraction. In principle, a diffusion length and the time for Li^+ ions to exit the structure can then be established.

Introductie

Energie-opslag is en zal één van de belangrijkste technologische gebieden blijven, omdat de energieconsumptie continu toeneemt en omdat het gebruik van hernieuwbare energiebronnen zoals wind- en en zonne-energie ook energieopslag vragen. Eén van de redenen voor de toename in de energieconsumptie is het toenemende gebruik van draagbare elektronische apparaten. Hoewel draagbare elektronische apparatuur al bestaat sinds het begin van de 20^{e} eeuw, is het gebruik van deze apparatuur door de alledaagse consument drastisch toegenomen sinds de jaren 80 van de vorige eeuw. De vraag naar dergelijke produkten komt voort uit de compactheid van deze apparatuur waardoor deze gemakkelijk mee te nemen is. Een van de meest belangrijke redenen voor de compactheid van deze apparaten is direct gekoppeld aan de ontwikkeling van batterijen, waardoor de benodigde energie in een dergelijk compact volume eindelijk mogelijk is geworden.

In dit proefschrift worden twee specifieke materialen onderzocht, die gebruikt worden als elektrode in een herlaadbaar Li-ion batterijsysteem. Dit zijn de spinellen $Li_4Ti_5O_{12}$ en $LiMn_2O_4$. Van $Li_4Ti_5O_{12}$ zijn de vorming en de stabiliteit tijdens behandeling met zuur bestudeerd. Van $LiMn_2O_4$ zijn de magnetische eigenschappen van met zuur gedelithieerde spinel bestudeerd en vergeleken met $Li_{(1+\delta)}Mn_{(2-\delta)}O_4$ spinellen. Tenslotte is de corrosiepotentiaal van $LiMn_2O_4$ gerelateerd aan de potentiaal van een elektrochemische cel als functie van geextraheerde Li-ionen.

Samenvatting

In Hoofdstuk 2 is de vorming van $Li_4Ti_5O_{12}$ middels vastestof of sol-gel routes bestudeerd met behulp van in-situ Röntgendiffractie (XRD). Door het gebruik van deze techniek kan de vorming van $Li_4Ti_5O_{12}$ real-time gevolgd worden. Voor de vaste-stof synthese werden LiOH, Li_2CO_3 en rutile en anatase TiO_2 gebruikt als grondstoffen. Voor de sol-gel route is gebruik gemaakt van Ti-isopropoxide en Li-acetaat grondstoffen. Uit dit onderzoek is gebleken dat $Li_4Ti_5O_{12}$ via het sol-gel synthese proces bij veel lagere temperaturen gevormd wordt dan via het vaste-stof synthese proces. Daarnaast is gevonden dat $Li_4Ti_5O_{12}$ gevormd wordt uit de tussenreactie van TiO_2 en Li_2TiO_3.

In Hoofdstuk 3 is de reactie van $Li_4Ti_5O_{12}$ in contact met een zure oplossing bestudeerd. Met behulp van een potentiometrische titratie van een $Li_4Ti_5O_{12}$ -bevattende oplossing met een zuur, is in de potentiometrische curve een bufferzone gevonden. Dit betekent dat het zuur werd geneutraliseerd door de $Li_4Ti_5O_{12}$ deeltjes. Met behulp van atomaire absorptie spectrometrie (AAS) zijn na de titratie Li^+ ionen aangetoond in de oplossing. Uit dit resultaat is geconcludeerd dat een uitwisseling tussen de protonen van het zuur en de Li^+ ionen van $Li_4Ti_5O_{12}$ heeft plaatsgevonden. Ondersteunend bewijs voor deze ionenwisseling kwam uit de resultaten van infrarood (IR) spectroscopie van het uitgewisselde materiaal. In het IR spectrum werden pieken gevonden bij golfgetallen die overeenkomen met die van protonen in spinellen.

De roosterplaatsen van de uitgewisselde protonen is onderzocht met behulp van neutronendiffractie. De roosterposities van deze protonen kunnen worden beschreven als alternerende lagen van octaedrisch gecoördineerde Li^+ en Ti^{4+} ionen en tetraedrisch gecoordineerde protonen en Li^+ ionen op 8a posities en Ti^{4+} ionen op 48f posities. Een grafische illustratie van het uitgewisselde spinel is afgebeeld in Hoofdstuk 3.

Uit thermogravische analyses (TGA) is gebleken dat het gewichtsverlies van het uitgewisselde materiaal substantieel was na verwarming tot 440°C. Uit Röntgendiffractie (XRD) is gebleken dat de spinel en TiO_2 anatase fasen aanwezig waren na verwarming tot 440°C. Dit duidde erop dat de protonen volledig uit de spinel struktuur verdwijnen in de vorm van water bij verwarming boven 440°C. Twee reacties worden gegeven in Hoofdstuk 3 voor de uitwisseling en de verandering van het uitgewisselde materiaal na verwarming boven 440°C.

Elektrochemische metingen zijn gedaan aan $Li_4Ti_5O_{12}$ en de uitgewisselde spinel met metallisch lithium als tegen- en als referentie elektrode. De resultaten laten zien dat bij aanwezigheid van meer protonen in de spinel, de potentiaal gaat afwijken van een vlakke potentiaal naar een hellende potentiaal wanneer Li^+ ionen intercaleren en deïntercaleren in de spinel. Daarom neemt de capaciteit van de spinel af naarmate meer protonen zijn uitgewisseld.

Tenslotte is van een hoeveelheid $Li_4Ti_5O_{12}$, die voor langere tijd was blootgesteld aan de atmosfeer, vastgesteld dat de potentiaalcurve vergelijkbaar was met die van uitgewis-

seld materiaal. Na verwarming van dit blootgestelde materiaal boven 440°C was de potentiaalcurve gelijk aan die van het uitgangsmateriaal. Deze bevindingen duiden erop dat $Li_4Ti_5O_{12}$ kan reageren met het vocht in de normale atmosfeer. De potentiaalcurves zijn afgebeeld in Hoofdstuk 3.

In Hoofdstuk 4 worden magnetische susceptibiliteitsmetingen op basis van de Faraday methode beschreven aan $LiMn_2O_4$ als functie van Li-ion extractie en aan Li-gesubsitueerde mangaan spinellen. De resultaten laten zien dat de magnetische momenten voor alle preparaten op de theoretische lijn liggen waarbij 100% van de Mn^{3+} ionen zich in de elektronische hoog-spin configuratie bevinden. Dit komt niet overeen met eerdere publicaties waarin werd geconcludeerd dat 80% van de Mn^{3+} kationen in de hoog-spin configuratie en 20% in de laag-spin configuratie voorkwam.

Daarnaast vertoont de Weiss temperatuur een vergelijkbare trend van sterk negatief tot minder negatief wanneer de gemiddelde oxidatietoestand van de Mn kationen toenmeent van 3.5 naar 3.7. Wanneer de gemiddelde Mn-oxidatietoestand toeneemt boven 3.7 zijn er twee aparte trends. De eerste trend laat weinig verandering in de Weiss temperatuur zien als de gemiddelde Mn-oxidatietoestand toeneemt van 3.7 tot 3.9, wanneer Li+ ionen continu worden verwijderd uit $LiMn_2O_4$. De andere trend is een continuering van de oorspronkelijke trend waar de Mn-oxidatietoestand toeneemt bij de substitutie van Mn kationen door Li^+ ionen. Een verklaring voor de magnetische interacties wordt gegeven in Hoofdstuk 4.

In Hoofdstuk 5 wordt de potentiaal van een oplossing onderzocht, die $LiMn_2O_4$ deeltjes bevat, als functie van de pH en Li-ion extractie. Het is bekend dat een disproportioneringsreactie van de Mn^{3+} ionen in $LiMn_2O_4$ optreedt als dit materiaal in contact komt met een zure oplossing. Tijdens de disproportioneringsreactie worden Li^+ ionen en Mn^{3+} kationen uit $LiMn_2O_4$ geextraheerd. Wanneer de pH van de oplossing als functie van Li-ion extractie wordt opgenomen dan valt een vergelijk op tussen de pH curve en de potentiaalcurve van een elektrochemische cel waarin Li^+ ionen worden geextraheerd uit $LiMn_2O_4$. In dit Hoofdstuk wordt aangetoond dat de open-cel spanning van de oplossing met $LiMn_2O_4$ deeltjes als functie van Li-ion extractie dezelfde vorm en potentiaal heeft als de elektrochemische potentiaalcurve, wanneer beide worden genormaliseerd ten opzichte van de normaalwaterstofelektrode. Met behulp van een thermodynamische analy-

se van de twee systemen is bepaald dat de corrosiepotentiaal van $LiMn_2O_4$ vergelijkbaar is met de potentiaal van een elektrochemische cel als functie van de Li-ion extractie. Daarnaast is een lineaire relatie gevonden tussen de pH van de oplossing en de corrossiepotentiaal van $LiMn_2O_4$.

Vooruitzicht

Interessant toekomstig werk, gebaseerd op het werk in dit proefschrift, zou zich kunnen richten op,

- Toepassing van proton-uitgewisseld $Li_4Ti_5O_{12}$
- Het meten van de diffusiecoefficient van Li^+ ionen in een materiaal met behulp van potentiometrische metingen aan een oplossing die deeltjes $LiMn_2O_4$ bevat

Een aantal toepassingen van proton-uitgewisseld $Li_4Ti_5O_{12}$ kan worden verwacht. Een voor de hand liggende toepassing is een protongeleider voor een vaste-stof brandstofcel. Hoewel de ionogene geleiding van het uitgewisselde materiaal niet is gerapporteerd in dit proefschrift is wel een publicatie verschenen van Corcoran et al. voor een ander proton-uitgewisseld lithium titanium oxide waarin geleidingsmetingen zijn gerapporteerd (1). Uit die publicatie blijkt dat de geleiding van het uitgewisselde materiaal moeilijk te meten was door de relatief grote volumeverandering tussen het uitgangsmateriaal en het uitgewisselde materiaal. Dit zou ook de produktie ervan bemoeilijken. Een voordeel van het proton-uitgewisselde $Li_4Ti_5O_{12}$ spinel materiaal is de geringe volumeverandering, die kleiner is dan 1%. Een andere toepassing van dit materiaal is als elektrolyt in een Nernst-type waterstofsensor. In een eerste onderzoek werd een Nernst- potentiaal geobserveerd bij blootstelling van dit materiaal aan waterstof bij verschillende drukken (2). Hoewel het eerste onderzoek veelbelovend was is meer werk nodig op dit gebied.

Een interessante alternative route om de Li-ion diffusiecoefficient van $LiMn_2O_4$ te bepalen is met behulp van potentiometrische metingen aan een zure oplossing die $LiMn_2O_4$ deeltjes bevat. Omdat de corrosiepotentiaal, gebaseerd op Hunter's vergelijking, gelijk is aan de potentiaal van een elektrochemische cel kunnen deze metingen gevolgd wor-

den als functie van tijd en Li-ion extractie. In principe kunnen dan een diffusielengte en de tijd, die nodig is voor Li^+ ionen om de struktuur te verlaten, bepaald worden.

References / Referenties

1. Corcoran, T. D.; Irvine. J. *Solid State Ionics* **2000,** *136-137* 297.

2. Caba V.M; Simon D.R.; Landschoot R.C. van; Draghici C.; Schoonman J.; *Bramat 2005, Book of Abstracts* (pp. 293-293). Brasov, Romania.

Acknowledgements

The completion of a Ph.D. project could not be possible without the support, help, encouragement, and patience of many people. I would like to express my gratitude to all those who made the creation of this thesis possible. I am indebted in so many ways and to so many people, that it would be impossible to name all of them here.

First of all, I would like to thank my promoter, Professor Dr. Joop Schoonman, for giving me the opportunity to come to The Netherlands and work in his group. I appreciate our interesting scientific discussions where he made me see the big picture of things. Through these discussions, new ideas and concepts were brought out to me and forced me to look at things in a different way. I also appreciate the editorial comments that also forced me to write in a sound and clear manner.

Secondly, many thanks to Dr. Erik Kelder for being my daily supervisor. Erik has always been a man with many ideas that also inspired me to have my own ideas and to research these ideas. I am also grateful for the opportunities that he facilitated for me to meet and collaborate with other experts from the battery and structural analysis fields.

I would also thank the people with whom I have collaborated in the past; Professor Janina Molenda in Krakow and Dr. Jerzy Pielaszek in Warsaw for interesting discussions and structural analysis of $Li_4Ti_5O_{12}$ spinel material, Dr. Ernst van Eck and Dr. Dave Pickup who were at the time at the University of Kent for NMR studies on $LiMn_2O_4$, Horst Krampitz from Honeywell Inc. in Germany for supplying $LiMn_2O_4$ material, Niek van der Pers of Materials Science for performing the set-up and preparation of the in-situ XRD and helping in the analysis, Ioana Benga, a master's student from Romania, who performed the arduous task of measuring magnetic susceptibility of $LiMn_2O_4$, Dr. Fokko Mulder from RID for lively discussions, and special thanks go to Dr. Marnix Wagemaker from RID who performed and analyzed the neutron diffraction data of the proton-exchanged $Li_4Ti_5O_{12}$, Finally, to the scientists of the Alistore Network of Excellence that facilitate meetings with the top researchers in the battery field in Europe.

I am very grateful to the past and present members of the battery team for their scientific and social skills and their support. Many thanks to Dr. Hong Huang, Dr. Michiel Jak, Dr. Nitte van Landschoot, Dr. Raffaella Perego, Dr. Frederique Belliard, Dr. Adam Best, and Neil Hancock. This appreciation extends to the present members, Dr. Ugo Lafont, Corrado Locati, Mario Valvo, with a special, heartfelt thanks to Loïc and Agnes Simonin, and to all the masters students that worked here through the years. Finally, an infinite amount of thanks to my scientific and business partner Frans Ooms.

I thank the staff and past members of the former Inorganic Chemistry Group, Dr. Albert Goosens, Dr. Roel van der Krol, and the technicians Ben Meester, Ton van der Plas, Joost Middelkoop, Fritz de Lange, with special thanks to Robert van Landschoot, and to the former students and post-docs Dr. Carolien Huisman and Dr. Liesbeth Reijnen (my former officemates), Dr. Harry Donker, Barbara van der Zanden, Yorik Kamlag, Dr. Leen van Rij, Ruben Loef, Christina Enache with special thanks to Dr. Marian Nanu, and Dr. Hans van't Spijker. Last, but certainly not the least, the administrative matters could never be accomplished without the help of two fine administrative assistants, Astrid Barrow and Marian de Bruijn.

A special thanks goes to all the people that I have befriended here in The Netherlands that are outside of academia. Although it is hard to mention everybody here, special attention goes to Bertrand, Nicolas, Kay, and Paola who first showed me the ropes in living in this country. An extended thanks to all of the musicians that I have the privilege to work and socialize with.

A personal thanks to my family (Mary, Ruth, Georgia, Chrissy, Laura, George, and Ray) and friends back in the U.S. It was not an easy decision for me to move here, but they supported me in all of my endeavours. This is true especially for my parents, George and Margaret. Finally, I cannot express the profound support from one special person who, without it, the completion of this thesis would never come about, Silvia.

About the author

Daniel Russell Simon was born on November 11, 1968 in a little northern town of Ashtabula, Ohio in the United States of America. He received a Bachelor of Science degree in Materials Engineering at the University of Cincinnati in 1992. During his bachelor study, he worked as an intern at Argonne National Laboratory in the Chemical Technology Division for the Advanced Battery Group. During this internship, he worked with Thomas Kaun in developing a secondary high temperature Li/FeS_2 battery for the possible application in electric vehicles.

After graduation, he briefly worked as an engineer in the R&D section for a battery company, SAFT America, located in Baltimore, Maryland. Although this company specialized in production of high-temperature lithium metal primary batteries used in defence missiles, the R&D objective was to develop a high temperature seal used for secondary lithium metal batteries. These batteries would also be used in electric vehicle applications.

In 1993 he returned to Argonne as an assistant engineer working for the same group. In the same year, he along with two other co-workers received the 1993 R&D 100 Award for sulphide seal development. From 1994-1997 he worked in the test and post-test analysis group for experimental and commercial batteries. During this period he worked with many battery systems such as NiMH, lead acid, sodium/sulphur, and Li-ion batteries. In 1998, he was transferred to the Nuclear Waste group which specialized in the encasement of radioactive salt wastes. In 1999 he returned to the Advanced Battery Group working on the Li-ion battery system with many talented electrochemists and material scientists such as Dr. Khalil Amine and Dr. Michael Thackeray.

In 2000 he decided to work for a Ph.D. degree in Professor Joop Schoonman's group at Delft University of Technology in The Netherlands with Dr. Erik Kelder. This thesis describes the work he did in his Ph.D. career. Currently, he is a part owner of a company, Nedusa EM, that specializes in the production and consultation of energy materials and battery systems. This biography describes only part of his working career that he has made for himself. The other part of his career that will not be described here is that of a semi-professional musician.

Publications

M.Wagemaker, D.R.Simon, E.M.Kelder, J.Schoonman, C.Ringpfeil, U.Haake, D.Luetxenkirchen-Hecht, R.Frahm, F.M.Mulder; "A kinetic two-phase and equilibrium solid solution in spinel $Li_{4+x}Ti_5O_{12}$", *Advanced Materials*, 18(23), (2006)

D.R.Simon, M.Wagemaker, E.M.Kelder, F.M.Mulder, J.Schoonman; "Characterization of proton exchanged $Li_4Ti_5O_{12}$ spinel material", *Solid State Ionics*, 177(26-32), (2006)

V.M. Caba, , D.R. Simon, , R.C. van Landschoot, , C. Draghici, , J. Schoonman; "Nerst sensor for hydrogen detection", *Bramat 2005, Book of Abstracts* (pp. 293-293). Brasov, Romania

M.Wagemaker, D.R.Simon, E.M.Kelder, J.Schoonman, F.M.Mulder; "Proton positions in spinel $H_{0.9}Li_{0.1}[Li_{0.33}Ti_{1.67}]O_4$", *Physica B: Condensed Matter,* 350(1-3), (2004)

D.M.Pickup, D.R.Simon, M.Fooken, H.Krampitz, E.R.H. van Eck, E.M.Kelder; "6Li MAS NMR study of stoichiometric and chemically delithiated $Li_xMn_2O_4$ spinels", *Journal of Materials Chemistry*, 13(4), (2003)

J.Marzec, K.Swierczek, J.Przewoznik, J.Molenda, D.R.Simon, E.M.Kelder, J.Schoonman; "Conduction mechanism in operating a $LiMn_2O_4$ cathode", *Solid State Ionics,* 146(3,4), (2002)

H.Huang, E.M.Kelder, D.R.Simon, J.Schoonman; "Electrochemical Impedance spectroscopy analysis on the processes of Li intercalation into $Li_4Ti_5O_{12}$", *Proceedings-Electrochemical Society*, 137-143 (2001)

H.Huang, E.M.Kelder, D.R.Simon, J.Schoonman; "Preparation and electrochemical characteristics of lithium titanium oxide spinel $Li_4Ti_5O_{12}$", *Proceedings-Electrochemical Society*, 120-127 (2001)

E.M.Kelder, F.G.B.Ooms, D.R.Simon, R.Perego, J.Schoonman; "Capacity, stability, and rate capability of $Li_{1+d}Mn_{2-d}O_4$ measured by chemical delithiation", *ITE Letters on Batteries, New Technologies & Medicine,* 2(1), (2001)

M.C.Hash, J.P.Thalacker, D.R.Simon, G.L.Burns, R.H.Woodman; "The evaluation of sintered sodalite-glass composites", *Ceramic Transactions,* 93, (1999)

M.C.Hash, G.L.Burns, J.P.Thalacker, D.R.Simon, C.Pereira, M.A.Lewis; "Hot isostatic pressing of sodalite-glass composites", *215th ACS National Meeting,* Dallas, March29-April 2, (1998)

T.D.Kaun, M.C.Hash, D.R.Simon; "Sulfide ceramics in molten-salt electrolyte batteries", *Ceramic Transactions,* 65, (1996)

T.D.Kaun, M.J.Duoba, W.P.Johll, V.Luong, F.C.Mrazek, D.J.Palkon, D.R.Simon; "Developmant of prototype sealed bipolar lithium/sulphide cells", *Proceedings of the Intersociety Energy Conversion Engineering Conference,* 417-22, (1991)

T.D.Kaun, M.J.Duoba, K.R.Gillie, M.C.Hash, D.R.Simon, D.R.Vissers; "Development of a sealed bipolar lithium-alloy/ferric sulfide battery for electric vehicles", *Proceedings of the Intersociety Energy Conversion Engineering Conference,* 335-40, (1990)

T.D.Kaun, M.J.Duoba, K.R.Gillie, D.R.Simon, D.R.Vissers; "Lithium-alloy/iron(II) sulfide as a sealed bipolar battery", *Proceedings of the International Power Sources Symposium,* 26-9, (1990)

H.Huang, E.M.Kelder, F.G.B.Ooms, D.R.Simon; "Process for fabrication of batteries for use at high temperatures", International patent application WO 2002009215, (2002)

Propositions

part of this thesis
Characterization of $Li_4Ti_5O_{12}$ and $LiMn_2O_4$ spinel materials
treated with aqueous acidic solutions

1. It is possible to determine the diffusion of Li^+ ions in $LiMn_2O_4$ using potentiometric measurements of an acidic solution containing $LiMn_2O_4$. (Kelder et al., *J. Power Sources* **2001,** *97-8,* 433-436 and this thesis Chapter 5)

2. Knowing the physics behind a fitting parameter is just as important as the fit itself. (Chung et al., *J. Power Sources* **2001,** *97-8,* 454-457 and this thesis Chapter 4)

3. Using the term "and so on" when describing problems of a system shows that the authors did not research all problems. (Cho et al., *Solid State Ionics* **2007**, 178, 119-123)

4. The use of hydrocarbons to produce hydrogen will never be environmentally friendly. (Bockris, *International Journal of Hydrogen Energy* **2007**, 32, 153-158).

5. It is unlikely for materials that are stable in basic solutions to be stable in the normal atmosphere. (this thesis Chapter 3).

6. An academic group should be proud to foster spin-off companies because it displays the practical and technical merits of the group as well as the determination of its people to market the technology.

7. The expression "I make enough money." does not only reflect financial but also career stagnation.

8. With regard to becoming an entrepreneur, one of the basic differences between the Dutch and the American view is the perception of failure.

9. Most people would not hire an electrician to do a plumber's job. However, in academia and research institutions, this scenario seems to be a common occurrence.

10. The phrase "playing a musical instrument" does not give the professional musician any justice.

Daniel Simon

These propositions are considered opposable and defendable and as such have been approved by the supervisor, Prof.dr. J. Schoonman.

Stellingen

behorende bij het proefschrift
Characterization of $Li_4Ti_5O_{12}$ and $LiMn_2O_4$ spinel materials
treated with aqueous acidic solutions

1. Het is mogelijk om de diffusie van Li^+ ionen in $LiMn_2O_4$ te bepalen met behulp van potentiometrische metingen in een zure oplossing die $LiMn_2O_4$ bevat. (Kelder et al., *J. Power Sources* **2001,** *97-8,* 433-436 en dit proefschrift Hoofdstuk 5)

2. Het is net zo belangrijk om de natuurkunde achter een modelparameter te begrijpen als het model zelf. (Chung et al., *J. Power Sources* **2001,** *97-8,* 454-457 en dit proefschrift Hoofdstuk 4)

3. Het gebruik van de term "and so on" in het beschrijven van de problemen van een systeem laat zien dat de auteurs niet alle problemen hebben onderzocht. (Cho et al., *Solid State Ionics* **2007**, 178, 119-123)

4. Het gebruik van koolwaterstoffen om waterstof te produceren zal nooit milieuvriendelijk zijn. (Bockris, *International Journal of Hydrogen Energy* **2007**, 32, 153-158)

5. Het is onwaarschijnlijk dat materialen die stabiel zijn in een basische oplossing, stabiel zijn aan de normale atmosfeer. (dit proefschrift Hoofdstuk 3)

6. Een academische groep zou trots moeten zijn op het stimuleren van spin-off bedrijven omdat het de praktische en technische kunde van een groep laat zien alsook het doorzettingsvermogen van de mensen om een technologie te vermarkten.

7. De uitdrukking "ik verdien genoeg" duidt niet alleen op financiële maar ook op loopbaanstagnatie.

8. Een van de basale verschillen tussen de Nederlandse en Amerikaanse kijk op het ondernemerschap is de perceptie van falen.

9. De meeste mensen nemen geen elektricien aan voor loodgieterswerk. Aan universiteiten en onderzoeksinstituten is dit echter een normaal verschijnsel.

10. De uitdrukking "een muziekinstrument bespelen" doet geen recht aan professionele muzikanten.

Daniel Simon

Deze stellingen worden opponeerbaar en verdedigbaar geacht en zijn als zodanig goedgekeurd door de promotor, Prof.dr. J. Schoonman.